Engineering Structures

A meshless computational framework for a modified dynamic system of vehicle coupled with plate structure

--Manuscript Draft--

Manuscript Number:	ENGSTRUCT-D-24-01037R1
Article Type:	Research Paper
Section/Category:	Oceania, Mainland China, Taiwan, Hong Kong, Macau, Singapore, Japan, Korea
Keywords:	Train-bridge interaction system; Meshless method; Computational plate-shell mechanics; high-speed railway; Rail irregularity
Corresponding Author:	Ping Xiang Central South University Hong Kong, HONG KONG
First Author:	Zhanjun Shao
Order of Authors:	Zhanjun Shao
	Han Zhao
	Peng Zhang
	Xiaonan Xie
	A. S. Ademiloye, Ph.D.
	Ping Xiang
Manuscript Region of Origin:	Asia Pacific
Abstract:	In previous simulations of train-bridge interaction systems (TBIS), the supporting system for the train are commonly treated as beam structures, leading to less accurate results, particularly for small-span cases. To address this limitation, a modified vertical TBIS is proposed. In the presented TBIS, the supporting system is considered as a Reissner-Mindlin plate, and the displacement field is described by first-order shear deformation theory (FSDT). To establish the model, radial point interpolation method (RPIM), a meshless method, is employed. Finally, a coupled dynamic equation is established to calculate various responses of the system. Several numerical examples are presented to illustrate the disparities between the system based on plate model and traditional beam model. The results indicate that the beam model yields higher estimates of the mid-span vertical displacement of the bridge, while the peak of the mid-span vertical acceleration is smaller compared to the plate model; additionally, it is observed that the carbody is primarily influenced by rail irregularities. Consequently, the proposed plate model offers distinct advantages over the beam model in providing comprehensive structural response information, thereby offering novel insights into bridge design and analysis. Additionally, this marks the inaugural application of themeshless method in the field of TBIS, which further extends the application scope of meshless methods.
Suggested Reviewers:	C. W. Lim, Ph.D. Prof., City University of Hong Kong bccwlim@cityu.edu.hk Prof. Lim is an expert in the field of meshless method.
	Xiaoqiao He, Ph.D. Prof., City University of Hong Kong bcxqhe@cityu.edu.hk Prof. He is an expert in the field of structural vibration and dynamics.
Opposed Reviewers:	
Response to Reviewers:	

Highlights

- A new train-bridge interaction system (TBIS) is proposed.
- The FSDT-RPIM modeling approach is first used in the field of TBIS.
- The proposed TBIS is more competitive than the traditional system.
- The feasibility of further improving the box girder model in TBIS is verified.

A meshless computational framework for a modified dynamic system of vehicle coupled with plate structure

Zhanjun Shao[a,b], Han Zhao[a,b], Peng Zhang[a,b], Xiaonan Xie[a,b], A. S. Ademiloye[c], Ping Xiang[a,b,*]

[a] *School of Civil Engineering, Central South University, Changsha, 410075, Hunan, China*
[b] *National Engineering Research Center of High-speed Railway Construction Technology, Changsha, 410018, Hunan, China*
[c] *Data and AI (ZI), Zienkiewicz Institute for Modelling, College of Engineering, Swansea University, Swansea, W Glam, Wales*

Abstract

In previous simulations of train-bridge interaction systems (TBIS), the supporting system for the train are commonly treated as beam structures, leading to less accurate results, particularly for small-span cases. To address this limitation, a modified vertical TBIS is proposed. In the presented TBIS, the supporting system is considered as a Reissner-Mindlin plate, and the displacement field is described by first-order shear deformation theory (FSDT). To establish the model, radial point interpolation method (RPIM), a meshless method, is employed. Finally, a coupled dynamic equation is established to calculate various responses of the system. Several numerical examples are presented to illustrate the disparities between the system based on plate model and traditional beam model. The results indicate that the beam model yields higher estimates of the mid-span vertical displacement of the bridge, while the peak of the mid-span vertical acceleration is smaller compared to the plate model; additionally, it is observed that the carbody is primarily influenced by rail irregularities. Consequently, the proposed plate model offers distinct advantages over the beam model in providing comprehensive structural response information, thereby offering novel insights into bridge design and analysis. Additionally, this marks the inaugural application of the

---

[*] Corresponding author.
Email address: `pxiang2-c@my.cityu.edu.hk` (Ping Xiang)

meshless method in the field of TBIS, which further extends the application scope of meshless methods.

Keywords: Train-bridge interaction system, Meshless method, Computational plate-shell mechanics, High-speed railway, Rail irregularity

---

1. Introduction

By the end of 2022, the total length of Chinese high-speed railway has exceeded 42,000 km. In this extensive network, a significant portion of the railway lines is composed of bridges [1, 2]. The construction of high-speed railways frequently faces various challenges related to terrain and environmental conditions. Therefore, it is necessary to conduct demonstrations to assist in the design process. Numerical simulation is highly recommended in this regard, primarily due to the substantial costs associated with conducting physical tests. In recent decades, researchers have created a variety of TBIS utilizing various numerical methods. These TBIS can be broadly classified into three distinct categories: programming-based, finite element software-based, and co-simulation-based.

The first category of TBIS relies entirely on programming. It involves processes such as utilizing MATLAB to simplify each component of the TBIS and establishing a mechanical model for each part [3–5]. Subsequently, these models are integrated using multi-body dynamics principles to formulate the dynamic equations governing the TBIS. For example, in this approach, the trains are simplified to mass points, while the tracks, piers, bridges, and other components are represented as simplified beam structures ~~[3, 6–11]~~[6–11]. These components are then interconnected, taking into account the wheel-rail interaction and multi-body dynamics. Beam structures are widely used in buildings, especially frame structures [12]. However, for many complex structures in TBIS, the beam structures do not represent thier mechanical performance well. For instance, it is not reasonable to approximate track slabs [13–15] and box girder bridges [16, 17] solely as beam structures, given their intricate nature. Hence, a crucial research focus lies in determining a reasonable and accurate approach for modeling track slabs and bridges within the first category of TBIS.

The second category of TBIS primarily relies on commercial software for modeling purposes. The components within the system are modeled using software such as ABAQUS or ANSYS or some other software, and subsequent assembly and calculations are performed within the software framework [18]. This approach takes advantage of well-established commercial software with robust modeling capabilities. In this type of TBIS, components like rails, track slabs, and bridges receive more intricate modeling, but the simulation of inter-component relationships, especially the wheel-rail relationship, is a complex task.

The third category of TBIS represents a combination of the first two. In this hybrid TBIS, components located above the bridge are typically modeled using MATLAB, while commercial software is uesd to tackle the intricate modeling of complex structures, such as bridges and piers [19]. This approach capitalizes on the strengths of the first two TBIS and often yields heightened modeling accuracy. However, it is worth noting that this approach comes with a relatively high threshold due to the concurrent use of multiple modeling platforms.

The first category of TBIS is the most commonly employed and offers extensive utility in conducting various analyses. These applications involve the investigation of factors such as impact of prestressed concrete bridge creep [20], as well as integrating it with neural networks to formulate predictions regarding train running safety [21]. Meanwhile, the first category of TBIS is entirely based on the programming platform, offering researchers significant flexibility. In contrast, the second category of TBIS faces limitations imposed by commercial software and the challenges of secondary development, and has some difficulties in introducing advanced mechanical theories. For academic research, the first category of TBIS proves more advantageous. Furthermore, the first category of TBIS is implemented on a single platform, eliminating the need for multi-platform data exchange as required in the third category of TBIS. Moreover, in some cases, the third category of TBIS requires the introduction of supercomputing platform support, which is costly. This reduction in development cost and complexity further supports its academic appeal. Therefore, the research object of this paper is the first category of TBIS. To enhance the accuracy of programming-based TBIS, the primary research focus is directed towards optimizing structural modeling. We drew inspiration from the enhancements achieved by researchers in refining the track slab model and embarked on an effort to enhance the bridge model. Many high-speed railway bridges are designed with simply supported box girder bridges, with dimensions more closely resembling plate structures than beam structures. Furthermore, these bridges exhibit intricate mechanical responses that cannot be replicated using beam elements alone. Consequently, in the pursuit of enhanced accuracy and the ensurance of reliability in train running safety analysis, this paper tries to substitute the beam model with a plate model, coupled with the train, in the development of TBIS.

Finite element method (FEM) [22] and its extensions, implemented in various commercial software, are the predominant approaches for modeling of plate structures [23]. However, FEM requires the construction of complex mesh to discretize and solve partial differential equations. Consequently, researchers must focus on mesh quality to achieve accurate results, and the cost of generating high-quality mesh is much higher than the computational cost [24]. While meshless methods has no mesh limitation, they do not require an explicitly defined connectivity between nodes for the definition of the shape functions. Moreover, the approximation and interpolation functions of meshless methods are usually high-order continuous, without the distortion effect of the mesh, ensuring the global smoothness of stress and making it easy to handle large deformation problems [25], dynamic analysis [26], acoustic analysis [27], etc. In addition to the classical methods like moving least squares method ~~[24, 28–30]~~[28–30], smoothed particle hydrodynamics method [31, 32], reproducing kernel particle method [33, 34], general finite difference method [35, 36], point interpolation method [37], etc., several new meshless methods have emerged, building upon these classical approaches. Radial basis functions (RBFs) have played a crucial role in the advancement of meshless methods. RBFs can be either compactly supported or globally gained, and their introduction has enhanced the performance of many classical methods. For example, in order to prevent the occurrence of matrix singularity issues in point interpolation method, RBFs have been introduced to guarantee the compatibility of the approximate function, which is called radial point interpolation method [38, 39]; Wei [40–43] introduced RBFs into reproducing kernel particle method and successfully used this method to analyze the mechanical behavior of a variety of structures and materials. These examples illustrate the advantages of meshless methods and demonstrate their feasibility for modeling bridge plates.

In this paper, we propose a computational framework based on RPIM and FSDT. The framework improves the bridge model and helps to improve the accuracy of the TBIS. Furthermore, the introduction of this framework opens up opportunities for creating more intricate bridge models utilizing multiple plates, and multiple plate structures hopefully yield more accurate simulation results. Meanwhile, the utilization of FSDT in conjunction with RPIM [44–46], as employed in this paper, enjoys broad recognition within the realm of computational mechanics for plates and shells, but it is the first attempt in the field of TBIS. The work path of this paper is shown as Fig. 1.

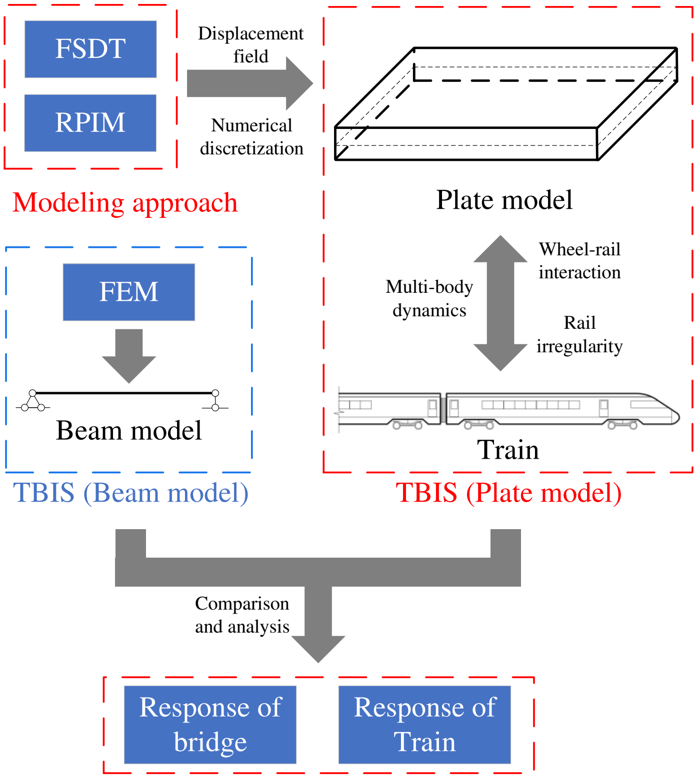

Figure 1: The work path of this paper.

2. Vertical TBIS

Vertical TBIS primarily concentrates on the vertical structural response. Despite its reduced degrees of freedom, this system proves conducive to validating novel approaches, including stochastic analyses~~[16, 47]~~[47]. It is also suitable for scrutinizing factors significantly affecting vertical structural response, such as structural concrete creep ~~[20, 48]~~[48]. In this paper, we opt to employ vertical TBIS for the validation of our proposed computational framework, with the intention of later extending its applicability to spatial TBIS in future research. Moreover, both vertical and spatial TBIS can be established by the principle of total potential energy with stationary value in elastic system dynamics proposed by Zeng ~~[17, 49]~~[49], so only derivation results are given in this paper. In addition, the modified vertical TBIS proposed in this paper is shown in Fig. 2, and the variables in the figure are explained by Tab. 1.

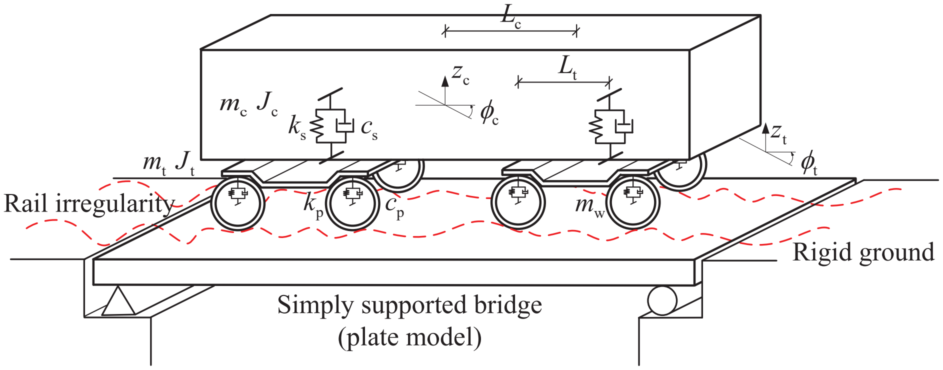

Figure 2: The proposed vertical train-bridge interaction system.

Based on the vertical TBIS presented in Ref. [16], the wheel and rail exhibit a close-fitting relationship expressed by the following equation:

$$z_{\mathrm{w}i} = z_{\mathrm{b}i} + z_{\mathrm{r}i} \tag{1}$$

where z represents the vertical displacement, and the subscript w denotes the wheel, b denotes the bridge, r denotes the vertical rail irregularity, and i denotes the $i-$th wheel. Eq. (1) indicates that the vertical displacement $z_{\mathrm{w}i}$ of the $i-$th wheel is the sum of the vertical displacement $z_{\mathrm{b}i}$ of the bridge and the vertical rail irregularity $z_{\mathrm{r}i}$ at its location.

Due to the relationship between the wheel and rail, a vehicle contains 6 DOFs, i.e.

$$\boldsymbol{U}_{\mathrm{v}} = \begin{bmatrix} z_{\mathrm{c}} & \phi_{\mathrm{c}} & z_{\mathrm{t1}} & \phi_{\mathrm{t1}} & z_{\mathrm{t2}} & \phi_{\mathrm{t2}} \end{bmatrix}, \tag{2}$$

Table 1: Explanation of variables in Fig. 2.

Variable	Explanation
z_{c}	Vertical displacement of carbody
ϕ_{c}	Rotational displacement of carbody
m_{c}	Mass of carbody
J_{c}	Mass moment of inertia of carbody
z_{t}	Vertical displacement of bogie
ϕ_{t}	Rotational displacement of bogie
m_{t}	Mass of bogie
J_{t}	Mass moment of inertia of bogie
m_{w}	Mass of wheel
k_{s}	Spring stiffness of the second suspension
c_{s}	Damping coefficient of the second suspension
k_{p}	Spring stiffness of the primary suspension
c_{p}	Damping coefficient of the primary suspension
L_{c}	Half of longitudinal distance between the centers of front and rear bogies
L_{t}	Half of bogie axle base

The mass matrix corresponding to the vector of DOF is denoted as follows.

$$\boldsymbol{M}_{\mathrm{v}} = \begin{bmatrix} m_{\mathrm{c}} & 0 & 0 & 0 & 0 & 0 \\ 0 & J_{\mathrm{c}} & 0 & 0 & 0 & 0 \\ 0 & 0 & m_{\mathrm{t1}} & 0 & 0 & 0 \\ 0 & 0 & 0 & J_{\mathrm{t1}} & 0 & 0 \\ 0 & 0 & 0 & 0 & m_{\mathrm{t2}} & 0 \\ 0 & 0 & 0 & 0 & 0 & J_{\mathrm{t2}} \end{bmatrix}, \tag{3}$$

Meanwhile, in Fig. 2, the suspensions are modeled as springs and damping elements. Thus, the stiffness matrix [50] of the car can be written as

$$\boldsymbol{K}_{\mathrm{v}} = \begin{bmatrix} 2k_{\mathrm{s}} & 0 & -k_{\mathrm{s}} & 0 & -k_{\mathrm{s}} & 0 \\ 0 & 2k_{\mathrm{s}}L_{\mathrm{c}}^2 & k_{\mathrm{s}}L_{\mathrm{c}} & 0 & -k_{\mathrm{s}}L_{\mathrm{c}} & 0 \\ -k_{\mathrm{s}} & k_{\mathrm{s}}L_{\mathrm{c}} & 2k_{\mathrm{p}}+k_{\mathrm{s}} & 0 & 0 & 0 \\ 0 & 0 & 0 & 2k_{\mathrm{p}}L_{\mathrm{t}}^2 & 0 & 0 \\ -k_{\mathrm{s}} & -k_{\mathrm{s}}L_{\mathrm{c}} & 0 & 0 & 2k_{\mathrm{p}}+k_{\mathrm{s}} & 0 \\ 0 & 0 & 0 & 0 & 0 & 2k_{\mathrm{p}}L_{\mathrm{t}}^2 \end{bmatrix}, \tag{4}$$

The damping matrix $\boldsymbol{C}_{\mathrm{v}}$ has the same form as $\boldsymbol{K}_{\mathrm{v}}$, except that k_{s} and k_{p} are replaced by c_{s} and c_{p}.

A train often consists of multiple vehicles. The stiffness matrix $\boldsymbol{K}_{\mathrm{vv}}$ of the train can be written as

$$\boldsymbol{K}_{\mathrm{vv}} = \operatorname{diag}\begin{bmatrix}\boldsymbol{K}_{\mathrm{v}1} & \boldsymbol{K}_{\mathrm{v}2} & \cdots & \boldsymbol{K}_{\mathrm{v}N}\end{bmatrix} \tag{5}$$

where N represents the train contains N vehicles; $\boldsymbol{K}_{\mathrm{v}1}$ and $\boldsymbol{K}_{\mathrm{v}N}$ are normally motor cars, and $\boldsymbol{K}_{\mathrm{v}2} \sim \boldsymbol{K}_{\mathrm{v}N-1}$ are trailer cars. Similarly, $\boldsymbol{M}_{\mathrm{vv}}$ and $\boldsymbol{C}_{\mathrm{vv}}$ can be obtained in the same form.

The TBIS in this study consists of two components, train and bridge. Therefore, the dynamic equation of the vertical TBIS can be written as

$$\begin{bmatrix}\boldsymbol{M}_{\mathrm{vv}} & \\ & \boldsymbol{M}_{\mathrm{bb}}\end{bmatrix}\begin{Bmatrix}\ddot{\boldsymbol{u}}_{\mathrm{vv}} \\ \ddot{\boldsymbol{u}}_{\mathrm{bb}}\end{Bmatrix}+\begin{bmatrix}\boldsymbol{C}_{\mathrm{vv}} & \boldsymbol{C}_{\mathrm{vb}} \\ \boldsymbol{C}_{\mathrm{bv}} & \boldsymbol{C}_{\mathrm{bb}}\end{bmatrix}\begin{Bmatrix}\dot{\boldsymbol{u}}_{\mathrm{vv}} \\ \dot{\boldsymbol{u}}_{\mathrm{bb}}\end{Bmatrix}+\begin{bmatrix}\boldsymbol{K}_{\mathrm{vv}} & \boldsymbol{K}_{\mathrm{vb}} \\ \boldsymbol{K}_{\mathrm{bv}} & \boldsymbol{K}_{\mathrm{bb}}\end{bmatrix}\begin{Bmatrix}\boldsymbol{u}_{\mathrm{vv}} \\ \boldsymbol{u}_{\mathrm{bb}}\end{Bmatrix}=\begin{Bmatrix}\boldsymbol{F}_{\mathrm{vv}} \\ \boldsymbol{F}_{\mathrm{bb}}\end{Bmatrix}, \tag{6}$$

where the matrices associated with the bridge, such as $\boldsymbol{M}_{\mathrm{bb}}$, $\boldsymbol{K}_{\mathrm{bb}}$, $\boldsymbol{K}_{\mathrm{vb}}$, etc., are obtained after determining the mechanical model of the bridge.

3. Plate mechanics

In computational plate mechanics, different theories exist to describe the mechanical behavior of thin [51], medium-thick, or thcik plate [52] structures. These theories include Kirchhoff-Love theory [53, 54], Reissner-Mindlin theory (FSDT [55–57]), and several higher-order shear deformation theories. In this study, FSDT is employed to describe the displacement field of the plate.

The employment of FSDT is based on the following primary considerations:

(1) In comparison to Kirchhoff-Love theory, the displacement field in Reissner-Mindlin theory is independently interpolated at displacement and rotating angle, respectively, which holds significant importance. This arises from the fact that, following the discretization by the meshless method, the nodal displacement vectors in the Kirchhoff-Love theory do not incorporate the rotating angle (as shown in Eq.(7)), rendering it unsuitable for assembling box girder structures with multiple plates in subsequent studies.

$$\boldsymbol{u}_{\mathrm{K}} = \begin{cases} u \\ v \\ w \end{cases} \text{(Kirchhoff-Love)}\,, \boldsymbol{u}_{\mathrm{R}} = \begin{cases} u \\ v \\ w \\ \theta_x \\ \theta_y \end{cases} \text{(Reissner-Mindlin)} \tag{7}$$

(2) The higher-order shear theories have a larger number of degrees of freedom compared to FSDT, leading to an increase in computational requirements. Given that the thickness of the bridge plate is thick, the applications of higher-order shear theories do not yield substantial benefits in terms of model accuracy; instead, it diminishes computational efficiency.

To summarize the belongings, the employment of FSDT is crucial in this study and its follow-up.

3.1. First-order shear deformation theory

Establishing the plate model as shown in Fig. 3, the displacement field based on FSDT can be defined as

$$u = u_0 + z\theta_x \tag{8}$$

$$v = v_0 + z\theta_y \tag{9}$$

$$w = w_0 \tag{10}$$

where u, v, and w represent the displacements in the x, y, and z directions, respectively; the subscript 0 denotes the mid-plane of the plate; θ_x and θ_y represent the rotations of a transverse normal about positive y and negative x axes. Therefore, u_0, v_0, w_0, θ_x, and θ_y are the basic unknowns of the displacement field.

The geometric equations of the plate can be listed as

$$\begin{Bmatrix} \varepsilon_x \\ \varepsilon_y \\ \gamma_{xy} \end{Bmatrix} = \boldsymbol{\varepsilon}_0 + z\boldsymbol{\kappa}, \quad \begin{Bmatrix} \gamma_{yz} \\ \gamma_{xz} \end{Bmatrix} = \boldsymbol{\gamma}_0, \tag{11}$$

$$\boldsymbol{\varepsilon}_0 = \begin{Bmatrix} \frac{\partial u_0}{\partial x} \\ \frac{\partial v_0}{\partial y} \\ \frac{\partial u_0}{\partial y} + \frac{\partial v_0}{\partial x} \end{Bmatrix}, \quad \boldsymbol{\kappa} = \begin{Bmatrix} \frac{\partial \theta_x}{\partial x} \\ \frac{\partial \theta_y}{\partial y} \\ \frac{\partial \theta_x}{\partial y} + \frac{\partial \theta_y}{\partial x} \end{Bmatrix}, \quad \boldsymbol{\gamma}_0 = \begin{Bmatrix} \theta_y + \frac{\partial w_0}{\partial y} \\ \theta_x + \frac{\partial w_0}{\partial x} \end{Bmatrix}. \tag{12}$$

Meanwhile, the constitutive equations can be written as

$$\begin{Bmatrix} \sigma_x \\ \sigma_y \\ \sigma_{xy} \\ \sigma_{yz} \\ \sigma_{xz} \end{Bmatrix} = \begin{bmatrix} Q_{11} & Q_{12} & 0 & 0 & 0 \\ Q_{12} & Q_{11} & 0 & 0 & 0 \\ 0 & 0 & Q_{44} & 0 & 0 \\ 0 & 0 & 0 & Q_{44} & 0 \\ 0 & 0 & 0 & 0 & Q_{44} \end{bmatrix} \times \begin{Bmatrix} \varepsilon_x \\ \varepsilon_y \\ \gamma_{xy} \\ \gamma_{yz} \\ \gamma_{xz} \end{Bmatrix}, \tag{13}$$

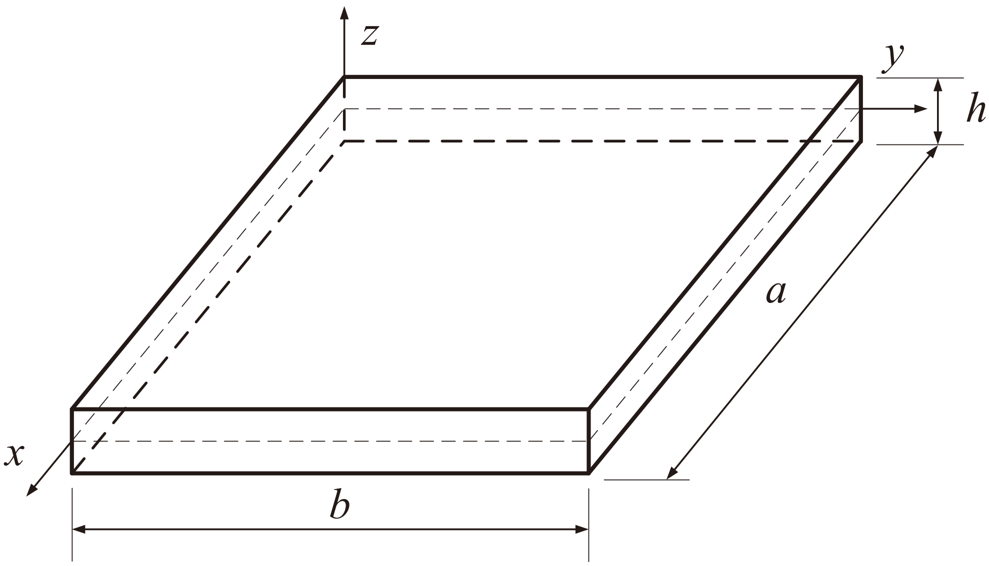

Figure 3: The geometry of the plate model.

assuming that the bridge plate behaves isotropically, we have

$$Q_{11} = \frac{E}{1-v^2}, \quad Q_{12} = \frac{vE}{1-v^2}, \quad Q_{44} = \frac{E}{2(1+v)}, \tag{14}$$

where E is Young's modulus and v is Poisson's ratio.

According to Eqs. 12 and 13, the relationship between in-plane force $\boldsymbol{P}$ and strain $\boldsymbol{\epsilon}$ can be obtained as

$$\boldsymbol{P} = \boldsymbol{S}\boldsymbol{\epsilon} \tag{15}$$

where $\boldsymbol{S}$ can be given by

$$\boldsymbol{S} = \begin{bmatrix} \boldsymbol{A} & \bar{\boldsymbol{B}} & \boldsymbol{0} \\ \bar{\boldsymbol{B}} & \boldsymbol{D} & \boldsymbol{0} \\ \boldsymbol{0} & \boldsymbol{0} & \boldsymbol{A}_{\mathrm{s}} \end{bmatrix}, \tag{16}$$

with

$$\begin{gathered} \left\{A_{ij} \quad B_{ij} \quad D_{ij}\right\} = \int_{h/2}^{-h/2} \left(1,\, z,\, z^2\right) Q_{ij} \mathrm{d}z \\ A_{ij}^{\mathrm{s}} = K \int_{h/2}^{-h/2} Q_{ij} \mathrm{d}z \end{gathered} \tag{17}$$

and the transverse shear correction coefficient $K = 5/6$.

3.2. Radial point interpolation method

Compared with the meshless methods where penalty functions are used to impose boundary conditions, the shape function of radial point interpolation method [38] has the property of Kronecker δ function, which can easily impose the essential boundary. At the same time, the coupled polynomial and radial basis point interpolation method constructs a shape function that preserves the linear regenerative characteristics of the polynomial basis point interpolation method. It also possesses the compatibility advantage of the radial basis point interpolation method, allowing for automatic adaptation to an arbitrary number of supporting nodes, typically resulting in high approximation accuracy. Therefore, this study employs RPIM as a numerical discretization tool.

The approximation displacement fiedl function $u^{\mathrm{h}}(\boldsymbol{x})$ of RPIM can be written as

$$u\left(\boldsymbol{x}\right) \approx u^{\mathrm{h}}\left(\boldsymbol{x}\right) = \sum_{t=1}^{m} p_t\left(\boldsymbol{x}\right) a_t + \sum_{s=1}^{NP} R_s\left(\boldsymbol{x}\right) b_s = \boldsymbol{p}^{\mathrm{T}}\left(\boldsymbol{x}\right) \boldsymbol{a} + \boldsymbol{R}^{\mathrm{T}}\left(\boldsymbol{x}\right) \boldsymbol{b}, \quad (18)$$

where $\boldsymbol{p}(\boldsymbol{x})$ is the polynomial basis functions and $\boldsymbol{R}(\boldsymbol{x})$ is the radial basis functions~~;~~. For the plate structures, the complete quadratic basis functions are

$$\boldsymbol{p}\left(\boldsymbol{x}\right) = \begin{bmatrix} 1 & x & y & x^2 & xy & y^2 \end{bmatrix}^{\mathrm{T}} \quad (19)$$

And the radial basis functions $\boldsymbol{R}(\boldsymbol{x})$ are defined as

$$\boldsymbol{R}\left(\boldsymbol{x}\right) = \begin{bmatrix} R_1\left(\boldsymbol{x}\right), & R_2\left(\boldsymbol{x}\right), & \cdots, & R_{NP}\left(\boldsymbol{x}\right) \end{bmatrix}^{\mathrm{T}} \quad (20)$$

where the number of the terms NP denotes the number of the supporting node contained in the supporting domain Ω_{S} with the coordinate $\boldsymbol{x}$ as the center. The supporting domain encompasses the supporting nodes, as illustrated in Fig. 4, with all the black supporting nodes contained within the blue box. It then interpolates to generate information about the computational node $\boldsymbol{x}$ through the shape function. The extent of the supporting domain is determined by the scale influence factor χ, and achieving a reasonable range for the supporting domain is crucial to produce results with relatively high accuracy.

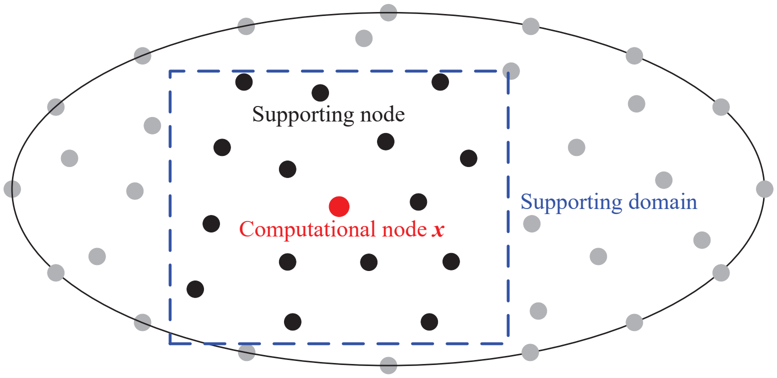

Figure 4: Supporting domain and supporting nodes of the meshless method.

The value of the radial basis function depends only on the distance function r, and in this paper, the multi-quadratic radial basis function is employed, i.e.

$$R_s(\boldsymbol{x}) = \left[r^2 + (\alpha h)^2\right]^{\beta}, \tag{21}$$

where $r = \sqrt{(x - x_s)^2 + (y - y_s)^2}$; h is the average node spacing; α and β are the shape coefficients, and they are set to 1 and 1.03 respectively according to Ref. [39].

On the supporting domain Ω_{S} of the computing node $\boldsymbol{x}$, the functional J_1 and J_2 is constructed based on the set of the scattered supporting nodes $\{x_I\}_{I=1}^{NP}\left(\forall x_I \in \Omega_{\mathrm{S}}\right)$.

$$J_1 = \sum_{I=1}^{NP}\left[\boldsymbol{P}_I^{\mathrm{T}}(\boldsymbol{x})\,\boldsymbol{a} + \boldsymbol{R}_I^{\mathrm{T}}(\boldsymbol{x})\,\boldsymbol{b} - \hat{u}_I\right], \tag{22}$$

$$J_2 = \sum_{I=1}^{NP} p_t(\boldsymbol{x}_I)\, b_I, \quad t = 1, 2, \cdots, 6. \tag{23}$$

Let $J_1 = 0$, $J_2 = 0$, Eq. (24) can be obtained.

$$\begin{bmatrix} \boldsymbol{A} & \boldsymbol{P} \\ \boldsymbol{P}^{\mathrm{T}} & \boldsymbol{0} \end{bmatrix} \begin{bmatrix} \boldsymbol{b} \\ \boldsymbol{a} \end{bmatrix} = \begin{bmatrix} \hat{\boldsymbol{u}} \\ \boldsymbol{0} \end{bmatrix}, \tag{24}$$

where $\boldsymbol{P}$ and $\boldsymbol{A}$ can be written as

$$\boldsymbol{P} = \begin{bmatrix} p_1(\boldsymbol{x}_1) & p_2(\boldsymbol{x}_1) & \cdots & p_6(\boldsymbol{x}_1) \\ p_1(\boldsymbol{x}_2) & p_2(\boldsymbol{x}_2) & \cdots & p_6(\boldsymbol{x}_2) \\ \vdots & \vdots & \ddots & \vdots \\ p_1(\boldsymbol{x}_{NP}) & p_2(\boldsymbol{x}_{NP}) & \cdots & p_6(\boldsymbol{x}_{NP}) \end{bmatrix} \tag{25}$$

$$\boldsymbol{A} = \begin{bmatrix} R_1(\boldsymbol{x}_1) & R_2(\boldsymbol{x}_1) & \cdots & R_{NP}(\boldsymbol{x}_1) \\ R_1(\boldsymbol{x}_2) & R_2(\boldsymbol{x}_2) & \cdots & R_{NP}(\boldsymbol{x}_2) \\ \vdots & \vdots & \ddots & \vdots \\ R_1(\boldsymbol{x}_{NP}) & R_2(\boldsymbol{x}_{NP}) & \cdots & R_{NP}(\boldsymbol{x}_{NP}) \end{bmatrix} \tag{26}$$

By solving Eq. (24), we have

$$\boldsymbol{a} = \underbrace{\left(\boldsymbol{P}^{\mathrm{T}}\boldsymbol{A}^{-1}\boldsymbol{P}\right)^{-1}\boldsymbol{P}^{\mathrm{T}}\boldsymbol{A}^{-1}}_{\boldsymbol{G}_{\mathrm{a}}}\hat{\boldsymbol{u}} = \boldsymbol{G}_{\mathrm{a}}\hat{\boldsymbol{u}}, \tag{27}$$

$$\boldsymbol{b} = \underbrace{\left[\boldsymbol{A}^{-1} - \boldsymbol{A}^{-1}\boldsymbol{P}\left(\boldsymbol{P}^{\mathrm{T}}\boldsymbol{A}^{-1}\boldsymbol{P}\right)^{-1}\boldsymbol{P}^{\mathrm{T}}\boldsymbol{A}^{-1}\right]}_{\boldsymbol{G}_{\mathrm{b}}}\hat{\boldsymbol{u}} = \boldsymbol{G}_{\mathrm{b}}\hat{\boldsymbol{u}}. \tag{28}$$

Therefore, for the computing node $\boldsymbol{x}$, its approximate displacement field function can be rewritten as

$$\begin{aligned} u^h(\boldsymbol{x}) &= \boldsymbol{p}^{\mathrm{T}}(\boldsymbol{x})\,\boldsymbol{a} + \boldsymbol{R}^{\mathrm{T}}(\boldsymbol{x})\,\boldsymbol{b} = \left[\boldsymbol{p}^{\mathrm{T}}(\boldsymbol{x})\,\boldsymbol{G}_{\mathrm{a}} + \boldsymbol{R}^{\mathrm{T}}(\boldsymbol{x})\,\boldsymbol{G}_{\mathrm{b}}\right]\hat{\boldsymbol{u}} \\ &= \sum_{I=1}^{NP} \mathit{\Phi}_I(\boldsymbol{x})\,\hat{u}_I = \boldsymbol{\mathit{\Phi}}(\boldsymbol{x})\,\hat{\boldsymbol{u}}, \end{aligned} \tag{29}$$

and the shape function $\boldsymbol{\mathit{\Phi}}(\boldsymbol{x})$ is defined as

$$\boldsymbol{\mathit{\Phi}}(\boldsymbol{x}) = \boldsymbol{p}^{\mathrm{T}}(\boldsymbol{x})\,\boldsymbol{G}_{\mathrm{a}} + \boldsymbol{R}^{\mathrm{T}}(\boldsymbol{x})\,\boldsymbol{G}_{\mathrm{b}}. \tag{30}$$

The equations for calculating the partial derivative of the shape function can be correspondingly given by

$$\begin{cases} \boldsymbol{\Phi}_{,i}(\boldsymbol{x}) = \boldsymbol{p}^{\mathrm{T}}_{,i}(\boldsymbol{x})\,\boldsymbol{G}_{\mathrm{a}} + \boldsymbol{R}^{\mathrm{T}}_{,i}(x)\boldsymbol{G}_{\mathrm{b}} \\ \boldsymbol{\Phi}_{,ij}(\boldsymbol{x}) = \boldsymbol{p}^{\mathrm{T}}_{,ij}(\boldsymbol{x})\,\boldsymbol{G}_{\mathrm{a}} + \boldsymbol{R}^{\mathrm{T}}_{,ij}(x)\boldsymbol{G}_{\mathrm{b}} \end{cases} \tag{31}$$

where

$$\begin{cases} \boldsymbol{R}^{\mathrm{T}}_{,i} = \boldsymbol{R}^{\mathrm{T}}_{,r} r_{,i} \\ \boldsymbol{R}^{\mathrm{T}}_{,ij} = \boldsymbol{R}^{\mathrm{T}}_{,rr} r_{,i} r_{,j} + \boldsymbol{R}^{\mathrm{T}}_{,r} r_{,ij} \end{cases} \tag{32}$$

4. Vertical TBIS based on the plate model

4.1. Bridge mechanical model built by meshless method

First, the mechanical model of the bridge is constructed using the approaches described in 3.1 and 3.2, and the stiffness matrix $\boldsymbol{K}_{\mathrm{b}}$, mass matrix $\boldsymbol{M}_{\mathrm{b}}$, and damping matrix $\boldsymbol{C}_{\mathrm{b}}$ of the bridge can be calculated.

The approximate displacement field established by RPIM can be expressed as

$$\hat{\boldsymbol{u}}_0 = \begin{Bmatrix} u_0 \\ v_0 \\ w_0 \\ \theta_x \\ \theta_y \end{Bmatrix} = \sum_{I=1}^{NP} \varPhi_I \begin{Bmatrix} u_{0I} \\ v_{0I} \\ w_{0I} \\ \theta_{xI} \\ \theta_{yI} \end{Bmatrix} = \boldsymbol{\varPhi}\hat{\boldsymbol{u}} \tag{33}$$

Therefore, we have

$$\boldsymbol{\varepsilon} = \begin{Bmatrix} \boldsymbol{\varepsilon}_0 \\ \boldsymbol{\kappa} \\ \boldsymbol{\gamma}_0 \end{Bmatrix} = \begin{Bmatrix} \boldsymbol{B}_{\mathrm{I}} \\ \boldsymbol{B}_{\mathrm{II}} \\ \boldsymbol{B}_{\mathrm{III}} \end{Bmatrix} \hat{\boldsymbol{u}} = \boldsymbol{B}\hat{\boldsymbol{u}} \tag{34}$$

where $\boldsymbol{B}_{\mathrm{I}}$, $\boldsymbol{B}_{\mathrm{II}}$, and $\boldsymbol{B}_{\mathrm{III}}$ are the derivative matrix of the shape function, which can be written as

$$\boldsymbol{B}_{\mathrm{I}} = \begin{bmatrix} \boldsymbol{B}_{\mathrm{I}}^1 & \boldsymbol{B}_{\mathrm{I}}^2 & \cdots & \boldsymbol{B}_{\mathrm{I}}^I & \cdots & \boldsymbol{B}_{\mathrm{I}}^{NP} \end{bmatrix}, \ \boldsymbol{B}_{\mathrm{I}}^I = \begin{bmatrix} \varPhi_{I,x} & 0 & 0 & 0 & 0 \\ 0 & \varPhi_{I,y} & 0 & 0 & 0 \\ \varPhi_{I,y} & \varPhi_{I,x} & 0 & 0 & 0 \end{bmatrix} \tag{35}$$

$$\boldsymbol{B}_{\mathrm{II}} = \begin{bmatrix} \boldsymbol{B}_{\mathrm{II}}^1 & \boldsymbol{B}_{\mathrm{II}}^2 & \cdots & \boldsymbol{B}_{\mathrm{II}}^I & \cdots & \boldsymbol{B}_{\mathrm{II}}^{NP} \end{bmatrix}, \ \boldsymbol{B}_{\mathrm{II}}^I = \begin{bmatrix} 0 & 0 & 0 & \varPhi_{I,x} & 0 \\ 0 & 0 & 0 & 0 & \varPhi_{I,y} \\ 0 & 0 & 0 & \varPhi_{I,y} & \varPhi_{I,x} \end{bmatrix} \tag{36}$$

$$\boldsymbol{B}_{\mathrm{III}} = \begin{bmatrix} \boldsymbol{B}_{\mathrm{III}}^1 & \boldsymbol{B}_{\mathrm{III}}^2 & \cdots & \boldsymbol{B}_{\mathrm{III}}^I & \cdots & \boldsymbol{B}_{\mathrm{III}}^{NP} \end{bmatrix}, \ \boldsymbol{B}_{\mathrm{III}}^I = \begin{bmatrix} 0 & 0 & \varPhi_{I,y} & 0 & \varPhi_I \\ 0 & 0 & \varPhi_{I,x} & \varPhi_I & 0 \end{bmatrix} \tag{37}$$

where $\varPhi_{I,x}$ and $\varPhi_{I,y}$ denote that $\varPhi_I$ takes first-order partial derivatives with respect to x and y, respectively.

According to Ref. [58], we define $\boldsymbol{K}_\mathrm{b} = \int_\varOmega \boldsymbol{B}^T\boldsymbol{S}\boldsymbol{B}\mathrm{d}\varOmega$, then we have

$$\boldsymbol{K}_\mathrm{b} = \int_\varOmega \boldsymbol{B}^\mathrm{T}\boldsymbol{S}\boldsymbol{B}\mathrm{d}\varOmega = \int_\varOmega \begin{Bmatrix} \boldsymbol{B}_\mathrm{I} \\ \boldsymbol{B}_\mathrm{II} \\ \boldsymbol{B}_\mathrm{III} \end{Bmatrix}^\mathrm{T} \begin{bmatrix} \boldsymbol{A} & \bar{\boldsymbol{B}} & 0 \\ \bar{\boldsymbol{B}} & \boldsymbol{D} & 0 \\ 0 & 0 & \boldsymbol{A}_\mathrm{s} \end{bmatrix} \begin{Bmatrix} \boldsymbol{B}_\mathrm{I} \\ \boldsymbol{B}_\mathrm{II} \\ \boldsymbol{B}_\mathrm{III} \end{Bmatrix} \mathrm{d}\varOmega$$

$$= \int_\varOmega \boldsymbol{B}_\mathrm{I}^\mathrm{T}\boldsymbol{A}\boldsymbol{B}_\mathrm{I} + \boldsymbol{B}_\mathrm{II}^\mathrm{T}\bar{\boldsymbol{B}}\boldsymbol{B}_\mathrm{I} + \boldsymbol{B}_\mathrm{I}^\mathrm{T}\bar{\boldsymbol{B}}\boldsymbol{B}_\mathrm{II} \tag{38}$$

$$+ \boldsymbol{B}_\mathrm{II}^\mathrm{T}\boldsymbol{D}\boldsymbol{B}_\mathrm{II} + \boldsymbol{B}_\mathrm{III}^\mathrm{T}\boldsymbol{A}_\mathrm{s}\boldsymbol{B}_\mathrm{III}\,\mathrm{d}\varOmega \tag{39}$$

Defining $\boldsymbol{M}_\mathrm{b} = \int_\varOmega \boldsymbol{N}_{\varPhi}^\mathrm{T}\boldsymbol{\rho}\boldsymbol{N}_{\varPhi}\mathrm{d}\varOmega$, where $\boldsymbol{N}_{\varPhi}$ is the shape function matrix, which can be expressed as

$$\boldsymbol{N}_{\varPhi} = \begin{bmatrix} \boldsymbol{N}_{\varPhi_1} & \boldsymbol{N}_{\varPhi_2} & \cdots & \boldsymbol{N}_{\varPhi I} & \cdots & \boldsymbol{N}_{\varPhi NP} \end{bmatrix} \tag{40}$$

where

$$\boldsymbol{N}_{\varPhi I} = \begin{bmatrix} \varPhi_I & 0 & 0 & 0 & 0 \\ 0 & \varPhi_I & 0 & 0 & 0 \\ 0 & 0 & \varPhi_I & 0 & 0 \\ 0 & 0 & 0 & \varPhi_I & 0 \\ 0 & 0 & 0 & 0 & \varPhi_I \end{bmatrix} \tag{41}$$

and

$$\boldsymbol{\rho} = \begin{bmatrix} I_0 & 0 & 0 & I_1 & 0 \\ 0 & I_0 & 0 & 0 & I_1 \\ 0 & 0 & I_0 & 0 & 0 \\ I_1 & 0 & 0 & I_2 & 0 \\ 0 & I_1 & 0 & 0 & I_2 \end{bmatrix} \tag{42}$$

where I_0, I_1, and I_2 denote the normal, coupled normal-rotary and rotary inertial coefficients, respectively, and they can be given by

$$(I_0, I_1, I_2) = \int_{-h/2}^{h/2} \rho(z)\left(1, z, z^2\right)dz \tag{43}$$

For the damping matrix $\boldsymbol{C}_\mathrm{b}$, we use Rayleigh damping, i.e.

$$\boldsymbol{C}_\mathrm{b} = a_\mathrm{r}\boldsymbol{M}_\mathrm{b} + b_\mathrm{r}\boldsymbol{K}_\mathrm{b} \tag{44}$$

with

$$a_\mathrm{r} = \frac{2\zeta_\mathrm{b}\omega_1\omega_2}{\omega_1 + \omega_2} \tag{45}$$

$$b_\mathrm{r} = \frac{2\zeta_\mathrm{b}}{\omega_1 + \omega_2}$$

where ω_1 and ω_2 are the first two orders of natural frequencies of the bridge, and ζ_b denotes the bridge damping ratio.

4.2. The block matrices and vectors of the TBIS

In this subsection, the bridge matrices $\boldsymbol{K}_\mathrm{bb}$, $\boldsymbol{M}_\mathrm{bb}$, and $\boldsymbol{C}_\mathrm{bb}$, as well as the train-bridge coupling matrices $\boldsymbol{K}_\mathrm{vb}$, $\boldsymbol{K}_\mathrm{bv}$, $\boldsymbol{C}_\mathrm{vb}$, and $\boldsymbol{C}_\mathrm{bv}$, are calculated using the principle of total potential energy with a stationary value in elastic system dynamics, as described in the Ref. [17, 49]. The load vectors $\boldsymbol{F}_\mathrm{vv}$, $\boldsymbol{F}_\mathrm{vv}$, and $\boldsymbol{F}_\mathrm{bb}$ are also determined using the same principle.

$\boldsymbol{K}_\mathrm{bb}$ contains two components: the stiffness matrix for all spans of the bridge, and the stiffness of the primary suspensions bound to the bridge, i.e.

$$\boldsymbol{K}_\mathrm{bb} = \mathrm{diag}\begin{bmatrix}\boldsymbol{K}_\mathrm{b1} & \boldsymbol{K}_\mathrm{b2} & \cdots & \boldsymbol{K}_{\mathrm{b}M}\end{bmatrix} + {\boldsymbol{N}_\mathrm{bl}}^\mathrm{T}\boldsymbol{k}_\mathrm{b}\boldsymbol{N}_\mathrm{bl} + {\boldsymbol{N}_\mathrm{br}}^\mathrm{T}\boldsymbol{k}_\mathrm{b}\boldsymbol{N}_\mathrm{br} \quad (46)$$

where the subscript M indicates that the bridge has a total of M spans. The matrix $\boldsymbol{k}_\mathrm{b}$ consists of the spring stiffness matrices of the primary suspensions, which are connected to the bridge stiffness matrix through the time-varying shape function matrix $\boldsymbol{N}_\mathrm{b}$. The subscripts l and r denote the left and right wheels of the wheelset, respectively. The expression for $\boldsymbol{k}_\mathrm{b}$ is given by

$$\boldsymbol{k}_\mathrm{b} = \mathrm{diag}\begin{bmatrix}\boldsymbol{k}_\mathrm{b1} & \boldsymbol{k}_\mathrm{b2} & \cdots & \boldsymbol{k}_{\mathrm{b}J}\end{bmatrix} \quad (47)$$

where the subscript J denotes the left (right) wheel of the J-th wheelset, then $\boldsymbol{k}_{\mathrm{b}i}$ can be written as

$$\boldsymbol{k}_{\mathrm{b}i} = \mathrm{diag}\begin{bmatrix}0 & 0 & k_\mathrm{p} & 0 & 0\end{bmatrix} \quad (48)$$

Since wheelsets are constantly moving along the rail, the shape function matrix $\boldsymbol{N}_\mathrm{b}$ also varies with time. Specifically, for $\boldsymbol{N}_\mathrm{bl}$, it can be expressed as

$$
\boldsymbol{N}_{\mathrm{bl}} = \begin{bmatrix}
\vdots & & & \vdots & & & \vdots & & & \vdots & & & \vdots \\
& \mathit{\Phi}_{x,i} & 0 & 0 & 0 & 0 & & \mathit{\Phi}_{x,j} & 0 & 0 & 0 & 0 & \\
& 0 & \mathit{\Phi}_{x,i} & 0 & 0 & 0 & & 0 & \mathit{\Phi}_{x,j} & 0 & 0 & 0 & \\
\cdots & 0 & 0 & \mathit{\Phi}_{x,i} & 0 & 0 & \cdots & 0 & 0 & \mathit{\Phi}_{x,j} & 0 & 0 & \cdots \\
& 0 & 0 & 0 & \mathit{\Phi}_{x,i} & 0 & & 0 & 0 & 0 & \mathit{\Phi}_{x,j} & 0 & \\
& 0 & 0 & 0 & 0 & \mathit{\Phi}_{x,i} & & 0 & 0 & 0 & 0 & \mathit{\Phi}_{x,j} & \\
\vdots & & & \vdots & & & \vdots & & & \vdots & & & \vdots \\
& \mathit{\Phi}_{y,k} & 0 & 0 & 0 & 0 & & \mathit{\Phi}_{y,l} & 0 & 0 & 0 & 0 & \\
& 0 & \mathit{\Phi}_{y,k} & 0 & 0 & 0 & & 0 & \mathit{\Phi}_{y,l} & 0 & 0 & 0 & \\
\cdots & 0 & 0 & \mathit{\Phi}_{y,k} & 0 & 0 & \vdots & 0 & 0 & \mathit{\Phi}_{y,l} & 0 & 0 & \vdots \\
& 0 & 0 & 0 & \mathit{\Phi}_{y,k} & 0 & & 0 & 0 & 0 & \mathit{\Phi}_{y,l} & 0 & \\
& 0 & 0 & 0 & 0 & \mathit{\Phi}_{y,k} & & 0 & 0 & 0 & 0 & \mathit{\Phi}_{y,l} & \\
\vdots & & & \vdots & & & \vdots & & & \vdots & & & \vdots
\end{bmatrix} \tag{49}
$$

where the subscripts x and y represent the wheelset serial numbers, while i, j, k, and l represent the serial numbers of the supporting points within the supporting domain centered on the wheel. For ease of understanding, the shape function matrix at moment t, $\boldsymbol{N}_{\mathrm{bl}}$, can be determined by Fig. 5.

Next, the train-bridge coupling matrix $\boldsymbol{K}_{\mathrm{vb}}$ can be given by

$$
\boldsymbol{K}_{\mathrm{vb}} = \boldsymbol{k}_{\mathrm{vb}}\boldsymbol{N}_{\mathrm{bl}} + \boldsymbol{k}_{\mathrm{vb}}\boldsymbol{N}_{\mathrm{br}} \tag{50}
$$

where $\boldsymbol{N}_{\mathrm{bl}}$, $\boldsymbol{N}_{\mathrm{br}}$ have been given before, and $\boldsymbol{k}_{\mathrm{vb}}$ can be written as

$$
\boldsymbol{k}_{\mathrm{vb}} = \begin{bmatrix}
\boldsymbol{k}_{\mathrm{vb}1} & & & \\
& \boldsymbol{k}_{\mathrm{vb}2} & & \\
& & \ddots & \\
& & & \boldsymbol{k}_{\mathrm{vb}N}
\end{bmatrix} \tag{51}
$$

where the subscript N indicates that there are N vehicles in the train, then $\boldsymbol{k}_{\mathrm{vb}i}$ can be written as

$$
\boldsymbol{k}_{\mathrm{vb}i} = \begin{bmatrix}
\boldsymbol{0} & \boldsymbol{0} \\
\boldsymbol{\lambda}_{\mathrm{vb}} & \boldsymbol{0} \\
\boldsymbol{0} & \boldsymbol{\lambda}_{\mathrm{vb}}
\end{bmatrix} \tag{52}
$$

with

$$
\lambda_{\mathrm{vb}} = \begin{bmatrix}
0 & 0 & -k_{\mathrm{p}} & 0 & 0 & 0 & 0 & -k_{\mathrm{p}} & 0 & 0 \\
0 & 0 & -k_{\mathrm{p}}L_{\mathrm{t}} & 0 & 0 & 0 & 0 & k_{\mathrm{p}}L_{\mathrm{t}} & 0 & 0
\end{bmatrix} \tag{53}
$$

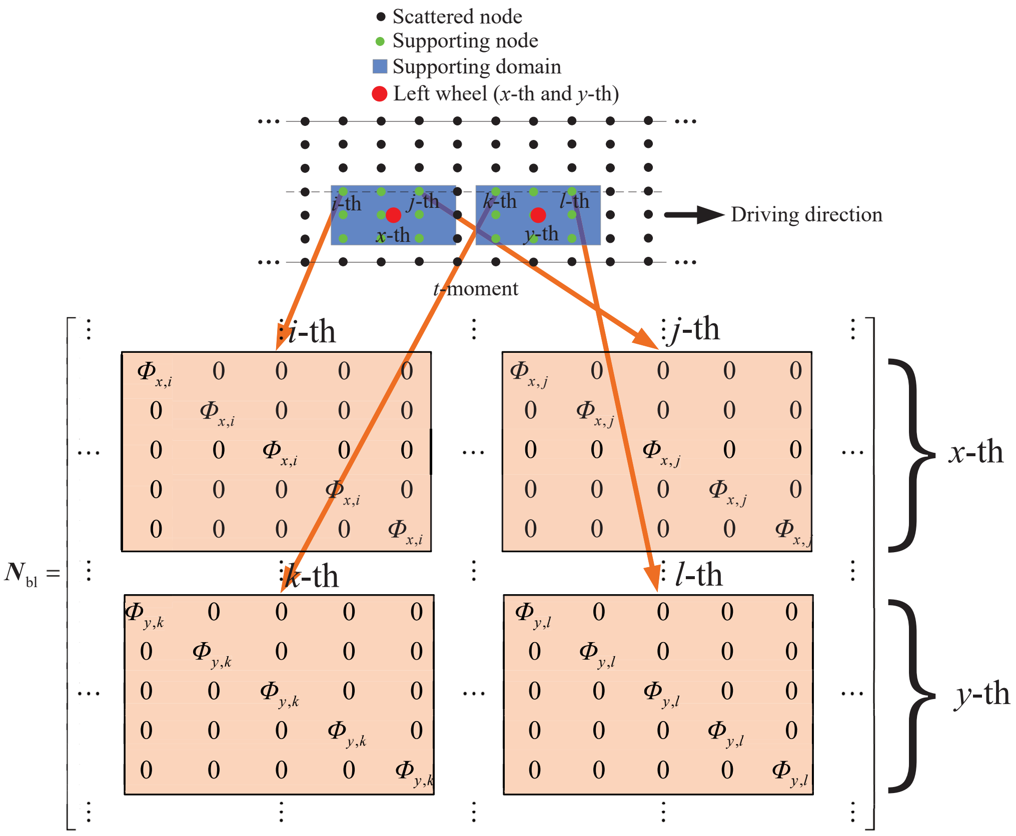

Figure 5: The shape function matrix $\boldsymbol{N}_{\mathrm{bl}}$ at moment t.

and transposing $\boldsymbol{K}_{\mathrm{vb}}$ gives $\boldsymbol{K}_{\mathrm{bv}}$, i.e. $\boldsymbol{K}_{\mathrm{bv}} = {\boldsymbol{K}_{\mathrm{vb}}}^{\mathrm{T}}$.

For the mass matrix $\boldsymbol{M}_{\mathrm{bb}}$, it has a similar form to $\boldsymbol{K}_{\mathrm{bb}}$, i.e.

$$\boldsymbol{M}_{\mathrm{bb}} = \mathrm{diag}\begin{bmatrix}\boldsymbol{M}_{\mathrm{b1}} & \boldsymbol{M}_{\mathrm{b2}} & \cdots & \boldsymbol{M}_{\mathrm{b}M}\end{bmatrix} + {\boldsymbol{N}_{\mathrm{bl}}}^{\mathrm{T}}\boldsymbol{m}_{\mathrm{b}}\boldsymbol{N}_{\mathrm{bl}} + {\boldsymbol{N}_{\mathrm{br}}}^{\mathrm{T}}\boldsymbol{m}_{\mathrm{b}}\boldsymbol{N}_{\mathrm{br}} \tag{54}$$

with

$$\boldsymbol{m}_{\mathrm{b}} = \mathrm{diag}\begin{bmatrix}\boldsymbol{m}_{\mathrm{b1}} & \boldsymbol{m}_{\mathrm{b2}} & \cdots & \boldsymbol{m}_{\mathrm{b}J}\end{bmatrix} \tag{55}$$

$$\boldsymbol{m}_{\mathrm{b}i} = \mathrm{diag}\begin{bmatrix}0 & 0 & m_{\mathrm{w}} & 0 & 0\end{bmatrix} \tag{56}$$

For the damping matrices $\boldsymbol{C}_{\mathrm{bb}}$, $\boldsymbol{C}_{\mathrm{bv}}$, and $\boldsymbol{C}_{\mathrm{vb}}$, we can obtain them by replacing $\boldsymbol{K}_{\mathrm{bb}}$, $\boldsymbol{K}_{\mathrm{bv}}$, and $\boldsymbol{K}_{\mathrm{vb}}$ with the corresponding damping coefficients.

For the load vectors $\boldsymbol{F}_{\mathrm{vv}}$ and $\boldsymbol{F}_{\mathrm{bb}}$, we have

$$\boldsymbol{F}_{\mathrm{vv}} = \boldsymbol{k}_{\mathrm{vb}}\boldsymbol{u}_{\mathrm{irrl}} + \boldsymbol{c}_{\mathrm{vb}}\boldsymbol{v}_{\mathrm{irrl}} + \boldsymbol{k}_{\mathrm{vb}}\boldsymbol{u}_{\mathrm{irrr}} + \boldsymbol{c}_{\mathrm{vb}}\boldsymbol{v}_{\mathrm{irrr}} \tag{57}$$

$$\begin{split}\boldsymbol{F}_{\mathrm{bb}} = & -{\boldsymbol{N}_{\mathrm{bl}}}^{\mathrm{T}}\boldsymbol{c}_{\mathrm{b}}\boldsymbol{u}_{\mathrm{irrl}} - {\boldsymbol{N}_{\mathrm{bl}}}^{\mathrm{T}}\boldsymbol{k}_{\mathrm{b}}\boldsymbol{v}_{\mathrm{irrl}} - {\boldsymbol{N}_{\mathrm{bl}}}^{\mathrm{T}}\boldsymbol{m}_{b}\boldsymbol{a}_{\mathrm{irrl}} - {\boldsymbol{N}_{\mathrm{bl}}}^{\mathrm{T}}\boldsymbol{g}_{\mathrm{irrl}} \\ & - {\boldsymbol{N}_{\mathrm{br}}}^{\mathrm{T}}\boldsymbol{k}_{\mathrm{b}}\boldsymbol{u}_{\mathrm{irrr}} - {\boldsymbol{N}_{\mathrm{br}}}^{\mathrm{T}}\boldsymbol{c}_{\mathrm{b}}\boldsymbol{v}_{\mathrm{irrr}} - {\boldsymbol{N}_{\mathrm{br}}}^{\mathrm{T}}\boldsymbol{m}_{b}\boldsymbol{a}_{\mathrm{irrr}} - {\boldsymbol{N}_{\mathrm{br}}}^{\mathrm{T}}\boldsymbol{g}_{\mathrm{irrr}}\end{split} \tag{58}$$

where $\boldsymbol{c}_{\mathrm{vb}}$ can be obtained by replacing k_{p} in $\boldsymbol{k}_{\mathrm{vb}}$ with c_{p}. Similarly, $\boldsymbol{c}_{\mathrm{b}}$ can be obtained by replacing k_{p} in $\boldsymbol{k}_{\mathrm{b}}$ with c_{p}. $\boldsymbol{u}_{\mathrm{irr}}$, $\boldsymbol{v}_{\mathrm{irr}}$, and $\boldsymbol{a}_{\mathrm{irr}}$ are the corresponding rail irregularity (i.e., vertical displacement), rail velocity, and rail acceleration of the train at moment t. Taking $\boldsymbol{u}_{\mathrm{irrl}}$ as an example,it can be written as

$$\boldsymbol{u}_{\mathrm{irrl}} = \begin{bmatrix}\boldsymbol{u}_{\mathrm{irrl1}} & \boldsymbol{u}_{\mathrm{irrl2}} & \ldots & \boldsymbol{u}_{\mathrm{irrl}J}\end{bmatrix}^{\mathrm{T}} \tag{59}$$

with

$$\boldsymbol{u}_{\mathrm{irrl}i} = \begin{bmatrix}0 & 0 & u_{\mathrm{l}i} & 0 & 0\end{bmatrix} \tag{60}$$

where $u_{\mathrm{l}i}$ denotes the rail irregularity corresponding to the left wheel of the i-th wheel pair at moment t. $\boldsymbol{v}_{\mathrm{irr}}$ and $\boldsymbol{a}_{\mathrm{irr}}$ can be obtained by taking first-order and second-order differences on $\boldsymbol{u}_{\mathrm{irr}}$.

By now, we solve all block matrices in Eq. (6). Then we can get the displacement, velocity, and acceleration of the train and bridge at each time step by Newmark-β method.

5. Rail irregularity

To facilitate a comparison with the model discussed in Ref. [16], we adopt German low-interference rail irregularity spectrum in Ref. [16] for this study, which applies to high-speed railway with speeds of 250 km/h and above. The power spectral density of rail irregularity primarily encompasses spectra from China, Germany, and United States. However, different rail irregularity spectrums do not affect the conclusions of model comparisons.

The spectrum is used to generate the vertical rail irregularity [59], i.e.

$$S_{\mathrm{V}} = \frac{A_{\mathrm{v}}}{\left(\Omega^2 + \Omega_{\mathrm{r}}^2\right)\left(\Omega^2 + \Omega_{\mathrm{c}}^2\right)} \tag{61}$$

where,for the case of low-interferenc, the parameters $\Omega_{\mathrm{r}} = 0.0206$, $\Omega_{\mathrm{c}} = 0.8246$, and $A_{\mathrm{v}} = 4.032 \times 10^{-7}$. The trigonometric series method [60] is used to generate the rail irregularity and the spatial frequency $\Omega \in [0.05, 0.3]$ rad/m.

Using Eqs. (62) and (63) to modulate the rail irregularity on the bridge [61], i.e.

$$z_{\mathrm{r}}(x) = \Phi(x)\hat{z}_{\mathrm{r}}(x) \tag{62}$$

$$\Phi(x) = \begin{cases} 0.5\left(1+\sqrt{c}\right) + 0.5\left(1-\sqrt{c}\right)\sin\left(\pi L_0^{-1}\left(x + 1.5L_0\right)\right) & -L_0 \leq x < 0 \\ \sqrt{c} & 0 \leq x < L \\ 0.5\left(1+\sqrt{c}\right) + 0.5\left(1-\sqrt{c}\right)\sin\left(\pi L_0^{-1}\left(-x - L - 0.5L_0\right)\right) & L \leq x < L + L_0 \\ 1 & \text{other} \end{cases} \tag{63}$$

where $\hat{z}_{\mathrm{r}}(x)$ is the original rail irregularity generated by trigonometric series method, and $\Phi(x)$ is the modulation function. c is the modulation coefficient, L is the total length of the rail irregularity, and L_0 is the modulation transition length. In this study, c is taken as 0.7, L_0 is taken as 20 m.

6. Numerical examples

Based on the previous sections, we construct a vertical TBIS consisting of a 1-span 32-meter simply supported bridge and a train, as depicted in Fig. (6). In TBIS programs, simply supported box girders are commonly used for bridges, where different spans are not directly connected to each other, but the response is transmitted through the rails and piers. To more directly highlight the differences between the plate and beam models, we have excluded the track and pier models, resulting in no interaction between different span bridges. Therefore, a single-span bridge model is sufficient to achieve the research objectives. Meanwhile, it allows for more detailed mesh division, which is particularly beneficial when dealing with limited computing power. The train consists of 4 cars arranged as motor car + trailer car +

trailer car + motor car. German power spectrum is used to generate the rail irregularity for a total length of 1000 m. To ensure the stability of the initial condition, the train starts at 150 m at the first car distance from the bridgehead, and the calculation is over after the first car passes the bridge 150 m. The train speed is 300 Km/h. We list the main train parameters in Tab. 2.

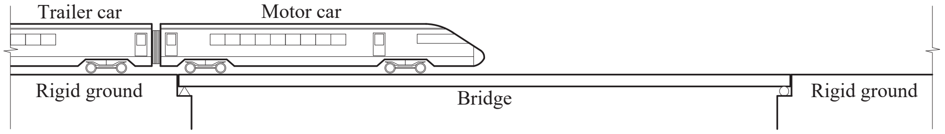

Figure 6: The TBIS of the numerical example.

Table 2: The parameters of cars.

Parameter	Unit	Motor car/Trailer car
m_{c}	kg	4.4×10^4 / 4.8×10^4
J_{c}	$\mathrm{kg} \cdot \mathrm{m}^2$	2.7×10^6 / 2.7×10^6
m_{t}	kg	2.4×10^3 / 3.2×10^3
J_{t}	$\mathrm{kg} \cdot \mathrm{m}^2$	2.2×10^3 / 7.2×10^3
m_{w}	kg	1.2×10^3
k_{s}	N/m	6×10^5 / 8×10^5
c_{s}	$\mathrm{N} \cdot \mathrm{s/m}$	8×10^4 / 9×10^4
k_{p}	N/m	1.4×10^6 / 2.08×10^6
c_{p}	$\mathrm{N} \cdot \mathrm{s/m}$	8×10^4 / 6×10^4
L_{c}	m	8.6875/8.6875
L_{t}	m	1.25/1.25

We consider two different approaches to model the bridge: One of them is FEM using two-node four-DOF Euler beam element [16], the other is the meshless method discussed in the previous section. The comparison between the beam model and plate model presented in this paper is, in fact, a comparison between the conventional TBIS and the proposed modified TBIS. In previous studies of TBIS, including the work cited in Ref. [1, 16, 17, 62], utilized Euler beams rather than Timoshenko beams to model simply supported girder bridges. In our work, the plate model-based TBIS is an improvement upon the approach introduced in Ref. [16]. The earlier literature simplified simply supported girder bridges to Euler beams, leading us to employ Euler beams-Reissner-Mindlin plates for the comparison in our study. The material properties of the bridge are as follows: Young's modulus is 3.451×10^{10} N/m^2, Poisson's ratio is 0.2, density is 2.65×10^3 kg/m^3, damping ratio is 0.05, and bridge width is 13 m.

In the FEM modeling, the bridge is divided into 64 equidistant elements. For the meshless method, a total of 27×65 nodes are distributed equidistantly in both the x and y directions, and the discretization of the model by FEM and RPIM can be seen in Fig. 7. In RPIM, particularly for two-dimensional problems, the quadratic complete polynomial basis functions can be written as

$$\boldsymbol{p}(\boldsymbol{x}) = \begin{bmatrix} 1 & x & y & x^2 & xy & y^2 \end{bmatrix}^{\mathrm{T}}. \tag{64}$$

The scale influence factor χ, which is used to control the size of the supporting domain, is typically chosen within the range of 2.0 to 3.0. As suggested by Ref. [39, 63], in this paper, a specific value of 2.4 is adopted. At this setting, the support domain can accommodate up to 25 supporting nodes. At the end of this section, we will perform a sensitivity study on these parameters. Finally, the TBIS can be established as Fig. 8. The time step length for Newmark-β method is set to $\Delta_{\mathrm{t}} = 6 \times 10^{-4}$ s, i.e., the train runs $\Delta_{\mathrm{L}} = 0.05$ m for each time step. Thus, a total of 8524 time steps are required to complete the entire journey.

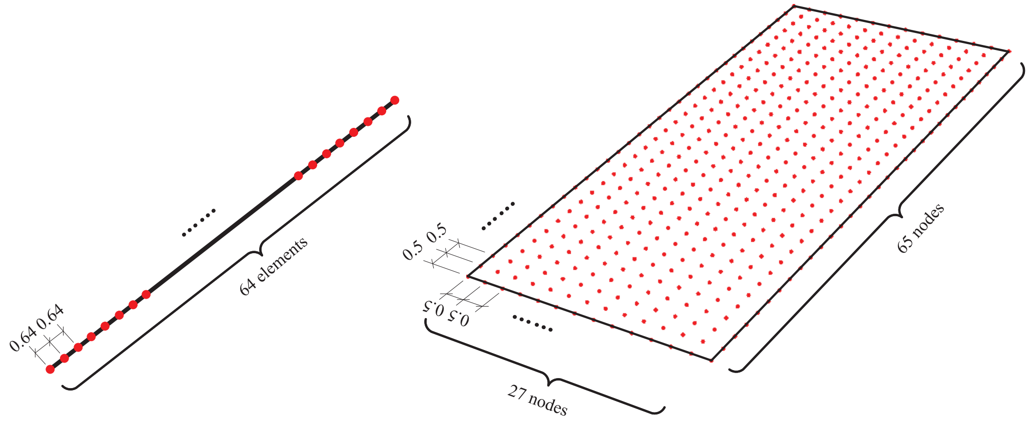

Finite element discretization

Meshless discretization

Figure 7: Discretization of the model by FEM and RPIM.

As most real engineering bridges are box girders, accurate determination of plate thickness parameters based on current literature is challenging.

Moreover, the width-thickness ratio W_t significantly affects the vibration of the plate. To address this, we calculate the dynamic responses of the plate model for different W_t values and compare them with the beam model. It is important to note that the cross-sectional area and flexural stiffness of the beam model vary with W_t. In both finite element and meshless methods, during the numerical modeling of Reissner-Mindlin plate, displacement and rotating angle are interpolated independently. This approach can introduce a new challenge known as shear locking. In civil engineering, the ratio of thickness to width, denoted as h/a, is commonly employed to classify plate structures as either thin or thick. Generally, when $h/a < 0.125$, a plate is considered thin; otherwise, it is categorized as thick or medium-thick. Shear locking tends to increase significantly when h/a is substantially less than 0.125. However, the width-to-thickness ratios investigated in this study range from 4 to 7, ensuring a minimum h/a of 0.143, which is greater than 0.125. Consequently, this paper eliminates the necessity to address shear locking concerns. In case shear locking does become an issue, reduced integration can be employed as a mitigating measure, if necessary.

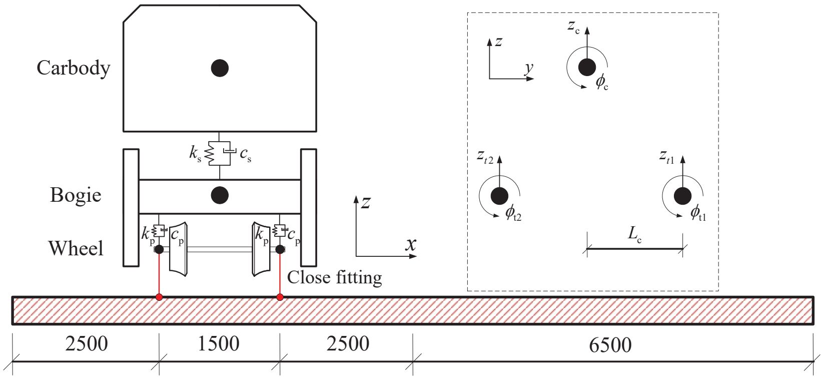

Figure 8: The TBIS based on plate model established by RPIM.

Fig. 9 shows the curve of mid-span vertical displacement of the two models changing with time when $W_\mathrm{t} = 5$. The beam model is constructed in the same way as we used in the Ref. [64], i.e., each span is modeled separately. In this modeling approach, each span of bridge (the width is 13 m, length is 32 m, and height is 2.6 m) is simplified into Euler beam elements. In terms of size, it seems to make more sense to simplify it to a plate. The beam model curve is plotted at a width coordinate of -0.5 m. The width coordinates ranging from 0 m to 13 m correspond to the changes in mid-span vertical displacement of the plate model along the width direction of the bridge. For the plate model, it can be clearly observed that the vertical displacement gradually increases in the width direction 0 m to 13 m. This occurs because, in this specific example, the train is set to run on the side of the width direction within the range of 0 $\sim$ 6.5 m. The specific position and wheel trajectories are depicted in Fig. 8. By comparing the projected curves of the beam model and plate model, it can be observed that the overall trends are similar. The bridge begins to bend down as the train drives onto it, and it starts to reset when the train begins to exit the bridge. Once all the cars of the train have completely crossed the bridge, the bridge enters a state of free vibration, and the amplitude gradually decreases due to the presence of damping. Eventually, the bridge returns to its initial state. Although both the beam model and plate model exhibit similar dynamic trends, substantial disparities in their response values are evident. These discrepancies can be attributed to differences in mechanical assumptions. Mechanically, beam and plate structures, characterized by significantly smaller scales in two directions and one direction, respectively, allow certain assumptions to be introduced in the analysis. These assumptions aim to simplify beams and plates into one-dimensional and two-dimensional problems, respectively, thereby facilitating their analytical solutions. In the specific example considered, the dimensions in the thickness direction are notably smaller than those in the width and length directions. Consequently, certain mechanical assumptions applicable to beam structures become invalid, leading to distorted calculation results. This discrepancy represents a critical factor contributing to the observed differences between the two models.

Fig. 10 displays the mid-span vertical displacements for different values of W_{t} (4, 5, 6, 7) in the models. The plot utilizes three colors: the red curve represents the beam model, while the blue and gray curves represent the plate model. Specifically, the blue curve corresponds to the displacements at the width coordinates of 0 m and 13 m, while the gray curve represents the displacement between 0 m and 13 m. By observing the variation in the longitudinal scale, it can be inferred that the mid-span vertical displacement increases with an increase in W_{t}. However, it is noteworthy that the increase is more pronounced in the beam model compared to the plate model. Furthermore, the amplitude of free vibration is much larger in the beam model than in the plate model. Consequently, larger values of W_{t} result in greater discrepancies between the two models. It is important to acknowledge that due to computational limitations, our simulation only considers a one-span

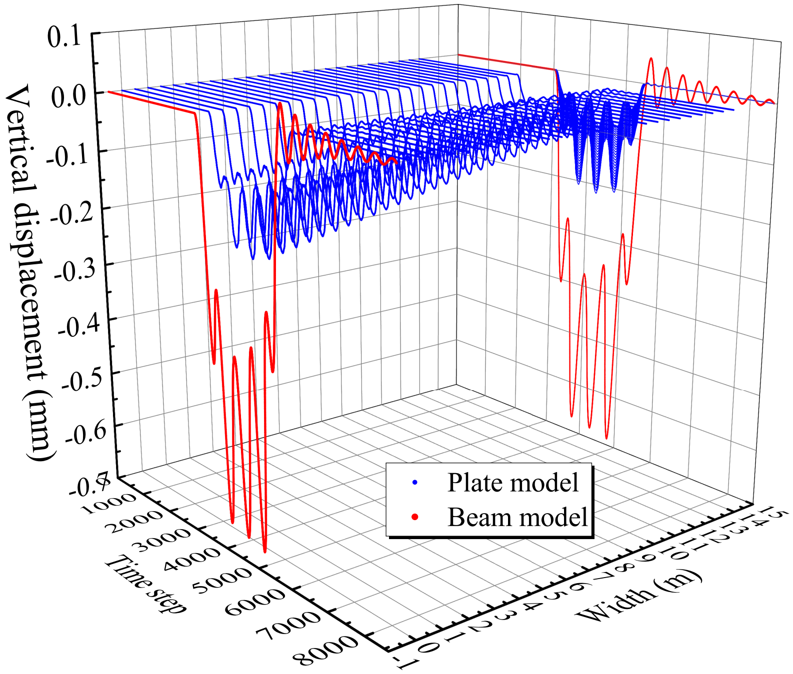

Figure 9: Curves of vertical displacements at mid-span with time for the plate and beam models ($W_{\mathrm{t}} = 5$).

bridge. In this context, utilizing a beam model for the simulation is not rigorous, considering the dimensions of the bridge. On the other hand, the proposed plate model in this paper provides more realistic data. For instance, while the beam model can only represent the overall displacement of a bridge section, the plate model offers variation in displacement along the width direction. The blue curve depicts the maximum and minimum vertical displacements of the section, while the gray curve envelopes the blue curve, demonstrating the variation in vertical displacement from one side of the bridge to the other.

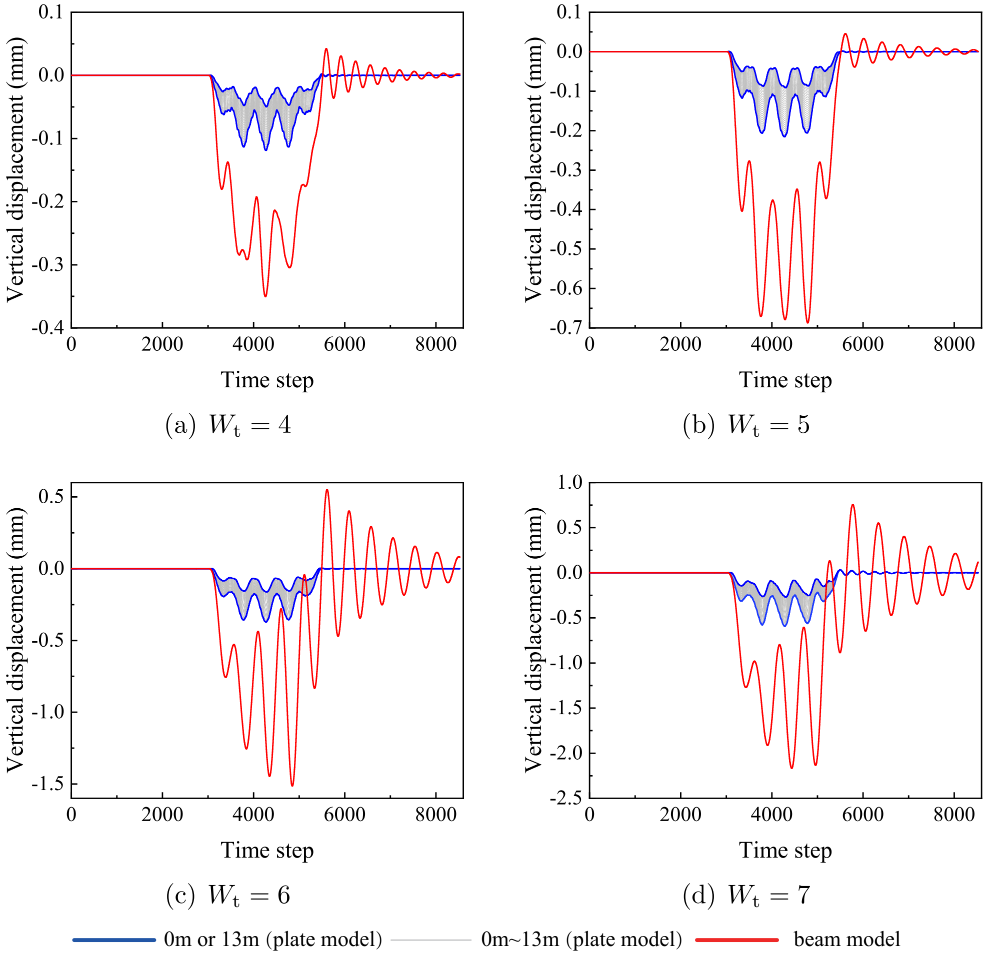

(a) $W_{\rm t} = 4$

(b) $W_{\rm t} = 5$

(c) $W_{\rm t} = 6$

(d) $W_{\rm t} = 7$

Figure 10: Mid-span vertical displacement of bridge built by plate model and beam model with different width-thickness ratio $W_{\rm t}$

The trend analysis of the bridge span is performed and presented in Fig. 11. Upon examining the figure, it is evident that the analysis results of the beam model only provide the overall acceleration variation at the mid-span, whereas the plate model offers more detailed information. In the plate model, a noticeable disparity in acceleration variation can be observed between the traffic side and the other side. Furthermore, on the traffic side, the acceleration variation at the corresponding position of the wheel is more pronounced, with peaks reaching 0.5 m/s^2. In terms of the overall trend, the mid-span acceleration variation increases with an increase in W_t for both models. However, the peak acceleration in the beam model is smaller than that in the plate model. Naturally, the two models exhibit similarity when considering only peak acceleration values when Wt is lager. However, when examined in the frequency domain, variations may become evident. Furthermore, as W_t increases, the disparity in vertical displacement between the two models also magnifies. Consequently, we believe that the plate model continues to maintain its competitive edge. As a result, the plate model can provide more comprehensive response information for targeted analysis and design.

The analysis results of the carbody acceleration, specifically the vertical acceleration of the first motor car, are presented in Fig. 12. It is evident that the carbody acceleration exhibits a high degree of similarity between the two models, with only slight variations observed during the bridge crossing phase as W_t changes. This suggests that the bridge model has minimal influence on the carbody acceleration, which is primarily governed by rail irregularities. Since the same rail irregularities are employed in both models, the obtained figures exhibit similar patterns.

To validate the applicability of the proposed meshless computational framework, we conducted computations of the bridge ($W_\mathrm{t} = 5$) response at various train speeds, as depicted in Figs. 13 and 14. The figures reveal a gradual increase in the fluctuation of the bridge response with the rise in speed, consistent with analogous observations in the Ref. [16]. We plot the mid-span displacements and acceleration under trains comprising 6, 8, and 10 cars traversing the bridge in Figs. 15 and 16. It is evident that the number peak responses increase with the number of cars, indicating the adaptability of the proposed model to diverse train compositions. In Figs. 17 and 18, we reduce the discretization accuracy and plotted the mid-span responses for the final span of the bridge with 2, 3, and 4 spans. With an increase in the number of spans, the mid-span responses of the final span

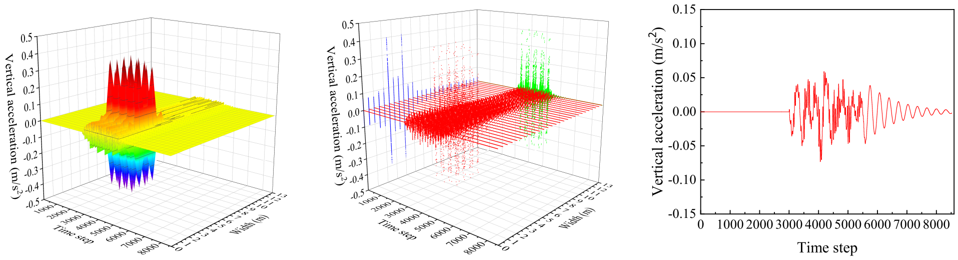

(a) $W_{\mathrm{t}} = 4$

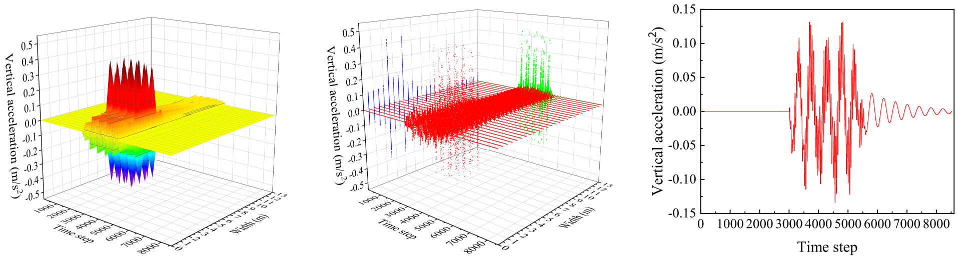

(b) $W_{\mathrm{t}} = 5$

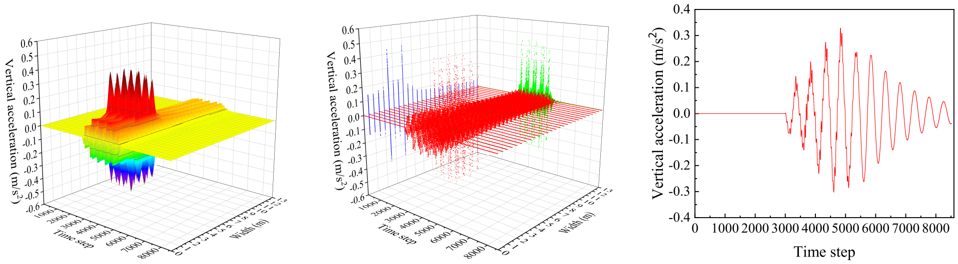

(c) $W_{\mathrm{t}} = 6$

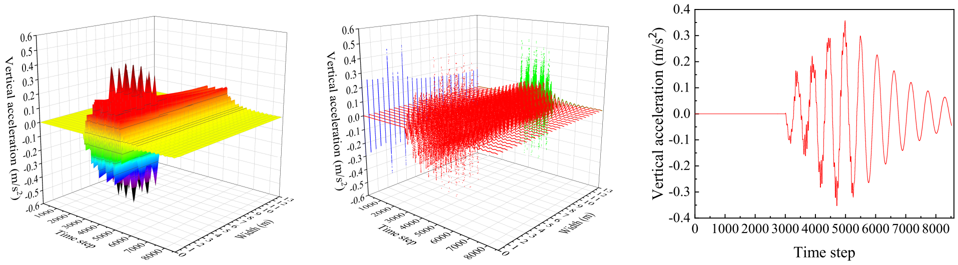

(d) $W_{\mathrm{t}} = 7$

Figure 11: Mid-span vertical acceleration of bridge built by plate model and beam model with different width-thickness ratio W_{t} (The figures on the left and center represent the mid-span acceleration surface and scatter point figure of the plate model, respectively. The figures on the right display the mid-span acceleration figure of the beam model)

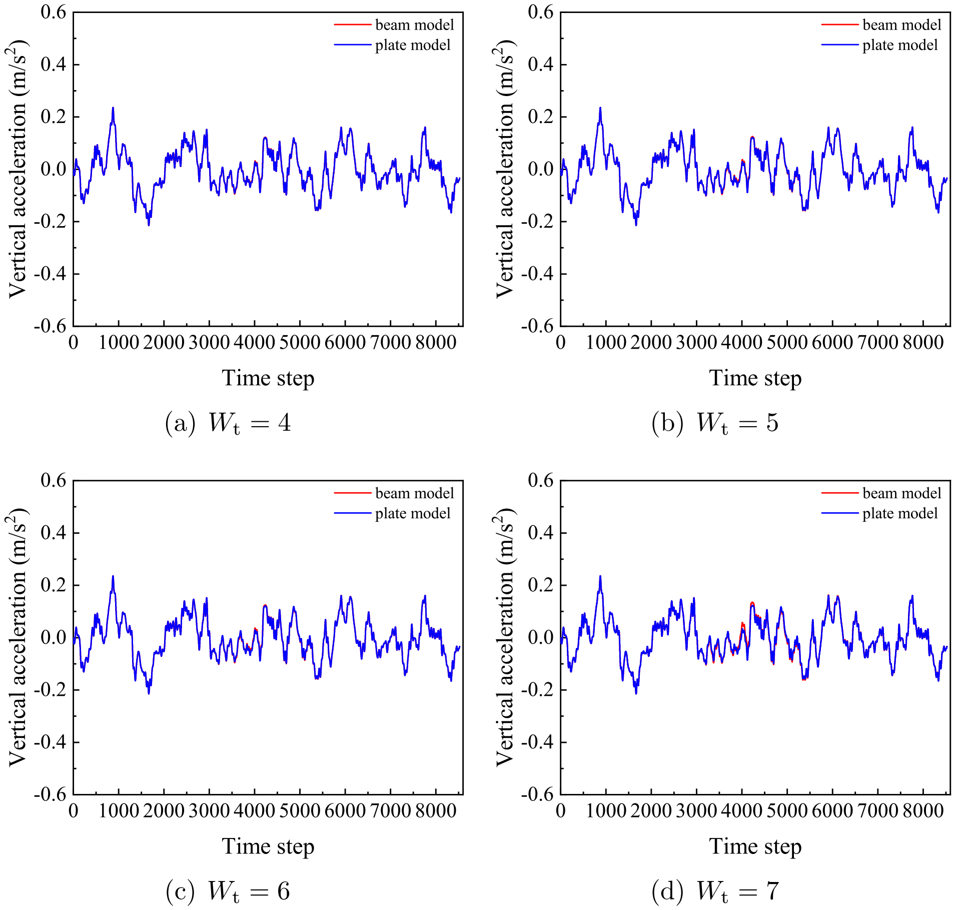

(a) $W_{\mathrm{t}} = 4$

(b) $W_{\mathrm{t}} = 5$

(c) $W_{\mathrm{t}} = 6$

(d) $W_{\mathrm{t}} = 7$

Figure 12: Vertical acceleration of the car body of the first motor car under plate model and beam model with different width-thickness ratio W_{t}

gradually rise. This is attributed to the increased number of spans, causing the train to experience more bridge influence before reaching the last span, thereby resulting in a slight elevation in the response of the last span bridge. Hence, the computational framework presented in this paper demonstrates commendable applicability.

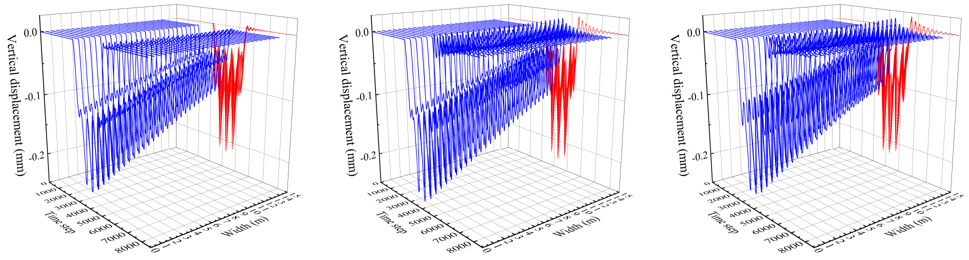

(a) 350 Km/h (b) 400 Km/h (c) 450 Km/h

Figure 13: Mid-span vertical displacement of the bridge under different train speeds ($W_\mathrm{t} = 5$).

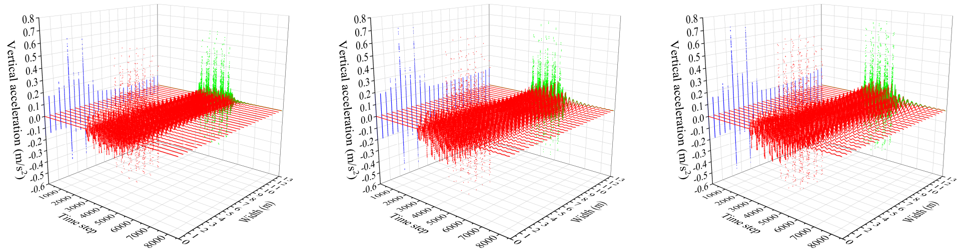

(a) 350 Km/h (b) 400 Km/h (c) 450 Km/h

Figure 14: Mid-span vertical acceleration of the bridge under different train speeds ($W_\mathrm{t} = 5$).

The stability and convergence of numerical simulation methods play crucial roles in determining their widespread applicability to such problems. Hence, we investigate the sensitivity of the structural response to discretization density and the scale influence factor χ. In Tab. 3, the vertical displacements of the bridge at coordinates $(0, 16)$ during the initial passage of the first motor car onto the bridge mid-span are provided. The results indicate that as the density of meshless discretization nodes increases, the structural response gradually converges and stabilizes regionally, ultimately reaching

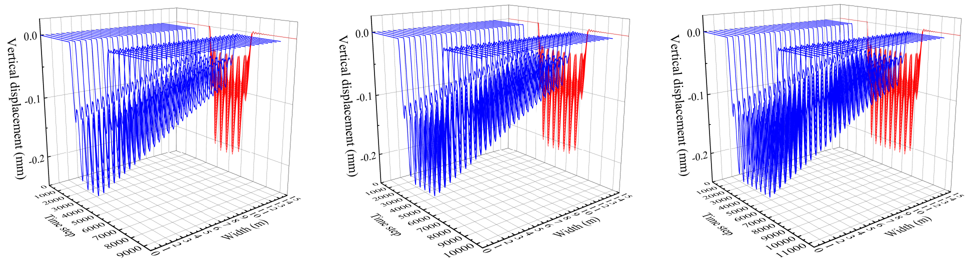

(a) 6 cars (b) 8 cars (c) 10 cars

Figure 15: Mid-span vertical displacement of the bridge under different number of cars ($W_t = 5$).

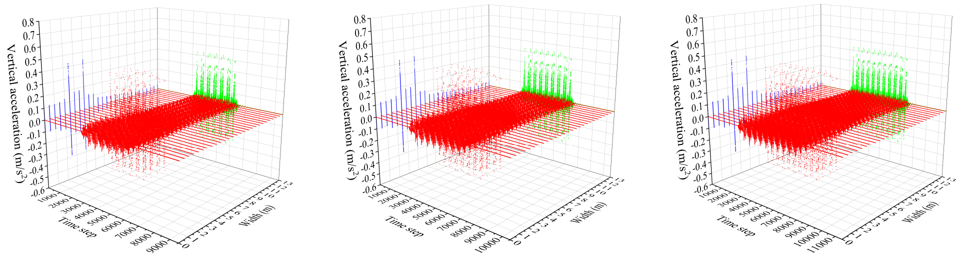

(a) 6 cars (b) 8 cars (c) 10 cars

Figure 16: Mid-span vertical acceleration of the bridge under different number of cars ($W_t = 5$).

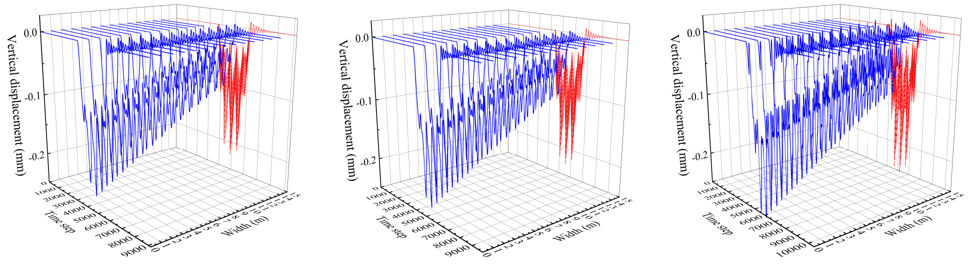

(a) 2 spans (b) 3 spans (c) 4 spans

Figure 17: Vertical displacement of the last span bridge with different number of spans ($W_t = 5$).

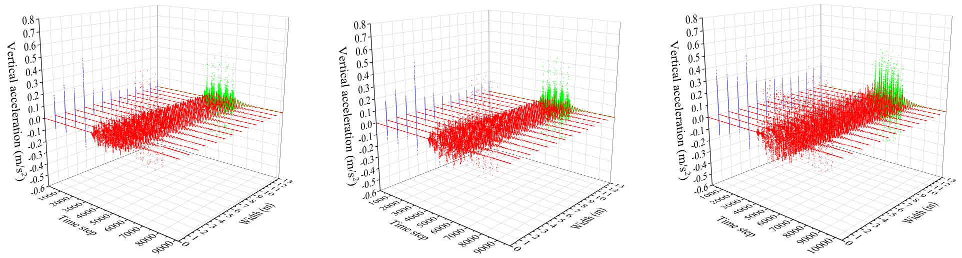
(a) 2 spans (b) 3 spans (c) 4 spans

Figure 18: Vertical acceleration of the last span bridge with different number of spans ($W_t = 5$).

a converged value around -1.31×10^{-4} m. The scale influence factor χ, also affects the convergence speed. The fastest convergence is observed at $\chi = 3$. However, regardless of χ in the range of $2 \sim 3$, the structural response successfully converges and stabilizes with a 27×65 meshless node configuration. Consequently, the chosen value of $\chi = 2.4$ in our numerical examples is deemed appropriate in this study. This leads us to the conclusion that the proposed computational framework exhibits reliable stability and convergence.

Table 3: Sensitivity of stability and convergence for the structural vertical displacement ($\times 10^{-4}$ m) at coordinates (0,16) to the discretization density and scale influence factor χ when the first motor car runs into mid-span of the bridge ($W_t = 5$).

χ	27×65	14×65	27×33	14×33	14×17	8×17
2.0	-1.130	-1.131	-1.130	-1.130	-1.128	-1.125
2.2	-1.130	-1.130	-1.127	-1.128	-1.117	-1.116
2.4	-1.131	-1.131	-1.128	-1.128	-1.115	-1.114
2.6	-1.131	-1.132	-1.129	-1.129	-1.118	-1.116
2.8	-1.130	-1.132	-1.129	-1.130	-1.126	-1.123
3.0	-1.130	-1.131	-1.130	-1.130	-1.129	-1.127

For the computational efficiency, an increase in model dimensionality (from one-dimensional to two-dimensional) almost inevitably leads to a reduction in computational efficiency. We list the CPU computation times for various models in Tab. 4. While computational efficiency experiences a significant decrease, it is not an insurmountable challenge. In our previous work, we successfully integrated various types of neural networks into the train-bridge system computational framework to predict dynamic responses, and the related results have been published [65–67]. These artificial intelligence agents effectively accelerate computations. Therefore, a similar approach could be considered to address the efficiency problem in our future work.

Table 4: CPU computation time for different models with different number of nodes.

Model	Node	Time (s)
Beam model	26	1.101
	51	3.046
	101	5.285
Plate model	8×17	116.750
	14×33	563.506
	27×65	3216.619

Until this juncture in the paper, we have verified the dynamic system of the vehicle coupled with the plate structure. We now propose a more refined system, as illustrated in Fig. 19, based on the findings of this study. Utilizing the FSDT-RPIM framework introduced in this paper, the top, web, and bottom plates with varying thickness [68] of the box girder bridge can be simulated and separately assembled, culminating in a higher level box girder model. The TBIS validated in this paper can be readily employed to couple the vehicle with the top plate. Simultaneously, the beam structure can be employed to simulate the pier and assembled with the bottom slab. This approach facilitates the construction of a higher level TBIS. The viability of this concept can be substantiated in future research. However, it is essential to note that the utilization of RPIM for discretizing the plate model in this study does not preclude the use of other methods. This research has demonstrated the applicability of meshless methods in the TBIS domain. Classical meshless methods such as the moving least square method, reproducing kernel particle method, and general finite difference method can be incorporated into the computational framework proposed in this paper. They only differ slightly in the imposition of boundary conditions and the wheel-plate coupling relationship. Thus, researchers can choose different methods based on specific needs when addressing this type of problem.

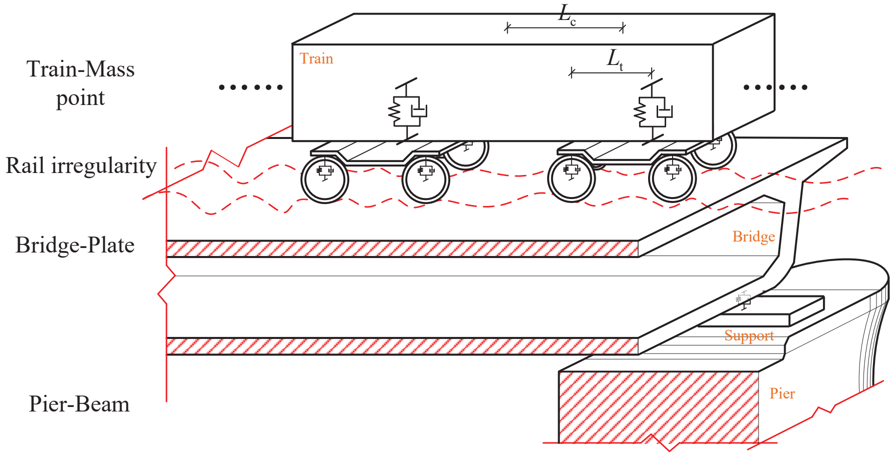

Figure 19: A higher level TBIS with multiple plates.

7. Conclusions

In this study, we propose a modified vertical train-bridge interaction system. To model the bridge, we utilize radial point interpolation method, a meshless method, while incorporating first-order shear deformation theory to represent the displacement field of the bridge. We provide the form of each block matrix in the coupled dynamics equations of the presented system. This is the first attempt to combine FSDT and RPIM to build a plate model for bridge simulate within TBIS. Furthermore, we conduct an analysis of the mid-span vertical displacement, vertical acceleration, and carbody acceleration for both the beam model and the proposed plate model. A comparison between the two models is performed, and the results yield the following findings:

(1) The analysis of the mid-span vertical displacements reveals that they exhibit an increasing trend as the width-thickness ratio increases. It is noteworthy that for lower span numbers, the mid-span vertical displacements obtained from the beam model are notably larger than those obtained from the plate model. In contrast, the plate model offers the advantage of providing more detailed information, such as the vertical displacement at any specific point within the bridge surface.

(2) The mid-span vertical acceleration exhibits an upward trend as the width-thickness ratio increases. Notably, the plate model surpasses the beam model in terms of its ability to provide vertical acceleration information at every point along the entire bridge surface. Additionally, it is observed that the vertical acceleration is greater on the traffic side compared to the opposite side. Moreover, the vertical acceleration amplitude is significantly larger at the section of the bridge surface in contact with the wheels compared to other locations. In contrast, the beam model can only offer the overall vertical acceleration of the bridge, limiting its utility in targeted analysis and design of the bridge.

(3) The carbody acceleration exhibits minimal dependence on the bridge model and width-thickness ratio. Instead, it is primarily influenced by track irregularities.

As we mentioned in Section 1, this study establishes a theoretical foundation and validates the feasibility of implementing TBIS with precision bridge modeling within a unified platform. In engineering practice, a majority of simply supported girder bridges employ box girder structures, ~~which prove challenging to simulate accurately using either beam or single-plate models. However, this paper demonstrates the feasibility of train-plate coupling, which implies that it is also feasible to model box girders using multiple plates and embed them in TBIS. For instance, the top, bottom, and web plates of a box girder can be simulated by four plates. Such simulations exhibit high accuracy, on par with solid element modeling. Meanwhile, beam model features only a single point in the width direction, limiting further customization of boundary conditions. Conversely, the platemodel utilized in this study permits intricate adjustments in the width direction. In particular, with the introduction of multi-plate structures and piers, it is possible to establish interrelationships between the bottom plate and the piers that are compatible with actual situation. This will directly affect the accuracy of the TBIS. Additionally, there is potential to expand the internal structure of the system. For instance, the track slab could also be modeled using the plate model, or even a laminated plate structure could be considered. This would allow for the development of a more comprehensive train-track-bridge interaction system.~~ however, certain terrains necessitate the construction of large-span continuous girder bridges. The proposed model faces challenges in simulating such large-span bridges. As the span increases, the mechanical model becomes closer to a beam rather a plate. However, traditional beam models are also inadequate for simulating this bridge type effectively. We recommend employing a co-simulation approach, wherein programming software like MATLAB is utilized to simulate the structure above the bridge, while commercial software such as ABAQUS, ANSYS, and SIMPACK are employed for a refined modeling of the bridge.

Acknowledgments

This work was funded by the National Natural Science Foundation of China (Grant No. 11972379), the Key R&D Program of Hunan Province (2020SK2060), and Hunan Science Fund for Distinguished Young Scholars (2021JJ10061).

Declaration of Competing Interest

The authors declare that they have no known competing financial interests or personal relationships that could have appeared to influence the work reported in this paper.

Data Availability Statement

The data that support the findings of this study are available from the corresponding author, upon reasonable request.

References

[1] H. Zhao, B. Wei, L. Jiang, P. Xiang, X. Zhang, H. Ma, S. Xu, L. Wang, H. Wu, X. Xie, A velocity-related running safety assessment index in seismic design for railway bridge, Mech Syst Signal Pr 198 (2023) 110305. `doi:10.1016/j.ymssp.2023.110305`.

[2] Y. Wang, P. Wang, H. Tang, X. Liu, J. Xu, J. Xiao, J. Wu, Assessment and prediction of high speed railway bridge long-term deformation based on track geometry inspection big data, Mech Syst Signal Pr 158 (2021) 107749. `doi:10.1016/j.ymssp.2021.107749`.

[3] H. Zhao, B. Wei, P. Guo, J. Tan, P. Xiang, L. Jiang, W. Fu, X. Liu, Random analysis of train-bridge coupled system under non-uniform ground motion, Adv Struct Eng (2023). `doi:10.1177/13694332231175230`.

[4] C. Koh, J. Ong, D. Chua, J. Feng, Moving element method for train-track dynamics, Int J Numer Meth Eng 56 (11) (2003) 1549–1567. doi:10.1002/nme.624.

[5] L. Xu, Z. Yu, Z. Shan, Numerical simulation for train-track-bridge dynamic interaction considering damage constitutive relation of concrete tracks, Arch Civ Mech Eng 21 (2021) 1–23. doi:10.1007/s43452-021-00266-8.

[6] P. Xiang, H. Ma, H. Zhao, L. Jiang, S. Xu, X. Liu, Safety analysis of train-track-bridge coupled braking system under earthquake, Structures 53 (2023) 1519–1529. doi:10.1016/j.istruc.2023.04.086.

[7] P. Xiang, P. Guo, W. Zhou, X. Liu, L. Jiang, Z. Yu, J. Yu, Three-dimensional stochastic train-bridge coupling dynamics under aftershocks, Int J Civ Eng (2023) 1–17doi:10.1007/s40999-023-00846-0.

[8] L.-L. Ke, J. Yang, S. Kitipornchai, Nonlinear free vibration of functionally graded carbon nanotube-reinforced composite beams, Compos Struct 92 (3) (2010) 676–683. doi:10.1016/j.compstruct.2009.09.024.

[9] S. Kitipornchai, D. Chen, J. Yang, Free vibration and elastic buckling of functionally graded porous beams reinforced by graphene platelets, Mater Design 116 (2017) 656–665. doi:10.1016/j.matdes.2016.12.061.

[10] D. Chen, J. Yang, S. Kitipornchai, Elastic buckling and static bending of shear deformable functionally graded porous beam, Compos Struct 133 (2015) 54–61. doi:10.1016/j.compstruct.2015.07.052.

[11] J. Yang, H. Wu, S. Kitipornchai, Buckling and postbuckling of functionally graded multilayer graphene platelet-reinforced composite beams, Compos Struct 161 (2017) 111–118. doi:10.1016/j.compstruct.2016.11.048.

[12] Z. Shao, X. Li, P. Xiang, A new computational scheme for structural static stochastic analysis based on karhunen–loève expansion and modified perturbation stochastic finite element method, Comput Mech 71 (5) (2023) 917–933. doi:10.1007/s00466-022-02259-7.

[13] Z.-P. Zeng, F.-S. Liu, P. Lou, Y.-G. Zhao, L.-M. Peng, Formulation of three-dimensional equations of motion for train–slab track–bridge interaction system and its application to random vibration analysis, Appl Math Model 40 (11-12) (2016) 5891–5929. doi:10.1016/j.apm.2016.01.020.

[14] W. Zhou, L. Zu, L. Jiang, J. Yu, Y. Zuo, K. Peng, Influence of damping on seismic-induced track geometric irregularity spectrum in high-speed railway track-bridge system, Soil Dyn Earthq Eng 167 (2023) 107792. doi:10.1016/j.soildyn.2023.107792.

[15] Y. Tang, Z. Zhu, Z. Ba, V. W. Lee, W. Gong, Running safety assessment of trains considering post-earthquake damage state of bridge–track system, Eng Struct 287 (2023) 116187. doi:10.1016/j.engstruct.2023.116187.

[16] X. Liu, P. Xiang, L. Jiang, Z. Lai, T. Zhou, Y. Chen, Stochastic analysis of train–bridge system using the karhunen–loéve expansion and the point estimate method, Int J Struct Stab Dy 20 (02) (2020) 2050025. doi:10.1142/S021945542050025X.

[17] L. Jiang, X. Liu, P. Xiang, W. Zhou, Train-bridge system dynamics analysis with uncertain parameters based on new point estimate method, Eng Struct 199 (2019) 109454. doi:10.1016/j.engstruct.2019.109454.

[18] X. Lu, C.-W. Kim, K.-C. Chang, Finite element analysis framework for dynamic vehicle-bridge interaction system based on abaqus, Int J Struct Stab Dy 20 (03) (2020) 2050034. doi:10.1142/S0219455420500340.

[19] Z. Zhai, S. Zhu, Y. Yang, J. Luo, C. Cai, Dynamics analysis of train-track-bridge coupled system considering spatial flexibility of high piers and system longitudinal vibrations, Vehicle Syst Dyn 61 (10) (2022) 2613–2637. doi:10.1080/00423114.2022.2124178.

[20] P. Xiang, W. Huang, L. Jiang, D. Lu, X. Liu, Q. Zhang, Investigations on the influence of prestressed concrete creep on train-track-bridge system, Constr Build Mater 293 (2021) 123504. doi:10.1016/j.conbuildmat.2021.123504.

[21] H. Li, T. Wang, G. Wu, Probabilistic safety analysis of coupled train-bridge system using deep learning based surrogate model, Struct Infrastruct E 19 (8) (2023) 1138–1157. doi:10.1080/15732479.2021.2010104.

[22] M. Song, S. Kitipornchai, J. Yang, Free and forced vibrations of functionally graded polymer composite plates reinforced with graphene nanoplatelets, Compos Struct 159 (2017) 579–588. doi:10.1016/j.compstruct.2016.09.070.

[23] J. Yang, H.-S. Shen, Vibration characteristics and transient response of shear-deformable functionally graded plates in thermal environments, J Sound Vib 255 (3) (2002) 579–602. doi:10.1006/jsvi.2001.4161.

[24] T. Belytschko, Y. Y. Lu, L. Gu, Element-free galerkin methods, Int J Numer Meth Eng 37 (2) (1994) 229–256. doi:10.1002/nme.1620370205.

[25] Y. Deng, X. He, L. Sun, S. Yi, Y. Dai, An improved interpolating complex variable element free galerkin method for the pattern transformation of hydrogel, Eng Anal Bound Elem 113 (2020) 99–109. doi:10.1016/j.enganabound.2019.12.004.

[26] A. Ferreira, G. Fasshauer, R. Batra, Natural frequencies of thick plates made of orthotropic, monoclinic, and hexagonal materials by a meshless method, J Sound Vib 319 (3-5) (2009) 984–992. doi:10.1016/j.jsv.2008.06.034.

[27] J.-T. Chen, M. Chang, K. Chen, S. Lin, The boundary collocation method with meshless concept for acoustic eigenanalysis of two-dimensional cavities using radial basis function, J Sound Vib 257 (4) (2002) 667–711. doi:10.1006/jsvi.2002.5038.

[28] P. Xiang, L. Zhang, K. Liew, A mesh-free computational framework for predicting vibration behaviors of microtubules in an elastic medium, Compos Struct 149 (2016) 41–53. doi:10.1016/j.compstruct.2016.03.063.

[29] P. Xiang, L. Zhang, K. Liew, A third-order cauchy-born rule for modeling of microtubules based on the element-free framework, Compos Struct 161 (2017) 215–226. doi:10.1016/j.compstruct.2016.10.110.

[30] P. Xiang, K. M. Liew, Dynamic behaviors of long and curved microtubules based on an atomistic-continuum model, Comput Method Appl M 223 (2012) 123–132. doi:10.1016/j.cma.2012.02.023.

[31] R. A. Gingold, J. J. Monaghan, Smoothed particle hydrodynamics: theory and application to non-spherical stars, Mon Not R Astron Soc 181 (3) (1977) 375–389. doi:10.1093/mnras/181.3.375.

[32] J. J. Monaghan, Smoothed particle hydrodynamics, Annu Rev Astron Astr 30 (1) (1992) 543–574. doi:10.1146/annurev.aa.30.090192.002551.

[33] W. K. Liu, S. Jun, Y. F. Zhang, Reproducing kernel particle methods, Int J Numer Meth Fl 20 (8-9) (1995) 1081–1106. doi:10.1002/fld.1650200824.

[34] P. Xiang, Q. Xia, L. Jiang, L. Peng, J. Yan, X. Liu, Free vibration analysis of fg-cntrc conical shell panels using the kernel particle ritz element-free method, Compos Struct 255 (2021) 112987. doi:10.1016/j.compstruct.2020.112987.

[35] N. Perrone, R. Kao, A general finite difference method for arbitrary meshes, Comput Struct 5 (1) (1975) 45–57. doi:10.1016/0045-7949(75)90018-8.

[36] T. Liszka, J. Orkisz, The finite difference method at arbitrary irregular grids and its application in applied mechanics, Comput Struct 11 (1-2) (1980) 83–95. doi:10.1016/0045-7949(80)90149-2.

[37] G.-R. Liu, Y. Gu, A point interpolation method for two-dimensional solids, Int J Numer Meth Eng 50 (4) (2001) 937–951. doi:10.1002/1097-0207(20010210)50:4<937::AID-NME62>3.0.CO;2-X.

[38] J. Wang, G. Liu, A point interpolation meshless method based on radial basis functions, Int J Numer Meth Eng 54 (11) (2002) 1623–1648. doi:10.1002/nme.489.

[39] Q. Xia, P. Xiang, L. Jiang, J. Yan, L. Peng, Bending and free vibration and analysis of laminated plates on winkler foundations based on meshless layerwise theory, Mech Adv Mater Struc 29 (27) (2021) 6168–6187. doi:10.1080/15376494.2021.1972497.

[40] Z. Liu, G. Wei, Z. Wang, Numerical solution of functionally graded materials based on radial basis reproducing kernel particle method, Eng Anal Bound Elem 111 (2020) 32–43. doi:10.1016/j.enganabound.2019.09.023.

[41] Z. Liu, H. Gao, G. Wei, Z. Wang, The meshfree analysis of elasticity problem utilizing radial basis reproducing kernel particle method, Results Phys 17 (2020) 103037. doi:10.1016/j.rinp.2020.103037.

[42] S. Qin, G. Wei, B. Tang, The meshless analysis of elastic dynamic problem based on radial basis reproducing kernel particle method, Soil Dyn Earthq Eng 139 (2020) 106340. doi:10.1016/j.soildyn.2020.106340.

[43] T. Zhang, G. Wei, J. Ma, H. Gao, Radial basis reproducing kernel particle method for piezoelectric materials, Eng Anal Bound Elem 92 (2018) 171–179. doi:10.1016/j.enganabound.2017.10.020.

[44] J. Belinha, A. Araújo, A. Ferreira, L. Dinis, R. N. Jorge, The analysis of laminated plates using distinct advanced discretization meshless techniques, Comput Struct 143 (2016) 165–179. doi:10.1016/j.compstruct.2016.02.021.

[45] D. Rodrigues, J. Belinha, L. Dinis, R. N. Jorge, The bending behaviour of antisymmetric cross-ply laminates using high-order shear deformation theories and a radial point interpolation method, in: Structures, Vol. 32, 2021, pp. 1589–1603. doi:10.1016/j.istruc.2021.03.048.

[46] O. Askour, S. Mesmoudi, Y. Hilali, M. Rammane, O. Bourihane, An improved fsdt with an efficient mesh-free approach for nonlinear static analysis of fg-goprc beams, in: Structures, Vol. 58, 2023, p. 105575. doi:10.1016/j.istruc.2023.105575.

[47] X. Liu, L. Jiang, Z. Lai, P. Xiang, Y. Chen, Sensitivity and dynamic analysis of train-bridge coupled system with multiple random factors, Eng Struct 221 (2020) 111083. doi:10.1016/j.engstruct.2020.111083.

[48] P. Xiang, M. Wei, M. Sun, Q. Li, L. Jiang, X. Liu, J. Ren, Creep effect on the dynamic response of train-track-continuous bridge system, Int J Struct Stab Dy 21 (10) (2021) 2150139. doi:10.1142/S021945542150139X.

[49] P. Lou, Q. Zeng, Formulation of equations of motion of finite element form for vehicle–track–bridge interaction system with two types of vehicle model, Int J Numer Meth Eng 62 (3) (2005) 435–474. `doi:10.1002/nme.1207`.

[50] L. Xiang, J. Lizhong, X. Ping, et al., Analysis of train-bridge vertical random vibration based on a new point estimate method, Journal of Vibration and Shock 39 (6) (2020) 15–21. `doi:10.13465/j.cnki.jvs.2020.06.003`.

[51] J. Yang, H.-S. Shen, Dynamic response of initially stressed functionally graded rectangular thin plates, Compos Struct 54 (4) (2001) 497–508. `doi:10.1016/S0263-8223(01)00122-2`.

[52] C. Lü, C. W. Lim, W. Chen, Exact solutions for free vibrations of functionally graded thick plates on elastic foundations, Mech Adv Mater Struc 16 (8) (2009) 576–584. `doi:10.1080/15376490903138888`.

[53] C. W. Lim, C. Lü, Y. Xiang, W. Yao, On new symplectic elasticity approach for exact free vibration solutions of rectangular kirchhoff plates, Int J Eng Sci 47 (1) (2009) 131–140. `doi:j.ijengsci.2008.08.003`.

[54] C. Lim, Z. Li, Y. Xiang, G. Wei, C. M. Wang, On the missing modes when using the exact frequency relationship between kirchhoff and mindlin plates, Adv Vib Eng 4 (3) (2005) 221–248.

[55] M. Rafiee, X. He, K. Liew, Non-linear dynamic stability of piezoelectric functionally graded carbon nanotube-reinforced composite plates with initial geometric imperfection, Int J Nonlin Mech 59 (2014) 37–51. `doi:10.1016/j.ijnonlinmec.2013.10.011`.

[56] M. Rafiee, X. He, S. Mareishi, K. Liew, Modeling and stress analysis of smart cnts/fiber/polymer multiscale composite plates, Int J Appl Mech 6 (03) (2014) 1450025. `doi:10.1142/S1758825114500252`.

[57] K. Liew, X. He, T. Ng, S. Sivashanker, Active control of fgm plates subjected to a temperature gradient: modelling via finite element method based on fsdt, Int J Numer Meth Eng 52 (11) (2001) 1253–1271. `doi:10.1002/nme.252`.

[58] P. Zhu, Z. Lei, K. M. Liew, Static and free vibration analyses of carbon nanotube-reinforced composite plates using finite element method with first order shear deformation plate theory, Compos Struct 94 (4) (2012) 1450–1460. doi:10.1016/j.compstruct.2011.11.010.

[59] X. Li, Y. Zhu, Z. Jin, Nonstationary random vibration performance of train-bridge coupling system with vertical track irregularity, Shock Vib 2016 (2016) 1450895. doi:10.1155/2016/1450895.

[60] H. Xia, N. Zhang, W. Guo, H. Xia, N. Zhang, W. Guo, Dynamic analysis of train-bridge coupling system, Dynamic Interaction of Train-Bridge Systems in High-Speed Railways: Theory and Applications (2018) 227–289doi:10.1007/978-3-662-54871-4_5.

[61] Z.-w. Yu, J.-f. Mao, F.-q. Guo, W. Guo, Non-stationary random vibration analysis of a 3d train–bridge system using the probability density evolution method, J Sound Vib 366 (2016) 173–189. doi:10.1016/j.jsv.2015.12.002.

[62] L. Xu, W. Zhai, A three-dimensional model for train-track-bridge dynamic interactions with hypothesis of wheel-rail rigid contact, Mech Syst Signal Pr 132 (2019) 471–489. doi:10.1016/j.ymssp.2019.04.025.

[63] H.-H. Phan-Dao, C. H. Thai, J. Lee, H. Nguyen-Xuan, Analysis of laminated composite and sandwich plate structures using generalized layerwise hsdt and improved meshfree radial point interpolation method, Aerosp Sci Technol 58 (2016) 641–660. doi:10.1016/j.ast.2016.09.017.

[64] H. Zhao, B. Wei, L. Jiang, P. Xiang, Seismic running safety assessment for stochastic vibration of train–bridge coupled system, Arch Civ Mech Eng 22 (4) (2022) 180. doi:10.1007/s43452-022-00451-3.

[65] P. Zhang, H. Zhao, Z. Shao, L. Jiang, H. Hu, Y. Zeng, P. Xiang, A rapid analysis framework for seismic response prediction and running safety assessment of train-bridge coupled systems, Soil Dyn Earthq Eng 177 (2024) 108386. doi:10.1016/j.soildyn.2023.108386.

[66] H. Zhao, B. Wei, P. Zhang, P. Guo, Z. Shao, S. Xu, L. Jiang, H. Hu, Y. Zeng, P. Xiang, Safety analysis of high-speed trains on bridges under

earthquakes using a lstm-rnn-based surrogate model, Comput Struct 294 (2024) 107274. doi:10.1016/j.compstruc.2024.107274.

[67] P. Xiang, P. Zhang, H. Zhao, Z. Shao, L. Jiang, Seismic response prediction of a train-bridge coupled system based on a lstm neural network, Mech Based Des Struc (2023) 1–23doi:10.1080/15397734.2023.2260469.

[68] H. Xiang, J. Yang, Free and forced vibration of a laminated fgm timoshenko beam of variable thickness under heat conduction, Compos Part B-Eng 39 (2) (2008) 292–303. doi:10.1016/j.compositesb.2007.01.005.

A meshless computational framework for a modified dynamic system of vehicle coupled with plate structure

Zhanjun Shao[a,b], Han Zhao[a,b], Peng Zhang[a,b], Xiaonan Xie[a,b], A. S. Ademiloye[c], Ping Xiang[a,b,*]

[a] *School of Civil Engineering, Central South University, Changsha, 410075, Hunan, China*
[b] *National Engineering Research Center of High-speed Railway Construction Technology, Changsha, 410018, Hunan, China*
[c] *Data and AI (ZI), Zienkiewicz Institute for Modelling, College of Engineering, Swansea University, Swansea, W Glam, Wales*

Abstract

In previous simulations of train-bridge interaction systems (TBIS), the supporting system for the train are commonly treated as beam structures, leading to less accurate results, particularly for small-span cases. To address this limitation, a modified vertical TBIS is proposed. In the presented TBIS, the supporting system is considered as a Reissner-Mindlin plate, and the displacement field is described by first-order shear deformation theory (FSDT). To establish the model, radial point interpolation method (RPIM), a meshless method, is employed. Finally, a coupled dynamic equation is established to calculate various responses of the system. Several numerical examples are presented to illustrate the disparities between the system based on plate model and traditional beam model. The results indicate that the beam model yields higher estimates of the mid-span vertical displacement of the bridge, while the peak of the mid-span vertical acceleration is smaller compared to the plate model; additionally, it is observed that the carbody is primarily influenced by rail irregularities. Consequently, the proposed plate model offers distinct advantages over the beam model in providing comprehensive structural response information, thereby offering novel insights into bridge design and analysis. Additionally, this marks the inaugural application of the

---

[*] Corresponding author.
Email address: `pxiang2-c@my.cityu.edu.hk` (Ping Xiang)

meshless method in the field of TBIS, which further extends the application scope of meshless methods.

Keywords: Train-bridge interaction system, Meshless method, Computational plate-shell mechanics, High-speed railway, Rail irregularity

---

1. Introduction

By the end of 2022, the total length of Chinese high-speed railway has exceeded 42,000 km. In this extensive network, a significant portion of the railway lines is composed of bridges [1, 2]. The construction of high-speed railways frequently faces various challenges related to terrain and environmental conditions. Therefore, it is necessary to conduct demonstrations to assist in the design process. Numerical simulation is highly recommended in this regard, primarily due to the substantial costs associated with conducting physical tests. In recent decades, researchers have created a variety of TBIS utilizing various numerical methods. These TBIS can be broadly classified into three distinct categories: programming-based, finite element software-based, and co-simulation-based.

The first category of TBIS relies entirely on programming. It involves processes such as utilizing MATLAB to simplify each component of the TBIS and establishing a mechanical model for each part [3–5]. Subsequently, these models are integrated using multi-body dynamics principles to formulate the dynamic equations governing the TBIS. For example, in this approach, the trains are simplified to mass points, while the tracks, piers, bridges, and other components are represented as simplified beam structures [6–11]. These components are then interconnected, taking into account the wheel-rail interaction and multi-body dynamics. Beam structures are widely used in buildings, especially frame structures [12]. However, for many complex structures in TBIS, the beam structures do not represent thier mechanical performance well. For instance, it is not reasonable to approximate track slabs [13–15] and box girder bridges [16, 17] solely as beam structures, given their intricate nature. Hence, a crucial research focus lies in determining a reasonable and accurate approach for modeling track slabs and bridges within the first category of TBIS.

The second category of TBIS primarily relies on commercial software for modeling purposes. The components within the system are modeled using software such as ABAQUS or ANSYS or some other software, and subsequent assembly and calculations are performed within the software framework [18]. This approach takes advantage of well-established commercial software with robust modeling capabilities. In this type of TBIS, components like rails, track slabs, and bridges receive more intricate modeling, but the simulation of inter-component relationships, especially the wheel-rail relationship, is a complex task.

The third category of TBIS represents a combination of the first two. In this hybrid TBIS, components located above the bridge are typically modeled using MATLAB, while commercial software is uesd to tackle the intricate modeling of complex structures, such as bridges and piers [19]. This approach capitalizes on the strengths of the first two TBIS and often yields heightened modeling accuracy. However, it is worth noting that this approach comes with a relatively high threshold due to the concurrent use of multiple modeling platforms.

The first category of TBIS is the most commonly employed and offers extensive utility in conducting various analyses. These applications involve the investigation of factors such as impact of prestressed concrete bridge creep [20], as well as integrating it with neural networks to formulate predictions regarding train running safety [21]. Meanwhile, the first category of TBIS is entirely based on the programming platform, offering researchers significant flexibility. In contrast, the second category of TBIS faces limitations imposed by commercial software and the challenges of secondary development, and has some difficulties in introducing advanced mechanical theories. For academic research, the first category of TBIS proves more advantageous. Furthermore, the first category of TBIS is implemented on a single platform, eliminating the need for multi-platform data exchange as required in the third category of TBIS. Moreover, in some cases, the third category of TBIS requires the introduction of supercomputing platform support, which is costly. This reduction in development cost and complexity further supports its academic appeal. Therefore, the research object of this paper is the first category of TBIS. To enhance the accuracy of programming-based TBIS, the primary research focus is directed towards optimizing structural modeling. We drew inspiration from the enhancements achieved by researchers in refining the track slab model and embarked on an effort to enhance the bridge model. Many high-speed railway bridges are designed with simply supported box girder bridges, with dimensions more closely resembling plate structures than beam structures. Furthermore, these bridges exhibit intricate mechanical responses that cannot be replicated using beam elements alone. Consequently, in the pursuit of enhanced accuracy and the ensurance of reliability in train running safety analysis, this paper tries to substitute the beam model with a plate model, coupled with the train, in the development of TBIS.

Finite element method (FEM) [22] and its extensions, implemented in various commercial software, are the predominant approaches for modeling of plate structures [23]. However, FEM requires the construction of complex mesh to discretize and solve partial differential equations. Consequently, researchers must focus on mesh quality to achieve accurate results, and the cost of generating high-quality mesh is much higher than the computational cost [24]. While meshless methods has no mesh limitation, they do not require an explicitly defined connectivity between nodes for the definition of the shape functions. Moreover, the approximation and interpolation functions of meshless methods are usually high-order continuous, without the distortion effect of the mesh, ensuring the global smoothness of stress and making it easy to handle large deformation problems [25], dynamic analysis [26], acoustic analysis [27], etc. In addition to the classical methods like moving least squares method [28–30], smoothed particle hydrodynamics method [31, 32], reproducing kernel particle method [33, 34], general finite difference method [35, 36], point interpolation method [37], etc., several new meshless methods have emerged, building upon these classical approaches. Radial basis functions (RBFs) have played a crucial role in the advancement of meshless methods. RBFs can be either compactly supported or globally gained, and their introduction has enhanced the performance of many classical methods. For example, in order to prevent the occurrence of matrix singularity issues in point interpolation method, RBFs have been introduced to guarantee the compatibility of the approximate function, which is called radial point interpolation method [38, 39]; Wei [40–43] introduced RBFs into reproducing kernel particle method and successfully used this method to analyze the mechanical behavior of a variety of structures and materials. These examples illustrate the advantages of meshless methods and demonstrate their feasibility for modeling bridge plates.

In this paper, we propose a computational framework based on RPIM and FSDT. The framework improves the bridge model and helps to improve the accuracy of the TBIS. Furthermore, the introduction of this framework opens up opportunities for creating more intricate bridge models utilizing multiple plates, and multiple plate structures hopefully yield more accurate simulation results. Meanwhile, the utilization of FSDT in conjunction with RPIM [44–46], as employed in this paper, enjoys broad recognition within the realm of computational mechanics for plates and shells, but it is the first attempt in the field of TBIS. The work path of this paper is shown as Fig. 1.

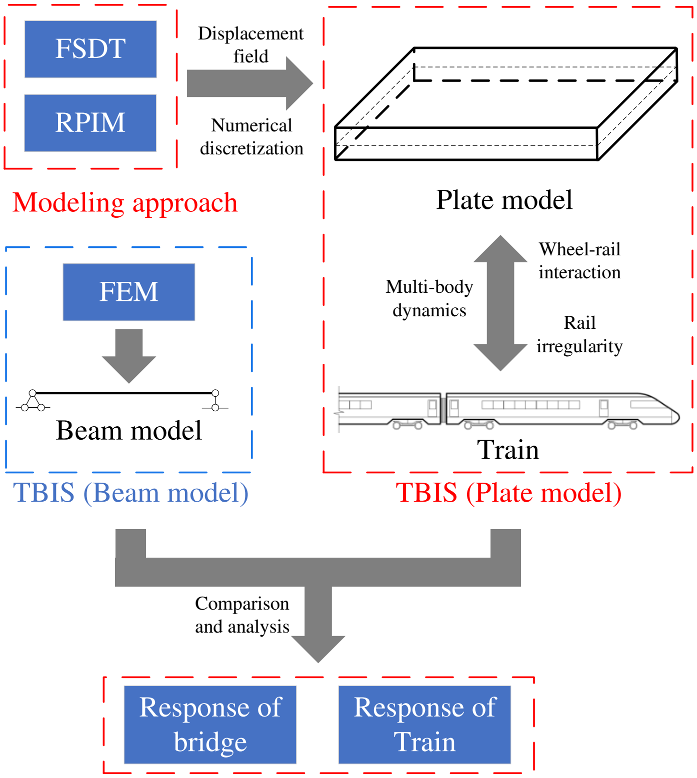

Figure 1: The work path of this paper.

2. Vertical TBIS

Vertical TBIS primarily concentrates on the vertical structural response. Despite its reduced degrees of freedom, this system proves conducive to validating novel approaches, including stochastic analyses[47]. It is also suitable for scrutinizing factors significantly affecting vertical structural response, such as structural concrete creep [48]. In this paper, we opt to employ vertical TBIS for the validation of our proposed computational framework, with the intention of later extending its applicability to spatial TBIS in future research. Moreover, both vertical and spatial TBIS can be established by the principle of total potential energy with stationary value in elastic system dynamics proposed by Zeng [49], so only derivation results are given in this paper. In addition, the modified vertical TBIS proposed in this paper is shown in Fig. 2, and the variables in the figure are explained by Tab. 1.

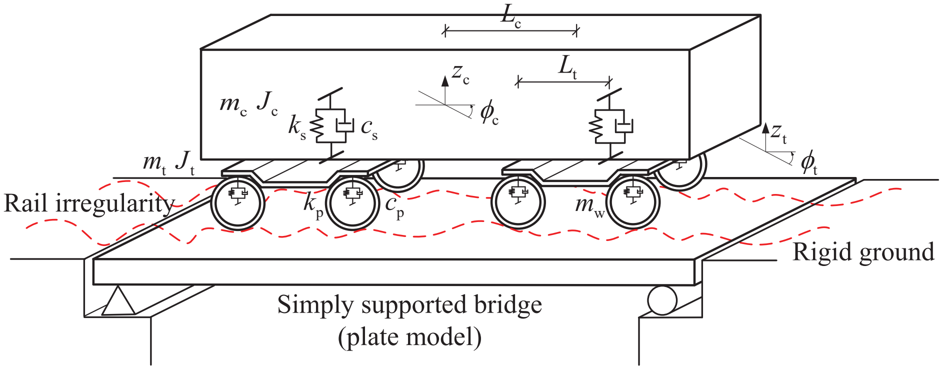

Figure 2: The proposed vertical train-bridge interaction system.

Based on the vertical TBIS presented in Ref. [16], the wheel and rail exhibit a close-fitting relationship expressed by the following equation:

$$z_{\mathrm{w}i} = z_{\mathrm{b}i} + z_{\mathrm{r}i} \tag{1}$$

where z represents the vertical displacement, and the subscript w denotes the wheel, b denotes the bridge, r denotes the vertical rail irregularity, and i denotes the $i-$th wheel. Eq. (1) indicates that the vertical displacement $z_{\mathrm{w}i}$ of the $i-$th wheel is the sum of the vertical displacement $z_{\mathrm{b}i}$ of the bridge and the vertical rail irregularity $z_{\mathrm{r}i}$ at its location.

Due to the relationship between the wheel and rail, a vehicle contains 6 DOFs, i.e.

$$\boldsymbol{U}_{\mathrm{v}} = \begin{bmatrix} z_{\mathrm{c}} & \phi_{\mathrm{c}} & z_{\mathrm{t1}} & \phi_{\mathrm{t1}} & z_{\mathrm{t2}} & \phi_{\mathrm{t2}} \end{bmatrix}, \tag{2}$$

The mass matrix corresponding to the vector of DOF is denoted as follows.

$$\boldsymbol{M}_{\mathrm{v}} = \begin{bmatrix} m_{\mathrm{c}} & 0 & 0 & 0 & 0 & 0 \\ 0 & J_{\mathrm{c}} & 0 & 0 & 0 & 0 \\ 0 & 0 & m_{\mathrm{t1}} & 0 & 0 & 0 \\ 0 & 0 & 0 & J_{\mathrm{t1}} & 0 & 0 \\ 0 & 0 & 0 & 0 & m_{\mathrm{t2}} & 0 \\ 0 & 0 & 0 & 0 & 0 & J_{\mathrm{t2}} \end{bmatrix}, \tag{3}$$

Table 1: Explanation of variables in Fig. 2.

Variable	Explanation
z_c	Vertical displacement of carbody
ϕ_c	Rotational displacement of carbody
m_c	Mass of carbody
J_c	Mass moment of inertia of carbody
z_t	Vertical displacement of bogie
ϕ_t	Rotational displacement of bogie
m_t	Mass of bogie
J_t	Mass moment of inertia of bogie
m_w	Mass of wheel
k_s	Spring stiffness of the second suspension
c_s	Damping coefficient of the second suspension
k_p	Spring stiffness of the primary suspension
c_p	Damping coefficient of the primary suspension
L_c	Half of longitudinal distance between the centers of front and rear bogies
L_t	Half of bogie axle base

Meanwhile, in Fig. 2, the suspensions are modeled as springs and damping elements. Thus, the stiffness matrix [50] of the car can be written as

$$\boldsymbol{K}_\mathrm{v} = \begin{bmatrix} 2k_\mathrm{s} & 0 & -k_\mathrm{s} & 0 & -k_\mathrm{s} & 0 \\ 0 & 2k_\mathrm{s}L_\mathrm{c}^2 & k_\mathrm{s}L_\mathrm{c} & 0 & -k_\mathrm{s}L_\mathrm{c} & 0 \\ -k_\mathrm{s} & k_\mathrm{s}L_\mathrm{c} & 2k_\mathrm{p}+k_\mathrm{s} & 0 & 0 & 0 \\ 0 & 0 & 0 & 2k_\mathrm{p}L_\mathrm{t}^2 & 0 & 0 \\ -k_\mathrm{s} & -k_\mathrm{s}L_\mathrm{c} & 0 & 0 & 2k_\mathrm{p}+k_\mathrm{s} & 0 \\ 0 & 0 & 0 & 0 & 0 & 2k_\mathrm{p}L_\mathrm{t}^2 \end{bmatrix}, \tag{4}$$

The damping matrix $\boldsymbol{C}_\mathrm{v}$ has the same form as $\boldsymbol{K}_\mathrm{v}$, except that k_s and k_p are replaced by c_s and c_p.

A train often consists of multiple vehicles. The stiffness matrix $\boldsymbol{K}_\mathrm{vv}$ of the train can be written as

$$\boldsymbol{K}_\mathrm{vv} = \mathrm{diag}\left[\boldsymbol{K}_\mathrm{v1} \quad \boldsymbol{K}_\mathrm{v2} \quad \cdots \quad \boldsymbol{K}_{\mathrm{v}N}\right] \tag{5}$$

where N represents the train contains N vehicles; $\boldsymbol{K}_\mathrm{v1}$ and $\boldsymbol{K}_{\mathrm{v}N}$ are normally motor cars, and $\boldsymbol{K}_\mathrm{v2} \sim \boldsymbol{K}_{\mathrm{v}N-1}$ are trailer cars. Similarly, $\boldsymbol{M}_\mathrm{vv}$ and $\boldsymbol{C}_\mathrm{vv}$ can be obtained in the same form.

The TBIS in this study consists of two components, train and bridge.

Therefore, the dynamic equation of the vertical TBIS can be written as

$$\begin{bmatrix} \boldsymbol{M}_{\text{vv}} & \\ & \boldsymbol{M}_{\text{bb}} \end{bmatrix} \begin{Bmatrix} \ddot{\boldsymbol{u}}_{\text{vv}} \\ \ddot{\boldsymbol{u}}_{\text{bb}} \end{Bmatrix} + \begin{bmatrix} \boldsymbol{C}_{\text{vv}} & \boldsymbol{C}_{\text{vb}} \\ \boldsymbol{C}_{\text{bv}} & \boldsymbol{C}_{\text{bb}} \end{bmatrix} \begin{Bmatrix} \dot{\boldsymbol{u}}_{\text{vv}} \\ \dot{\boldsymbol{u}}_{\text{bb}} \end{Bmatrix} + \begin{bmatrix} \boldsymbol{K}_{\text{vv}} & \boldsymbol{K}_{\text{vb}} \\ \boldsymbol{K}_{\text{bv}} & \boldsymbol{K}_{\text{bb}} \end{bmatrix} \begin{Bmatrix} \boldsymbol{u}_{\text{vv}} \\ \boldsymbol{u}_{\text{bb}} \end{Bmatrix} = \begin{Bmatrix} \boldsymbol{F}_{\text{vv}} \\ \boldsymbol{F}_{\text{bb}} \end{Bmatrix}, \tag{6}$$

where the matrices associated with the bridge, such as $\boldsymbol{M}_{\text{bb}}$, $\boldsymbol{K}_{\text{bb}}$, $\boldsymbol{K}_{\text{vb}}$, etc., are obtained after determining the mechanical model of the bridge.

3. Plate mechanics

In computational plate mechanics, different theories exist to describe the mechanical behavior of thin [51], medium-thick, or thcik plate [52] structures. These theories include Kirchhoff-Love theory [53, 54], Reissner-Mindlin theory (FSDT [55–57]), and several higher-order shear deformation theories. In this study, FSDT is employed to describe the displacement field of the plate.

The employment of FSDT is based on the following primary considerations:

(1) In comparison to Kirchhoff-Love theory, the displacement field in Reissner-Mindlin theory is independently interpolated at displacement and rotating angle, respectively, which holds significant importance. This arises from the fact that, following the discretization by the meshless method, the nodal displacement vectors in the Kirchhoff-Love theory do not incorporate the rotating angle (as shown in Eq.(7)), rendering it unsuitable for assembling box girder structures with multiple plates in subsequent studies.

$$\boldsymbol{u}_{\text{K}} = \begin{cases} u \\ v \\ w \end{cases} \text{(Kirchhoff-Love)}\,, \boldsymbol{u}_{\text{R}} = \begin{cases} u \\ v \\ w \\ \theta_x \\ \theta_y \end{cases} \text{(Reissner-Mindlin)} \tag{7}$$

(2) The higher-order shear theories have a larger number of degrees of freedom compared to FSDT, leading to an increase in computational requirements. Given that the thickness of the bridge plate is thick, the applications of higher-order shear theories do not yield substantial benefits in terms of model accuracy; instead, it diminishes computational efficiency.

To summarize the belongings, the employment of FSDT is crucial in this study and its follow-up.

3.1. First-order shear deformation theory

Establishing the plate model as shown in Fig. 3, the displacement field based on FSDT can be defined as

$$u = u_0 + z\theta_x \tag{8}$$

$$v = v_0 + z\theta_y \tag{9}$$

$$w = w_0 \tag{10}$$

where u, v, and w represent the displacements in the x, y, and z directions, respectively; the subscript 0 denotes the mid-plane of the plate; θ_x and θ_y represent the rotations of a transverse normal about positive y and negative x axes. Therefore, u_0, v_0, w_0, θ_x, and θ_y are the basic unknowns of the displacement field.

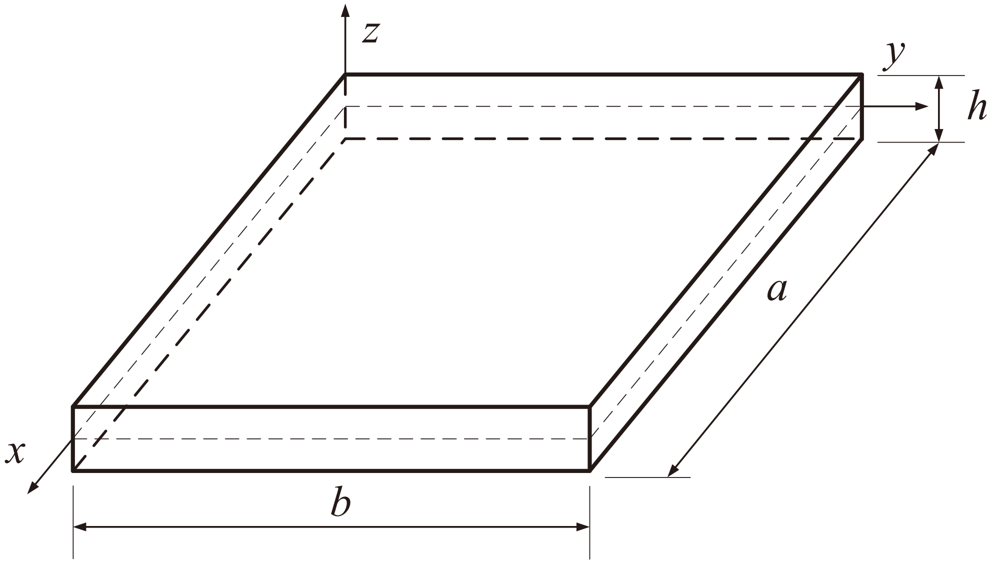

Figure 3: The geometry of the plate model.

The geometric equations of the plate can be listed as

$$\begin{Bmatrix} \varepsilon_x \\ \varepsilon_y \\ \gamma_{xy} \end{Bmatrix} = \boldsymbol{\varepsilon}_0 + z\boldsymbol{\kappa}, \quad \begin{Bmatrix} \gamma_{yz} \\ \gamma_{xz} \end{Bmatrix} = \boldsymbol{\gamma}_0, \tag{11}$$

$$\boldsymbol{\varepsilon}_0 = \begin{Bmatrix} \frac{\partial u_0}{\partial x} \\ \frac{\partial v_0}{\partial y} \\ \frac{\partial u_0}{\partial y} + \frac{\partial v_0}{\partial x} \end{Bmatrix}, \quad \boldsymbol{\kappa} = \begin{Bmatrix} \frac{\partial \theta_x}{\partial x} \\ \frac{\partial \theta_y}{\partial y} \\ \frac{\partial \theta_x}{\partial y} + \frac{\partial \theta_y}{\partial x} \end{Bmatrix}, \quad \boldsymbol{\gamma}_0 = \begin{Bmatrix} \theta_y + \frac{\partial w_0}{\partial y} \\ \theta_x + \frac{\partial w_0}{\partial x} \end{Bmatrix}. \tag{12}$$

Meanwhile, the constitutive equations can be written as

$$\begin{Bmatrix} \sigma_x \\ \sigma_y \\ \sigma_{xy} \\ \sigma_{yz} \\ \sigma_{xz} \end{Bmatrix} = \begin{bmatrix} Q_{11} & Q_{12} & 0 & 0 & 0 \\ Q_{12} & Q_{11} & 0 & 0 & 0 \\ 0 & 0 & Q_{44} & 0 & 0 \\ 0 & 0 & 0 & Q_{44} & 0 \\ 0 & 0 & 0 & 0 & Q_{44} \end{bmatrix} \times \begin{Bmatrix} \varepsilon_x \\ \varepsilon_y \\ \gamma_{xy} \\ \gamma_{yz} \\ \gamma_{xz} \end{Bmatrix}, \tag{13}$$

assuming that the bridge plate behaves isotropically, we have

$$Q_{11} = \frac{E}{1-v^2}, \quad Q_{12} = \frac{vE}{1-v^2}, \quad Q_{44} = \frac{E}{2(1+v)}, \tag{14}$$

where E is Young's modulus and v is Poisson's ratio.

According to Eqs. 12 and 13, the relationship between in-plane force $\boldsymbol{P}$ and strain $\boldsymbol{\epsilon}$ can be obtained as

$$\boldsymbol{P} = \boldsymbol{S}\boldsymbol{\epsilon} \tag{15}$$

where $\boldsymbol{S}$ can be given by

$$\boldsymbol{S} = \begin{bmatrix} \boldsymbol{A} & \bar{\boldsymbol{B}} & \mathbf{0} \\ \bar{\boldsymbol{B}} & \boldsymbol{D} & \mathbf{0} \\ \mathbf{0} & \mathbf{0} & \boldsymbol{A}_{\mathrm{s}} \end{bmatrix}, \tag{16}$$

with

$$\begin{gathered} \left\{ A_{ij} \quad B_{ij} \quad D_{ij} \right\} = \int_{h/2}^{-h/2} \left(1,\, z,\, z^2\right) Q_{ij} \mathrm{d}z \\ A_{ij}^{\mathrm{s}} = K \int_{h/2}^{-h/2} Q_{ij} \mathrm{d}z \end{gathered} \tag{17}$$

and the transverse shear correction coefficient $K = 5/6$.

3.2. Radial point interpolation method

Compared with the meshless methods where penalty functions are used to impose boundary conditions, the shape function of radial point interpolation method [38] has the property of Kronecker δ function, which can easily impose the essential boundary. At the same time, the coupled polynomial and radial basis point interpolation method constructs a shape function that preserves the linear regenerative characteristics of the polynomial basis point interpolation method. It also possesses the compatibility advantage of the radial basis point interpolation method, allowing for automatic adaptation to an arbitrary number of supporting nodes, typically resulting in high approximation accuracy. Therefore, this study employs RPIM as a numerical discretization tool.

The approximation displacement fiedl function $u^{\mathrm{h}}(\boldsymbol{x})$ of RPIM can be written as

$$u\left(\boldsymbol{x}\right) \approx u^{\mathrm{h}}\left(\boldsymbol{x}\right) = \sum_{t=1}^{m} p_t\left(\boldsymbol{x}\right) a_t + \sum_{s=1}^{NP} R_s\left(\boldsymbol{x}\right) b_s = \boldsymbol{p}^{\mathrm{T}}\left(\boldsymbol{x}\right) \boldsymbol{a} + \boldsymbol{R}^{\mathrm{T}}\left(\boldsymbol{x}\right) \boldsymbol{b}, \quad (18)$$

where $\boldsymbol{p}(\boldsymbol{x})$ is the polynomial basis functions and $\boldsymbol{R}(\boldsymbol{x})$ is the radial basis functions. For the plate structures, the complete quadratic basis functions are

$$\boldsymbol{p}\left(\boldsymbol{x}\right) = \begin{bmatrix} 1 & x & y & x^2 & xy & y^2 \end{bmatrix}^{\mathrm{T}} \quad (19)$$

And the radial basis functions $\boldsymbol{R}(\boldsymbol{x})$ are defined as

$$\boldsymbol{R}\left(\boldsymbol{x}\right) = \begin{bmatrix} R_1\left(\boldsymbol{x}\right), & R_2\left(\boldsymbol{x}\right), & \cdots, & R_{NP}\left(\boldsymbol{x}\right) \end{bmatrix}^{\mathrm{T}} \quad (20)$$

where the number of the terms NP denotes the number of the supporting node contained in the supporting domain $\mathit{\Omega}_{\mathrm{S}}$ with the coordinate $\boldsymbol{x}$ as the center. The supporting domain encompasses the supporting nodes, as illustrated in Fig. 4, with all the black supporting nodes contained within the blue box. It then interpolates to generate information about the computational node $\boldsymbol{x}$ through the shape function. The extent of the supporting domain is determined by the scale influence factor χ, and achieving a reasonable range for the supporting domain is crucial to produce results with relatively high accuracy.

The value of the radial basis function depends only on the distance function r, and in this paper, the multi-quadratic radial basis function is employed, i.e.

$$R_s\left(\boldsymbol{x}\right) = \left[r^2 + \left(\alpha h\right)^2\right]^{\beta}, \quad (21)$$

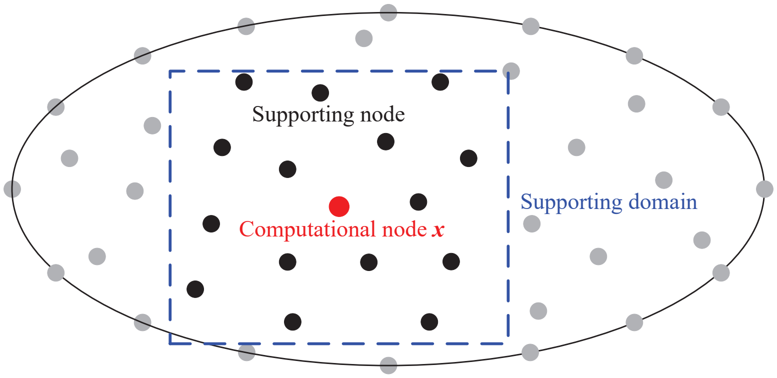

Figure 4: Supporting domain and supporting nodes of the meshless method.

where $r = \sqrt{(x - x_s)^2 + (y - y_s)^2}$; h is the average node spacing; α and β are the shape coefficients, and they are set to 1 and 1.03 respectively according to Ref. [39].

On the supporting domain $\varOmega_{\mathrm{S}}$ of the computing node $\boldsymbol{x}$, the functional J_1 and J_2 is constructed based on the set of the scattered supporting nodes $\{x_I\}_{I=1}^{NP} \left(\forall x_I \in \varOmega_{\mathrm{S}}\right)$.

$$J_1 = \sum_{I=1}^{NP} \left[\boldsymbol{P}_I^{\mathrm{T}}(\boldsymbol{x})\,\boldsymbol{a} + \boldsymbol{R}_I^{\mathrm{T}}(\boldsymbol{x})\,\boldsymbol{b} - \hat{u}_I\right], \tag{22}$$

$$J_2 = \sum_{I=1}^{NP} p_t(\boldsymbol{x}_I)\,b_I, \quad t = 1, 2, \cdots, 6. \tag{23}$$

Let $J_1 = 0$, $J_2 = 0$, Eq. (24) can be obtained.

$$\begin{bmatrix} \boldsymbol{A} & \boldsymbol{P} \\ \boldsymbol{P}^{\mathrm{T}} & \boldsymbol{0} \end{bmatrix} \begin{bmatrix} \boldsymbol{b} \\ \boldsymbol{a} \end{bmatrix} = \begin{bmatrix} \hat{\boldsymbol{u}} \\ \boldsymbol{0} \end{bmatrix}, \tag{24}$$

where $\boldsymbol{P}$ and $\boldsymbol{A}$ can be written as

$$\boldsymbol{P} = \begin{bmatrix} p_1(\boldsymbol{x}_1) & p_2(\boldsymbol{x}_1) & \cdots & p_6(\boldsymbol{x}_1) \\ p_1(\boldsymbol{x}_2) & p_2(\boldsymbol{x}_2) & \cdots & p_6(\boldsymbol{x}_2) \\ \vdots & \vdots & \ddots & \vdots \\ p_1(\boldsymbol{x}_{NP}) & p_2(\boldsymbol{x}_{NP}) & \cdots & p_6(\boldsymbol{x}_{NP}) \end{bmatrix} \tag{25}$$

$$\boldsymbol{A}=\begin{bmatrix} R_1(\boldsymbol{x}_1) & R_2(\boldsymbol{x}_1) & \cdots & R_{NP}(\boldsymbol{x}_1) \\ R_1(\boldsymbol{x}_2) & R_2(\boldsymbol{x}_2) & \cdots & R_{NP}(\boldsymbol{x}_2) \\ \vdots & \vdots & \ddots & \vdots \\ R_1(\boldsymbol{x}_{NP}) & R_2(\boldsymbol{x}_{NP}) & \cdots & R_{NP}(\boldsymbol{x}_{NP}) \end{bmatrix} \tag{26}$$

By solving Eq. (24), we have

$$\boldsymbol{a}=\underbrace{\left(\boldsymbol{P}^{\mathrm{T}}\boldsymbol{A}^{-1}\boldsymbol{P}\right)^{-1}\boldsymbol{P}^{\mathrm{T}}\boldsymbol{A}^{-1}}_{\boldsymbol{G}_{\mathrm{a}}}\hat{\boldsymbol{u}}=\boldsymbol{G}_{\mathrm{a}}\hat{\boldsymbol{u}}, \tag{27}$$

$$\boldsymbol{b}=\underbrace{\left[\boldsymbol{A}^{-1}-\boldsymbol{A}^{-1}\boldsymbol{P}\left(\boldsymbol{P}^{\mathrm{T}}\boldsymbol{A}^{-1}\boldsymbol{P}\right)^{-1}\boldsymbol{P}^{\mathrm{T}}\boldsymbol{A}^{-1}\right]}_{\boldsymbol{G}_{\mathrm{b}}}\hat{\boldsymbol{u}}=\boldsymbol{G}_{\mathrm{b}}\hat{\boldsymbol{u}}. \tag{28}$$

Therefore, for the computing node $\boldsymbol{x}$, its approximate displacement field function can be rewritten as

$$\begin{aligned} u^h(\boldsymbol{x}) &= \boldsymbol{p}^{\mathrm{T}}(\boldsymbol{x})\,\boldsymbol{a}+\boldsymbol{R}^{\mathrm{T}}(\boldsymbol{x})\,\boldsymbol{b}=\left[\boldsymbol{p}^{\mathrm{T}}(\boldsymbol{x})\,\boldsymbol{G}_{\mathrm{a}}+\boldsymbol{R}^{\mathrm{T}}(\boldsymbol{x})\,\boldsymbol{G}_{\mathrm{b}}\right]\hat{\boldsymbol{u}} \\ &= \sum_{I=1}^{NP}\Phi_I(\boldsymbol{x})\,\hat{u}_I=\boldsymbol{\Phi}(\boldsymbol{x})\,\hat{\boldsymbol{u}}, \end{aligned} \tag{29}$$

and the shape function $\boldsymbol{\Phi}(\boldsymbol{x})$ is defined as

$$\boldsymbol{\Phi}(\boldsymbol{x})=\boldsymbol{p}^{\mathrm{T}}(\boldsymbol{x})\,\boldsymbol{G}_{\mathrm{a}}+\boldsymbol{R}^{\mathrm{T}}(\boldsymbol{x})\,\boldsymbol{G}_{\mathrm{b}}. \tag{30}$$

The equations for calculating the partial derivative of the shape function can be correspondingly given by

$$\begin{cases} \boldsymbol{\Phi}_{,i}(\boldsymbol{x})=\boldsymbol{p}_{,i}^{\mathrm{T}}(\boldsymbol{x})\,\boldsymbol{G}_{\mathrm{a}}+\boldsymbol{R}_{,i}^{\mathrm{T}}(x)\boldsymbol{G}_{\mathrm{b}} \\ \boldsymbol{\Phi}_{,ij}(\boldsymbol{x})=\boldsymbol{p}_{,ij}^{\mathrm{T}}(\boldsymbol{x})\,\boldsymbol{G}_{\mathrm{a}}+\boldsymbol{R}_{,ij}^{\mathrm{T}}(x)\boldsymbol{G}_{\mathrm{b}} \end{cases} \tag{31}$$

where

$$\begin{cases} \boldsymbol{R}_{,i}^{\mathrm{T}}=\boldsymbol{R}_{,r}^{\mathrm{T}}r_{,i} \\ \boldsymbol{R}_{,ij}^{\mathrm{T}}=\boldsymbol{R}_{,rr}^{\mathrm{T}}r_{,i}r_{,j}+\boldsymbol{R}_{,r}^{\mathrm{T}}r_{,ij} \end{cases} \tag{32}$$

4. Vertical TBIS based on the plate model

4.1. Bridge mechanical model built by meshless method

First, the mechanical model of the bridge is constructed using the approaches described in 3.1 and 3.2, and the stiffness matrix $\boldsymbol{K}_{\mathrm{b}}$, mass matrix $\boldsymbol{M}_{\mathrm{b}}$, and damping matrix $\boldsymbol{C}_{\mathrm{b}}$ of the bridge can be calculated.

The approximate displacement field established by RPIM can be expressed as

$$\hat{\boldsymbol{u}}_0 = \begin{Bmatrix} u_0 \\ v_0 \\ w_0 \\ \theta_x \\ \theta_y \end{Bmatrix} = \sum_{I=1}^{NP} \varPhi_I \begin{Bmatrix} u_{0I} \\ v_{0I} \\ w_{0I} \\ \theta_{xI} \\ \theta_{yI} \end{Bmatrix} = \boldsymbol{\varPhi}\hat{\boldsymbol{u}} \tag{33}$$

Therefore, we have

$$\boldsymbol{\varepsilon} = \begin{Bmatrix} \boldsymbol{\varepsilon}_0 \\ \boldsymbol{\kappa} \\ \boldsymbol{\gamma}_0 \end{Bmatrix} = \begin{Bmatrix} \boldsymbol{B}_{\mathrm{I}} \\ \boldsymbol{B}_{\mathrm{II}} \\ \boldsymbol{B}_{\mathrm{III}} \end{Bmatrix} \hat{\boldsymbol{u}} = \boldsymbol{B}\hat{\boldsymbol{u}} \tag{34}$$

where $\boldsymbol{B}_{\mathrm{I}}$, $\boldsymbol{B}_{\mathrm{II}}$, and $\boldsymbol{B}_{\mathrm{III}}$ are the derivative matrix of the shape function, which can be written as

$$\boldsymbol{B}_{\mathrm{I}} = \begin{bmatrix} \boldsymbol{B}_{\mathrm{I}}^1 & \boldsymbol{B}_{\mathrm{I}}^2 & \cdots & \boldsymbol{B}_{\mathrm{I}}^I & \cdots & \boldsymbol{B}_{\mathrm{I}}^{NP} \end{bmatrix},\ \boldsymbol{B}_{\mathrm{I}}^I = \begin{bmatrix} \varPhi_{I,x} & 0 & 0 & 0 & 0 \\ 0 & \varPhi_{I,y} & 0 & 0 & 0 \\ \varPhi_{I,y} & \varPhi_{I,x} & 0 & 0 & 0 \end{bmatrix} \tag{35}$$

$$\boldsymbol{B}_{\mathrm{II}} = \begin{bmatrix} \boldsymbol{B}_{\mathrm{II}}^1 & \boldsymbol{B}_{\mathrm{II}}^2 & \cdots & \boldsymbol{B}_{\mathrm{II}}^I & \cdots & \boldsymbol{B}_{\mathrm{II}}^{NP} \end{bmatrix},\ \boldsymbol{B}_{\mathrm{II}}^I = \begin{bmatrix} 0 & 0 & 0 & \varPhi_{I,x} & 0 \\ 0 & 0 & 0 & 0 & \varPhi_{I,y} \\ 0 & 0 & 0 & \varPhi_{I,y} & \varPhi_{I,x} \end{bmatrix} \tag{36}$$

$$\boldsymbol{B}_{\mathrm{III}} = \begin{bmatrix} \boldsymbol{B}_{\mathrm{III}}^1 & \boldsymbol{B}_{\mathrm{III}}^2 & \cdots & \boldsymbol{B}_{\mathrm{III}}^I & \cdots & \boldsymbol{B}_{\mathrm{III}}^{NP} \end{bmatrix},\ \boldsymbol{B}_{\mathrm{III}}^I = \begin{bmatrix} 0 & 0 & \varPhi_{I,y} & 0 & \varPhi_I \\ 0 & 0 & \varPhi_{I,x} & \varPhi_I & 0 \end{bmatrix} \tag{37}$$

where $\varPhi_{I,x}$ and $\varPhi_{I,y}$ denote that $\varPhi_I$ takes first-order partial derivatives with respect to x and y, respectively.

According to Ref. [58], we define $\boldsymbol{K}_{\mathrm{b}} = \int_\varOmega \boldsymbol{B}^T\boldsymbol{S}\boldsymbol{B}\mathrm{d}\varOmega$, then we have

$$\begin{aligned} \boldsymbol{K}_{\mathrm{b}} = \int_\varOmega \boldsymbol{B}^{\mathrm{T}}\boldsymbol{S}\boldsymbol{B}\mathrm{d}\varOmega &= \int_\varOmega \begin{Bmatrix} \boldsymbol{B}_{\mathrm{I}} \\ \boldsymbol{B}_{\mathrm{II}} \\ \boldsymbol{B}_{\mathrm{III}} \end{Bmatrix}^{\mathrm{T}} \begin{bmatrix} \boldsymbol{A} & \bar{\boldsymbol{B}} & 0 \\ \bar{\boldsymbol{B}} & \boldsymbol{D} & 0 \\ 0 & 0 & \boldsymbol{A}_{\mathrm{s}} \end{bmatrix} \begin{Bmatrix} \boldsymbol{B}_{\mathrm{I}} \\ \boldsymbol{B}_{\mathrm{II}} \\ \boldsymbol{B}_{\mathrm{III}} \end{Bmatrix} \mathrm{d}\varOmega \\ &= \int_\varOmega \boldsymbol{B}_{\mathrm{I}}^{\mathrm{T}}\boldsymbol{A}\boldsymbol{B}_{\mathrm{I}} + \boldsymbol{B}_{\mathrm{II}}^{\mathrm{T}}\bar{\boldsymbol{B}}\boldsymbol{B}_{\mathrm{I}} + \boldsymbol{B}_{\mathrm{I}}^{\mathrm{T}}\bar{\boldsymbol{B}}\boldsymbol{B}_{\mathrm{II}} \qquad (38) \\ &+ \boldsymbol{B}_{\mathrm{II}}^{\mathrm{T}}\boldsymbol{D}\boldsymbol{B}_{\mathrm{II}} + \boldsymbol{B}_{\mathrm{III}}^{\mathrm{T}}\boldsymbol{A}_{\mathrm{s}}\boldsymbol{B}_{\mathrm{III}}\,\mathrm{d}\varOmega \qquad (39) \end{aligned}$$

Defining $\boldsymbol{M}_{\mathrm{b}} = \int_{\Omega} \boldsymbol{N}_{\Phi}^{\mathrm{T}} \boldsymbol{\rho} \boldsymbol{N}_{\Phi} \mathrm{d}\Omega$, where $\boldsymbol{N}_{\Phi}$ is the shape function matrix, which can be expressed as

$$\boldsymbol{N}_{\Phi} = \begin{bmatrix} \boldsymbol{N}_{\Phi 1} & \boldsymbol{N}_{\Phi 2} & \cdots & \boldsymbol{N}_{\Phi I} & \cdots & \boldsymbol{N}_{\Phi NP} \end{bmatrix} \tag{40}$$

where

$$\boldsymbol{N}_{\Phi I} = \begin{bmatrix} \Phi_I & 0 & 0 & 0 & 0 \\ 0 & \Phi_I & 0 & 0 & 0 \\ 0 & 0 & \Phi_I & 0 & 0 \\ 0 & 0 & 0 & \Phi_I & 0 \\ 0 & 0 & 0 & 0 & \Phi_I \end{bmatrix} \tag{41}$$

and

$$\boldsymbol{\rho} = \begin{bmatrix} I_0 & 0 & 0 & I_1 & 0 \\ 0 & I_0 & 0 & 0 & I_1 \\ 0 & 0 & I_0 & 0 & 0 \\ I_1 & 0 & 0 & I_2 & 0 \\ 0 & I_1 & 0 & 0 & I_2 \end{bmatrix} \tag{42}$$

where I_0, I_1, and I_2 denote the normal, coupled normal-rotary and rotary inertial coefficients, respectively, and they can be given by

$$(I_0, I_1, I_2) = \int_{-h/2}^{h/2} \rho(z) \left(1, z, z^2\right) dz \tag{43}$$

For the damping matrix $\boldsymbol{C}_{\mathrm{b}}$, we use Rayleigh damping, i.e.

$$\boldsymbol{C}_{\mathrm{b}} = a_{\mathrm{r}} \boldsymbol{M}_{\mathrm{b}} + b_{\mathrm{r}} \boldsymbol{K}_{\mathrm{b}} \tag{44}$$

with

$$\begin{aligned} a_{\mathrm{r}} &= \frac{2\zeta_{\mathrm{b}} \omega_1 \omega_2}{\omega_1 + \omega_2} \\ b_{\mathrm{r}} &= \frac{2\zeta_{\mathrm{b}}}{\omega_1 + \omega_2} \end{aligned} \tag{45}$$

where ω_1 and ω_2 are the first two orders of natural frequencies of the bridge, and ζ_{b} denotes the bridge damping ratio.

4.2. The block matrices and vectors of the TBIS

In this subsection, the bridge matrices $\boldsymbol{K}_{\mathrm{bb}}$, $\boldsymbol{M}_{\mathrm{bb}}$, and $\boldsymbol{C}_{\mathrm{bb}}$, as well as the train-bridge coupling matrices $\boldsymbol{K}_{\mathrm{vb}}$, $\boldsymbol{K}_{\mathrm{bv}}$, $\boldsymbol{C}_{\mathrm{vb}}$, and $\boldsymbol{C}_{\mathrm{bv}}$, are calculated using the principle of total potential energy with a stationary value in elastic system dynamics, as described in the Ref. [17, 49]. The load vectors $\boldsymbol{F}_{\mathrm{vv}}$, $\boldsymbol{F}_{\mathrm{vv}}$, and $\boldsymbol{F}_{\mathrm{bb}}$ are also determined using the same principle.

$\boldsymbol{K}_{\mathrm{bb}}$ contains two components: the stiffness matrix for all spans of the bridge, and the stiffness of the primary suspensions bound to the bridge, i.e.

$$\boldsymbol{K}_{\mathrm{bb}} = \mathrm{diag}\begin{bmatrix}\boldsymbol{K}_{\mathrm{b1}} & \boldsymbol{K}_{\mathrm{b2}} & \cdots & \boldsymbol{K}_{\mathrm{b}M}\end{bmatrix} + {\boldsymbol{N}_{\mathrm{bl}}}^{\mathrm{T}}\boldsymbol{k}_{\mathrm{b}}\boldsymbol{N}_{\mathrm{bl}} + {\boldsymbol{N}_{\mathrm{br}}}^{\mathrm{T}}\boldsymbol{k}_{\mathrm{b}}\boldsymbol{N}_{\mathrm{br}} \tag{46}$$

where the subscript M indicates that the bridge has a total of M spans. The matrix $\boldsymbol{k}_{\mathrm{b}}$ consists of the spring stiffness matrices of the primary suspensions, which are connected to the bridge stiffness matrix through the time-varying shape function matrix $\boldsymbol{N}_{\mathrm{b}}$. The subscripts l and r denote the left and right wheels of the wheelset, respectively. The expression for $\boldsymbol{k}_{\mathrm{b}}$ is given by

$$\boldsymbol{k}_{\mathrm{b}} = \mathrm{diag}\begin{bmatrix}\boldsymbol{k}_{\mathrm{b1}} & \boldsymbol{k}_{\mathrm{b2}} & \cdots & \boldsymbol{k}_{\mathrm{b}J}\end{bmatrix} \tag{47}$$

where the subscript J denotes the left (right) wheel of the J-th wheelset, then $\boldsymbol{k}_{\mathrm{b}i}$ can be written as

$$\boldsymbol{k}_{\mathrm{b}i} = \mathrm{diag}\begin{bmatrix}0 & 0 & k_{\mathrm{p}} & 0 & 0\end{bmatrix} \tag{48}$$

Since wheelsets are constantly moving along the rail, the shape function matrix $\boldsymbol{N}_{\mathrm{b}}$ also varies with time. Specifically, for $\boldsymbol{N}_{\mathrm{bl}}$, it can be expressed as

$$
\boldsymbol{N}_{\mathrm{bl}} = \begin{bmatrix}
\vdots & & & \vdots & & & \vdots & & & \vdots & & & \vdots \\
 & \Phi_{x,i} & 0 & 0 & 0 & 0 & & \Phi_{x,j} & 0 & 0 & 0 & 0 & \\
 & 0 & \Phi_{x,i} & 0 & 0 & 0 & & 0 & \Phi_{x,j} & 0 & 0 & 0 & \\
\cdots & 0 & 0 & \Phi_{x,i} & 0 & 0 & \cdots & 0 & 0 & \Phi_{x,j} & 0 & 0 & \cdots \\
 & 0 & 0 & 0 & \Phi_{x,i} & 0 & & 0 & 0 & 0 & \Phi_{x,j} & 0 & \\
 & 0 & 0 & 0 & 0 & \Phi_{x,i} & & 0 & 0 & 0 & 0 & \Phi_{x,j} & \\
\vdots & & & \vdots & & & \vdots & & & \vdots & & & \vdots \\
 & \Phi_{y,k} & 0 & 0 & 0 & 0 & & \Phi_{y,l} & 0 & 0 & 0 & 0 & \\
 & 0 & \Phi_{y,k} & 0 & 0 & 0 & & 0 & \Phi_{y,l} & 0 & 0 & 0 & \\
\cdots & 0 & 0 & \Phi_{y,k} & 0 & 0 & \vdots & 0 & 0 & \Phi_{y,l} & 0 & 0 & \vdots \\
 & 0 & 0 & 0 & \Phi_{y,k} & 0 & & 0 & 0 & 0 & \Phi_{y,l} & 0 & \\
 & 0 & 0 & 0 & 0 & \Phi_{y,k} & & 0 & 0 & 0 & 0 & \Phi_{y,l} & \\
\vdots & & & \vdots & & & \vdots & & & \vdots & & & \vdots
\end{bmatrix} \tag{49}
$$

where the subscripts x and y represent the wheelset serial numbers, while i, j, k, and l represent the serial numbers of the supporting points within the supporting domain centered on the wheel. For ease of understanding, the shape function matrix at moment t, $\boldsymbol{N}_{\mathrm{bl}}$, can be determined by Fig. 5.

Next, the train-bridge coupling matrix $\boldsymbol{K}_{\mathrm{vb}}$ can be given by

$$
\boldsymbol{K}_{\mathrm{vb}} = \boldsymbol{k}_{\mathrm{vb}} \boldsymbol{N}_{\mathrm{bl}} + \boldsymbol{k}_{\mathrm{vb}} \boldsymbol{N}_{\mathrm{br}} \tag{50}
$$

where $\boldsymbol{N}_{\mathrm{bl}}$, $\boldsymbol{N}_{\mathrm{br}}$ have been given before, and $\boldsymbol{k}_{\mathrm{vb}}$ can be written as

$$
\boldsymbol{k}_{\mathrm{vb}} = \begin{bmatrix}
\boldsymbol{k}_{\mathrm{vb1}} & & & \\
 & \boldsymbol{k}_{\mathrm{vb2}} & & \\
 & & \ddots & \\
 & & & \boldsymbol{k}_{\mathrm{vb}N}
\end{bmatrix} \tag{51}
$$

where the subscript N indicates that there are N vehicles in the train, then $\boldsymbol{k}_{\mathrm{vb}i}$ can be written as

$$
\boldsymbol{k}_{\mathrm{vb}i} = \begin{bmatrix}
\mathbf{0} & \mathbf{0} \\
\boldsymbol{\lambda}_{\mathrm{vb}} & \mathbf{0} \\
\mathbf{0} & \boldsymbol{\lambda}_{\mathrm{vb}}
\end{bmatrix} \tag{52}
$$

with

$$
\lambda_{\mathrm{vb}} = \begin{bmatrix}
0 & 0 & -k_{\mathrm{p}} & 0 & 0 & 0 & 0 & -k_{\mathrm{p}} & 0 & 0 \\
0 & 0 & -k_{\mathrm{p}} L_{\mathrm{t}} & 0 & 0 & 0 & 0 & k_{\mathrm{p}} L_{\mathrm{t}} & 0 & 0
\end{bmatrix} \tag{53}
$$

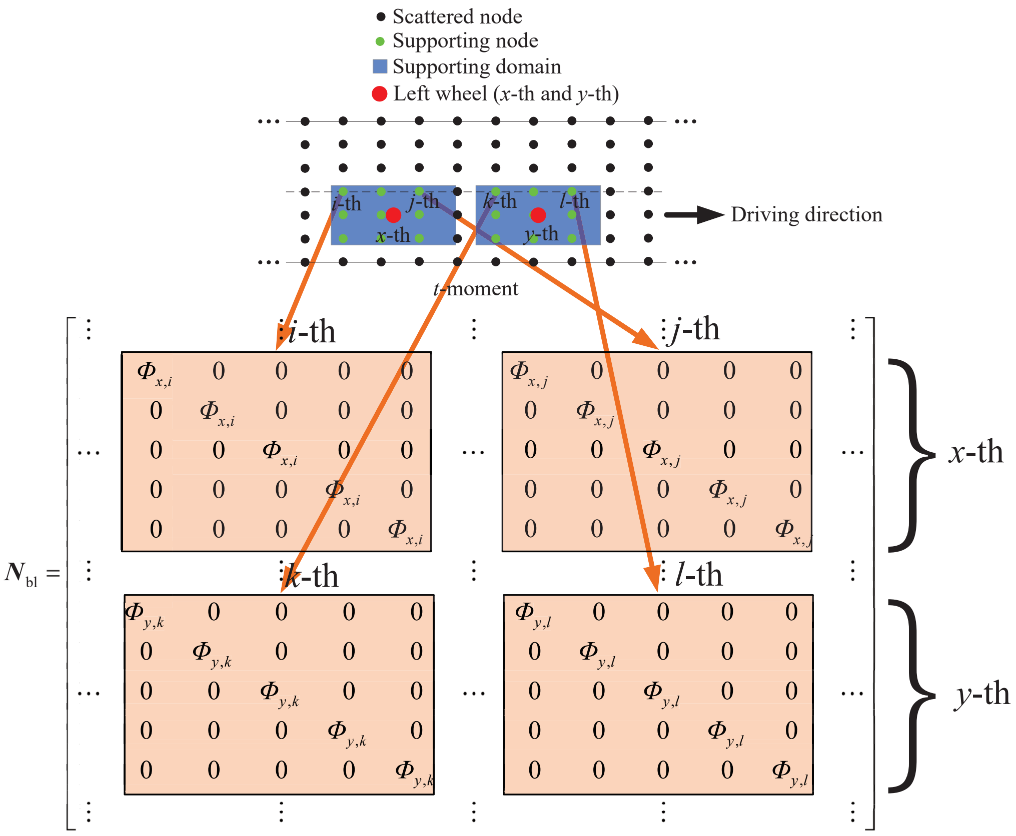

Figure 5: The shape function matrix $\boldsymbol{N}_{\mathrm{bl}}$ at moment t.

and transposing $\boldsymbol{K}_{\mathrm{vb}}$ gives $\boldsymbol{K}_{\mathrm{bv}}$, i.e. $\boldsymbol{K}_{\mathrm{bv}} = {\boldsymbol{K}_{\mathrm{vb}}}^{\mathrm{T}}$.

For the mass matrix $\boldsymbol{M}_{\mathrm{bb}}$, it has a similar form to $\boldsymbol{K}_{\mathrm{bb}}$, i.e.

$$\boldsymbol{M}_{\mathrm{bb}} = \mathrm{diag}\left[\boldsymbol{M}_{\mathrm{b1}} \quad \boldsymbol{M}_{\mathrm{b2}} \quad \cdots \quad \boldsymbol{M}_{\mathrm{b}M}\right] + {\boldsymbol{N}_{\mathrm{bl}}}^{\mathrm{T}} \boldsymbol{m}_{\mathrm{b}} \boldsymbol{N}_{\mathrm{bl}} + {\boldsymbol{N}_{\mathrm{br}}}^{\mathrm{T}} \boldsymbol{m}_{\mathrm{b}} \boldsymbol{N}_{\mathrm{br}} \tag{54}$$

with

$$\boldsymbol{m}_{\mathrm{b}} = \mathrm{diag}\left[\boldsymbol{m}_{\mathrm{b1}} \quad \boldsymbol{m}_{\mathrm{b2}} \quad \cdots \quad \boldsymbol{m}_{\mathrm{b}J}\right] \tag{55}$$

$$\boldsymbol{m}_{\mathrm{b}i} = \mathrm{diag}\left[0 \quad 0 \quad m_{\mathrm{w}} \quad 0 \quad 0\right] \tag{56}$$

For the damping matrices $\boldsymbol{C}_{\mathrm{bb}}$, $\boldsymbol{C}_{\mathrm{bv}}$, and $\boldsymbol{C}_{\mathrm{vb}}$, we can obtain them by replacing $\boldsymbol{K}_{\mathrm{bb}}$, $\boldsymbol{K}_{\mathrm{bv}}$, and $\boldsymbol{K}_{\mathrm{vb}}$ with the corresponding damping coefficients.

For the load vectors $\boldsymbol{F}_{\mathrm{vv}}$ and $\boldsymbol{F}_{\mathrm{bb}}$, we have

$$\boldsymbol{F}_{\mathrm{vv}} = \boldsymbol{k}_{\mathrm{vb}} \boldsymbol{u}_{\mathrm{irrl}} + \boldsymbol{c}_{\mathrm{vb}} \boldsymbol{v}_{\mathrm{irrl}} + \boldsymbol{k}_{\mathrm{vb}} \boldsymbol{u}_{\mathrm{irrr}} + \boldsymbol{c}_{\mathrm{vb}} \boldsymbol{v}_{\mathrm{irrr}} \tag{57}$$

$$\begin{aligned} \boldsymbol{F}_{\mathrm{bb}} = & -{\boldsymbol{N}_{\mathrm{bl}}}^{\mathrm{T}} \boldsymbol{c}_{\mathrm{b}} \boldsymbol{u}_{\mathrm{irrl}} - {\boldsymbol{N}_{\mathrm{bl}}}^{\mathrm{T}} \boldsymbol{k}_{\mathrm{b}} \boldsymbol{v}_{\mathrm{irrl}} - {\boldsymbol{N}_{\mathrm{bl}}}^{\mathrm{T}} \boldsymbol{m}_{b} \boldsymbol{a}_{\mathrm{irrl}} - {\boldsymbol{N}_{\mathrm{bl}}}^{\mathrm{T}} \boldsymbol{g}_{\mathrm{irrl}} \\ & - {\boldsymbol{N}_{\mathrm{br}}}^{\mathrm{T}} \boldsymbol{k}_{\mathrm{b}} \boldsymbol{u}_{\mathrm{irrr}} - {\boldsymbol{N}_{\mathrm{br}}}^{\mathrm{T}} \boldsymbol{c}_{\mathrm{b}} \boldsymbol{v}_{\mathrm{irrr}} - {\boldsymbol{N}_{\mathrm{br}}}^{\mathrm{T}} \boldsymbol{m}_{b} \boldsymbol{a}_{\mathrm{irrr}} - {\boldsymbol{N}_{\mathrm{br}}}^{\mathrm{T}} \boldsymbol{g}_{\mathrm{irrr}} \end{aligned} \tag{58}$$

where $\boldsymbol{c}_{\mathrm{vb}}$ can be obtained by replacing k_{p} in $\boldsymbol{k}_{\mathrm{vb}}$ with c_{p}. Similarly, $\boldsymbol{c}_{\mathrm{b}}$ can be obtained by replacing k_{p} in $\boldsymbol{k}_{\mathrm{b}}$ with c_{p}. $\boldsymbol{u}_{\mathrm{irr}}$, $\boldsymbol{v}_{\mathrm{irr}}$, and $\boldsymbol{a}_{\mathrm{irr}}$ are the corresponding rail irregularity (i.e., vertical displacement), rail velocity, and rail acceleration of the train at moment t. Taking $\boldsymbol{u}_{\mathrm{irrl}}$ as an example,it can be written as

$$\boldsymbol{u}_{\mathrm{irrl}} = \left[\boldsymbol{u}_{\mathrm{irrl1}} \quad \boldsymbol{u}_{\mathrm{irrl2}} \quad \ldots \quad \boldsymbol{u}_{\mathrm{irrl}J}\right]^{\mathrm{T}} \tag{59}$$

with

$$\boldsymbol{u}_{\mathrm{irrl}i} = \left[0 \quad 0 \quad u_{\mathrm{l}i} \quad 0 \quad 0\right] \tag{60}$$

where $u_{\mathrm{l}i}$ denotes the rail irregularity corresponding to the left wheel of the i-th wheel pair at moment t. $\boldsymbol{v}_{\mathrm{irr}}$ and $\boldsymbol{a}_{\mathrm{irr}}$ can be obtained by taking first-order and second-order differences on $\boldsymbol{u}_{\mathrm{irr}}$.

By now, we solve all block matrices in Eq. (6). Then we can get the displacement, velocity, and acceleration of the train and bridge at each time step by Newmark-β method.

5. Rail irregularity

To facilitate a comparison with the model discussed in Ref. [16], we adopt German low-interference rail irregularity spectrum in Ref. [16] for this study, which applies to high-speed railway with speeds of 250 km/h and above. The power spectral density of rail irregularity primarily encompasses spectra from China, Germany, and United States. However, different rail irregularity spectrums do not affect the conclusions of model comparisons.

The spectrum is used to generate the vertical rail irregularity [59], i.e.

$$S_{\mathrm{V}} = \frac{A_{\mathrm{v}}}{\left(\Omega^2 + \Omega_{\mathrm{r}}^2\right)\left(\Omega^2 + \Omega_{\mathrm{c}}^2\right)} \tag{61}$$

where,for the case of low-interferenc, the parameters $\Omega_{\mathrm{r}} = 0.0206$, $\Omega_{\mathrm{c}} = 0.8246$, and $A_{\mathrm{v}} = 4.032 \times 10^{-7}$. The trigonometric series method [60] is used to generate the rail irregularity and the spatial frequency $\Omega \in [0.05, 0.3]$ rad/m.

Using Eqs. (62) and (63) to modulate the rail irregularity on the bridge [61], i.e.

$$z_{\mathrm{r}}(x) = \Phi(x)\hat{z}_{\mathrm{r}}(x) \tag{62}$$

$$\Phi(x) = \begin{cases} 0.5\left(1+\sqrt{c}\right) + 0.5\left(1-\sqrt{c}\right)\sin\left(\pi L_0^{-1}\left(x+1.5L_0\right)\right) & -L_0 \le x < 0 \\ \sqrt{c} & 0 \le x < L \\ 0.5\left(1+\sqrt{c}\right) + 0.5\left(1-\sqrt{c}\right)\sin\left(\pi L_0^{-1}\left(-x-L-0.5L_0\right)\right) & L \le x < L + L_0 \\ 1 & \text{other} \end{cases} \tag{63}$$

where $\hat{z}_{\mathrm{r}}(x)$ is the original rail irregularity generated by trigonometric series method, and $\Phi(x)$ is the modulation function. c is the modulation coefficient, L is the total length of the rail irregularity, and L_0 is the modulation transition length. In this study, c is taken as 0.7, L_0 is taken as 20 m.

6. Numerical examples

Based on the previous sections, we construct a vertical TBIS consisting of a 1-span 32-meter simply supported bridge and a train, as depicted in Fig. (6). In TBIS programs, simply supported box girders are commonly used for bridges, where different spans are not directly connected to each other, but the response is transmitted through the rails and piers. To more directly highlight the differences between the plate and beam models, we have excluded the track and pier models, resulting in no interaction between different span bridges. Therefore, a single-span bridge model is sufficient to achieve the research objectives. Meanwhile, it allows for more detailed mesh division, which is particularly beneficial when dealing with limited computing power. The train consists of 4 cars arranged as motor car + trailer car +

trailer car + motor car. German power spectrum is used to generate the rail irregularity for a total length of 1000 m. To ensure the stability of the initial condition, the train starts at 150 m at the first car distance from the bridgehead, and the calculation is over after the first car passes the bridge 150 m. The train speed is 300 Km/h. We list the main train parameters in Tab. 2.

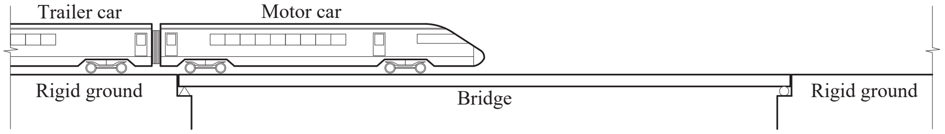

Figure 6: The TBIS of the numerical example.

Table 2: The parameters of cars.

Parameter	Unit	Motor car/Trailer car
m_c	kg	4.4×10^4 / 4.8×10^4
J_c	$\mathrm{kg} \cdot \mathrm{m}^2$	2.7×10^6 / 2.7×10^6
m_t	kg	2.4×10^3 / 3.2×10^3
J_t	$\mathrm{kg} \cdot \mathrm{m}^2$	2.2×10^3 / 7.2×10^3
m_w	kg	1.2×10^3
k_s	N/m	6×10^5 / 8×10^5
c_s	$\mathrm{N} \cdot \mathrm{s/m}$	8×10^4 / 9×10^4
k_p	N/m	1.4×10^6 / 2.08×10^6
c_p	$\mathrm{N} \cdot \mathrm{s/m}$	8×10^4 / 6×10^4
L_c	m	8.6875/8.6875
L_t	m	1.25/1.25

We consider two different approaches to model the bridge: One of them is FEM using two-node four-DOF Euler beam element [16], the other is the meshless method discussed in the previous section. The comparison between the beam model and plate model presented in this paper is, in fact, a comparison between the conventional TBIS and the proposed modified TBIS. In previous studies of TBIS, including the work cited in Ref. [1, 16, 17, 62], utilized Euler beams rather than Timoshenko beams to model simply supported girder bridges. In our work, the plate model-based TBIS is an improvement upon the approach introduced in Ref. [16]. The earlier literature simplified simply supported girder bridges to Euler beams, leading us to employ Euler beams-Reissner-Mindlin plates for the comparison in our study. The material properties of the bridge are as follows: Young's modulus is 3.451×10^{10} N/m^2, Poisson's ratio is 0.2, density is 2.65×10^3 kg/m^3, damping ratio is 0.05, and bridge width is 13 m.

In the FEM modeling, the bridge is divided into 64 equidistant elements. For the meshless method, a total of 27×65 nodes are distributed equidistantly in both the x and y directions, and the discretization of the model by FEM and RPIM can be seen in Fig. 7. In RPIM, particularly for two-dimensional problems, the quadratic complete polynomial basis functions can be written as

$$\boldsymbol{p}\left(\boldsymbol{x}\right) = \begin{bmatrix} 1 & x & y & x^2 & xy & y^2 \end{bmatrix}^{\mathrm{T}}. \tag{64}$$

The scale influence factor χ, which is used to control the size of the supporting domain, is typically chosen within the range of 2.0 to 3.0. As suggested by Ref. [39, 63], in this paper, a specific value of 2.4 is adopted. At this setting, the support domain can accommodate up to 25 supporting nodes. At the end of this section, we will perform a sensitivity study on these parameters. Finally, the TBIS can be established as Fig. 8. The time step length for Newmark-β method is set to $\Delta_{\mathrm{t}} = 6 \times 10^{-4}$ s, i.e., the train runs $\Delta_{\mathrm{L}} = 0.05$ m for each time step. Thus, a total of 8524 time steps are required to complete the entire journey.

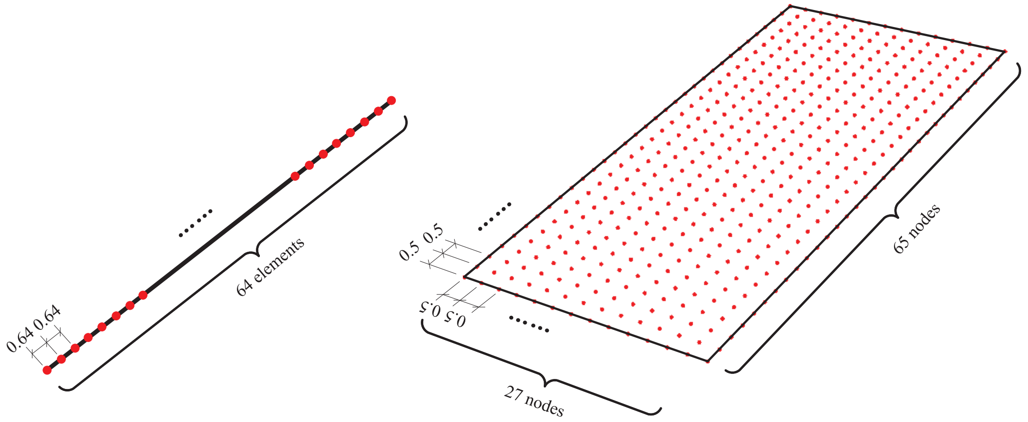

Finite element discretization

Meshless discretization

Figure 7: Discretization of the model by FEM and RPIM.

As most real engineering bridges are box girders, accurate determination of plate thickness parameters based on current literature is challenging.

Moreover, the width-thickness ratio W_{t} significantly affects the vibration of the plate. To address this, we calculate the dynamic responses of the plate model for different W_{t} values and compare them with the beam model. It is important to note that the cross-sectional area and flexural stiffness of the beam model vary with W_{t}. In both finite element and meshless methods, during the numerical modeling of Reissner-Mindlin plate, displacement and rotating angle are interpolated independently. This approach can introduce a new challenge known as shear locking. In civil engineering, the ratio of thickness to width, denoted as h/a, is commonly employed to classify plate structures as either thin or thick. Generally, when $h/a < 0.125$, a plate is considered thin; otherwise, it is categorized as thick or medium-thick. Shear locking tends to increase significantly when h/a is substantially less than 0.125. However, the width-to-thickness ratios investigated in this study range from 4 to 7, ensuring a minimum h/a of 0.143, which is greater than 0.125. Consequently, this paper eliminates the necessity to address shear locking concerns. In case shear locking does become an issue, reduced integration can be employed as a mitigating measure, if necessary.

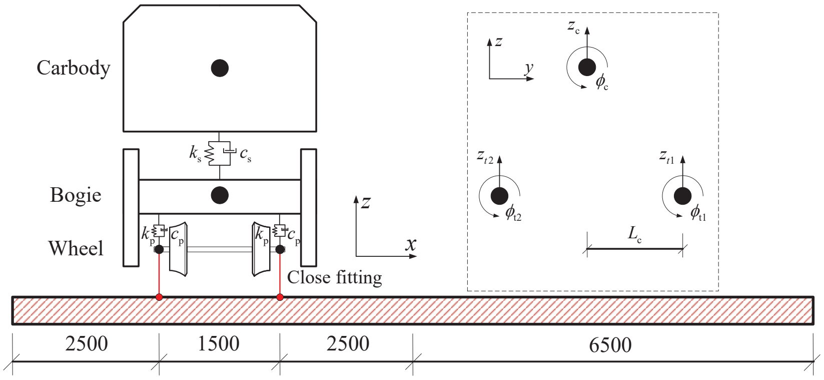

Figure 8: The TBIS based on plate model established by RPIM.

Fig. 9 shows the curve of mid-span vertical displacement of the two models changing with time when $W_{\mathrm{t}} = 5$. The beam model is constructed in the same way as we used in the Ref. [64], i.e., each span is modeled separately. In this modeling approach, each span of bridge (the width is 13 m, length is 32 m, and height is 2.6 m) is simplified into Euler beam elements. In terms of size, it seems to make more sense to simplify it to a plate. The beam model curve is plotted at a width coordinate of -0.5 m. The width coordinates ranging from 0 m to 13 m correspond to the changes in mid-span vertical displacement of the plate model along the width direction of the bridge. For the plate model, it can be clearly observed that the vertical displacement gradually increases in the width direction 0 m to 13 m. This occurs because, in this specific example, the train is set to run on the side of the width direction within the range of $0 \sim 6.5$ m. The specific position and wheel trajectories are depicted in Fig. 8. By comparing the projected curves of the beam model and plate model, it can be observed that the overall trends are similar. The bridge begins to bend down as the train drives onto it, and it starts to reset when the train begins to exit the bridge. Once all the cars of the train have completely crossed the bridge, the bridge enters a state of free vibration, and the amplitude gradually decreases due to the presence of damping. Eventually, the bridge returns to its initial state. Although both the beam model and plate model exhibit similar dynamic trends, substantial disparities in their response values are evident. These discrepancies can be attributed to differences in mechanical assumptions. Mechanically, beam and plate structures, characterized by significantly smaller scales in two directions and one direction, respectively, allow certain assumptions to be introduced in the analysis. These assumptions aim to simplify beams and plates into one-dimensional and two-dimensional problems, respectively, thereby facilitating their analytical solutions. In the specific example considered, the dimensions in the thickness direction are notably smaller than those in the width and length directions. Consequently, certain mechanical assumptions applicable to beam structures become invalid, leading to distorted calculation results. This discrepancy represents a critical factor contributing to the observed differences between the two models.

Fig. 10 displays the mid-span vertical displacements for different values of W_{t} (4, 5, 6, 7) in the models. The plot utilizes three colors: the red curve represents the beam model, while the blue and gray curves represent the plate model. Specifically, the blue curve corresponds to the displacements at the width coordinates of 0 m and 13 m, while the gray curve represents the displacement between 0 m and 13 m. By observing the variation in the longitudinal scale, it can be inferred that the mid-span vertical displacement increases with an increase in W_{t}. However, it is noteworthy that the increase is more pronounced in the beam model compared to the plate model. Furthermore, the amplitude of free vibration is much larger in the beam model than in the plate model. Consequently, larger values of W_{t} result in greater discrepancies between the two models. It is important to acknowledge that due to computational limitations, our simulation only considers a one-span

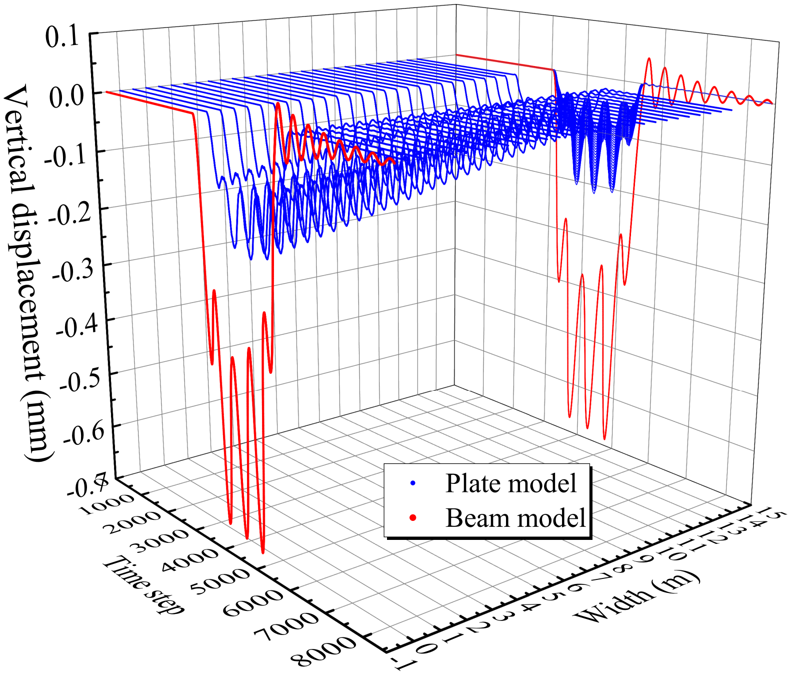

Figure 9: Curves of vertical displacements at mid-span with time for the plate and beam models ($W_{\mathrm{t}} = 5$).

bridge. In this context, utilizing a beam model for the simulation is not rigorous, considering the dimensions of the bridge. On the other hand, the proposed plate model in this paper provides more realistic data. For instance, while the beam model can only represent the overall displacement of a bridge section, the plate model offers variation in displacement along the width direction. The blue curve depicts the maximum and minimum vertical displacements of the section, while the gray curve envelopes the blue curve, demonstrating the variation in vertical displacement from one side of the bridge to the other.

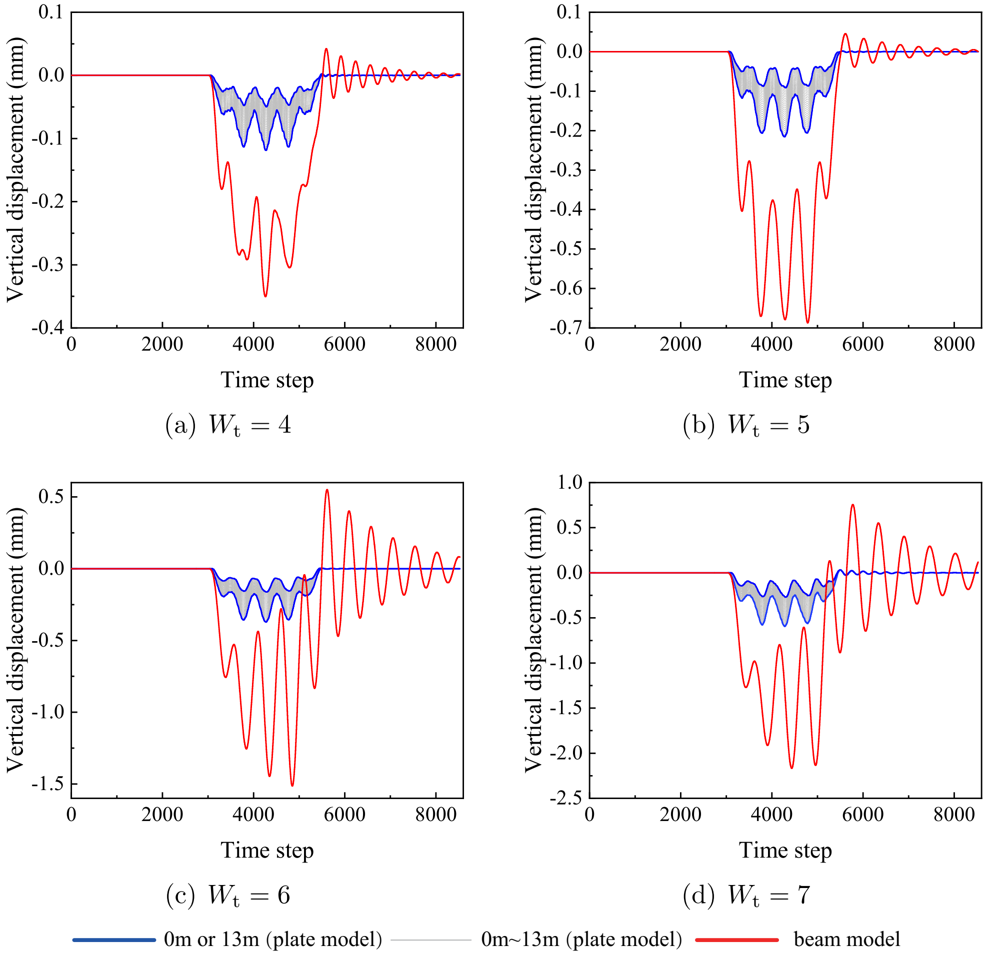

(a) $W_{\mathrm{t}} = 4$

(b) $W_{\mathrm{t}} = 5$

(c) $W_{\mathrm{t}} = 6$

(d) $W_{\mathrm{t}} = 7$

Figure 10: Mid-span vertical displacement of bridge built by plate model and beam model with different width-thickness ratio W_{t}

The trend analysis of the bridge span is performed and presented in Fig. 11. Upon examining the figure, it is evident that the analysis results of the beam model only provide the overall acceleration variation at the mid-span, whereas the plate model offers more detailed information. In the plate model, a noticeable disparity in acceleration variation can be observed between the traffic side and the other side. Furthermore, on the traffic side, the acceleration variation at the corresponding position of the wheel is more pronounced, with peaks reaching 0.5 $\mathrm{m/s^2}$. In terms of the overall trend, the mid-span acceleration variation increases with an increase in W_{t} for both models. However, the peak acceleration in the beam model is smaller than that in the plate model. Naturally, the two models exhibit similarity when considering only peak acceleration values when $W\mathrm{t}$ is lager. However, when examined in the frequency domain, variations may become evident. Furthermore, as W_{t} increases, the disparity in vertical displacement between the two models also magnifies. Consequently, we believe that the plate model continues to maintain its competitive edge. As a result, the plate model can provide more comprehensive response information for targeted analysis and design.

The analysis results of the carbody acceleration, specifically the vertical acceleration of the first motor car, are presented in Fig. 12. It is evident that the carbody acceleration exhibits a high degree of similarity between the two models, with only slight variations observed during the bridge crossing phase as W_{t} changes. This suggests that the bridge model has minimal influence on the carbody acceleration, which is primarily governed by rail irregularities. Since the same rail irregularities are employed in both models, the obtained figures exhibit similar patterns.

To validate the applicability of the proposed meshless computational framework, we conducted computations of the bridge ($W_{\mathrm{t}} = 5$) response at various train speeds, as depicted in Figs. 13 and 14. The figures reveal a gradual increase in the fluctuation of the bridge response with the rise in speed, consistent with analogous observations in the Ref. [16]. We plot the mid-span displacements and acceleration under trains comprising 6, 8, and 10 cars traversing the bridge in Figs. 15 and 16. It is evident that the number peak responses increase with the number of cars, indicating the adaptability of the proposed model to diverse train compositions. In Figs. 17 and 18, we reduce the discretization accuracy and plotted the mid-span responses for the final span of the bridge with 2, 3, and 4 spans. With an increase in the number of spans, the mid-span responses of the final span

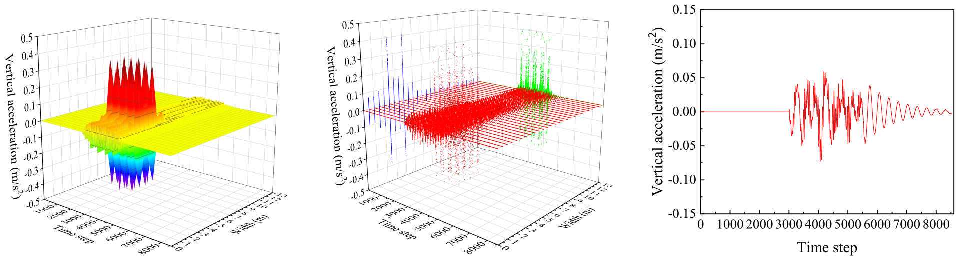

(a) $W_{\mathrm{t}} = 4$

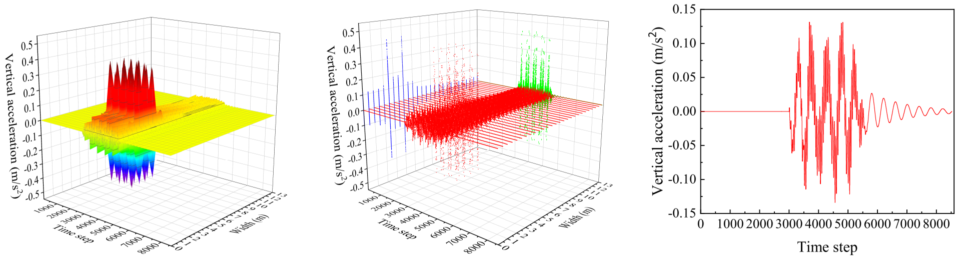

(b) $W_{\mathrm{t}} = 5$

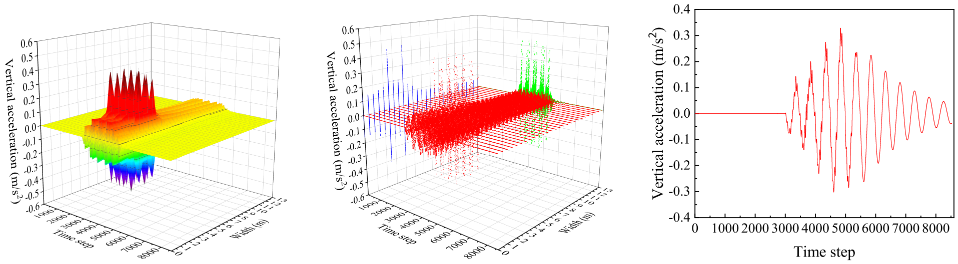

(c) $W_{\mathrm{t}} = 6$

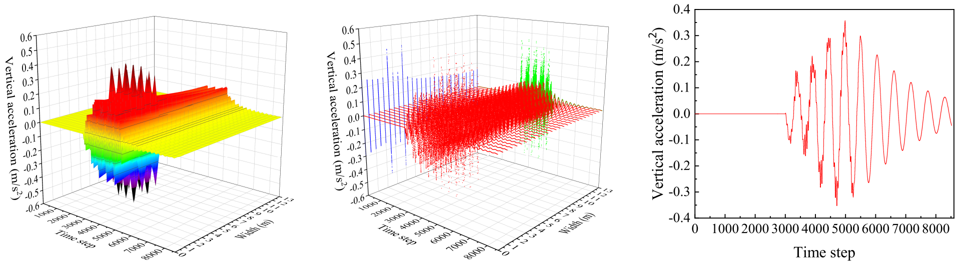

(d) $W_{\mathrm{t}} = 7$

Figure 11: Mid-span vertical acceleration of bridge built by plate model and beam model with different width-thickness ratio W_{t} (The figures on the left and center represent the mid-span acceleration surface and scatter point figure of the plate model, respectively. The figures on the right display the mid-span acceleration figure of the beam model)

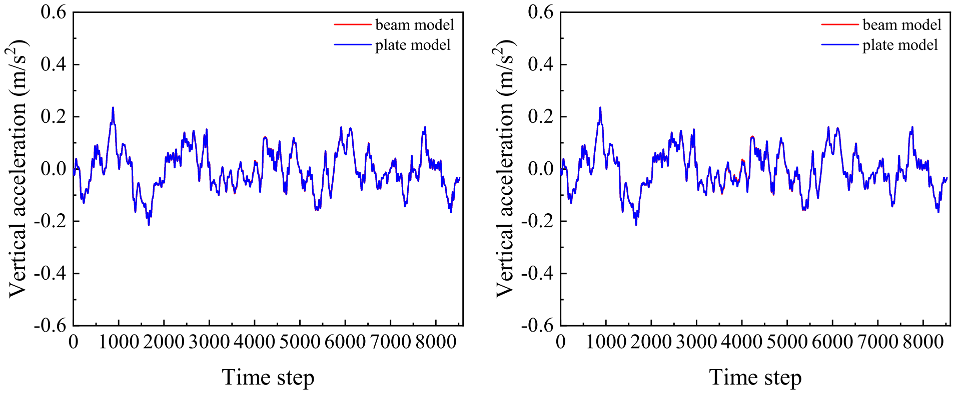

(a) $W_{\mathrm{t}} = 4$ (b) $W_{\mathrm{t}} = 5$

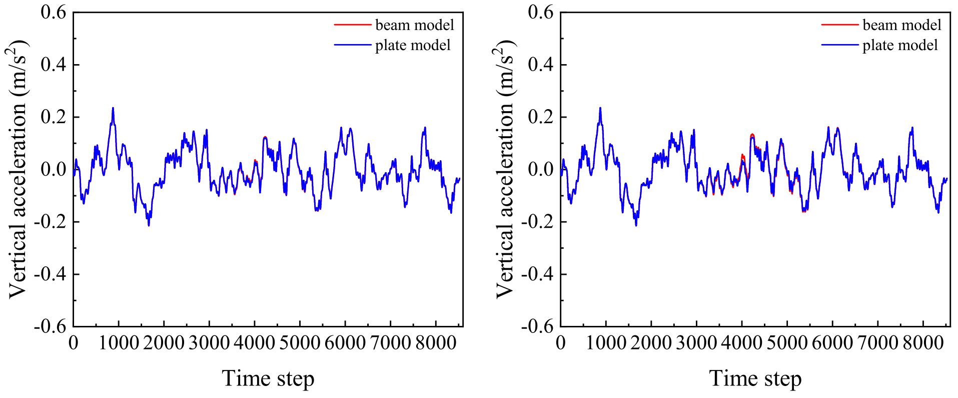

(c) $W_{\mathrm{t}} = 6$ (d) $W_{\mathrm{t}} = 7$

Figure 12: Vertical acceleration of the car body of the first motor car under plate model and beam model with different width-thickness ratio W_{t}

gradually rises. This is attributed to the increased number of spans, causing the train to experience more bridge influence before reaching the last span, thereby resulting in a slight elevation in the response of the last span bridge. Hence, the computational framework presented in this paper demonstrates commendable applicability.

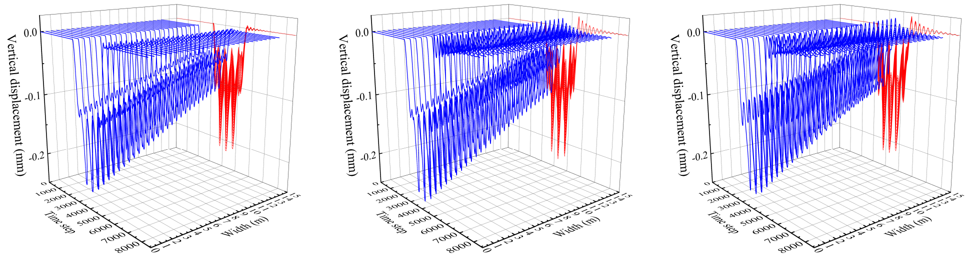

(a) 350 Km/h (b) 400 Km/h (c) 450 Km/h

Figure 13: Mid-span vertical displacement of the bridge under different train speeds ($W_{\mathrm{t}} = 5$).

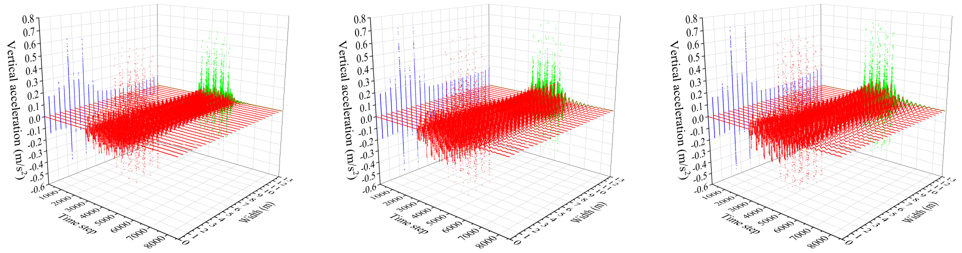

(a) 350 Km/h (b) 400 Km/h (c) 450 Km/h

Figure 14: Mid-span vertical acceleration of the bridge under different train speeds ($W_{\mathrm{t}} = 5$).

The stability and convergence of numerical simulation methods play crucial roles in determining their widespread applicability to such problems. Hence, we investigate the sensitivity of the structural response to discretization density and the scale influence factor χ. In Tab. 3, the vertical displacements of the bridge at coordinates $(0, 16)$ during the initial passage of the first motor car onto the bridge mid-span are provided. The results indicate that as the density of meshless discretization nodes increases, the structural response gradually converges and stabilizes regionally, ultimately reaching

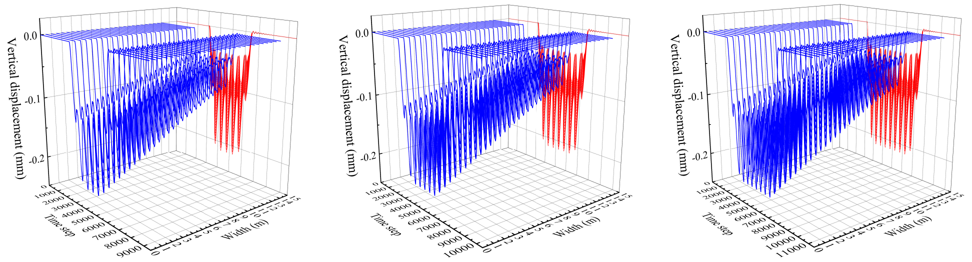

(a) 6 cars (b) 8 cars (c) 10 cars

Figure 15: Mid-span vertical displacement of the bridge under different number of cars ($W_t = 5$).

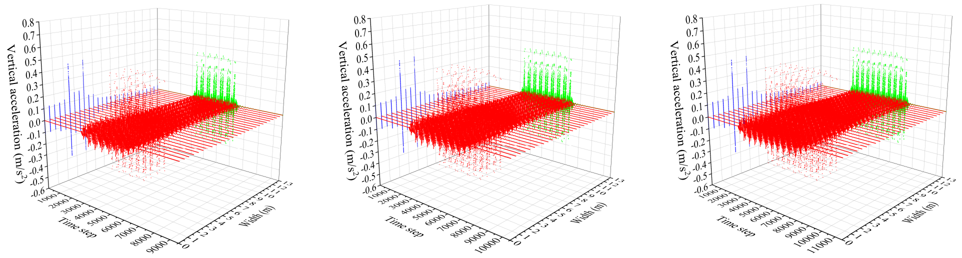

(a) 6 cars (b) 8 cars (c) 10 cars

Figure 16: Mid-span vertical acceleration of the bridge under different number of cars ($W_t = 5$).

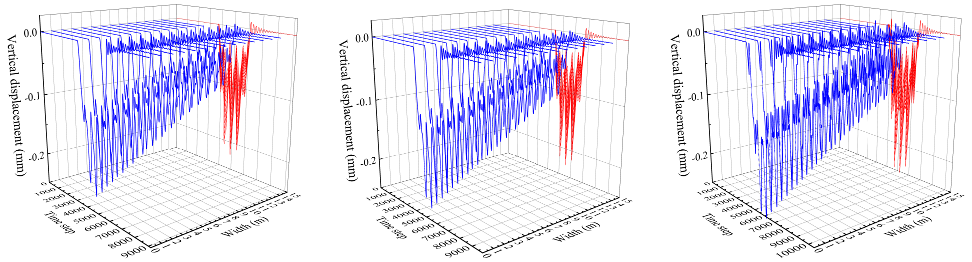

(a) 2 spans (b) 3 spans (c) 4 spans

Figure 17: Vertical displacement of the last span bridge with different number of spans ($W_t = 5$).

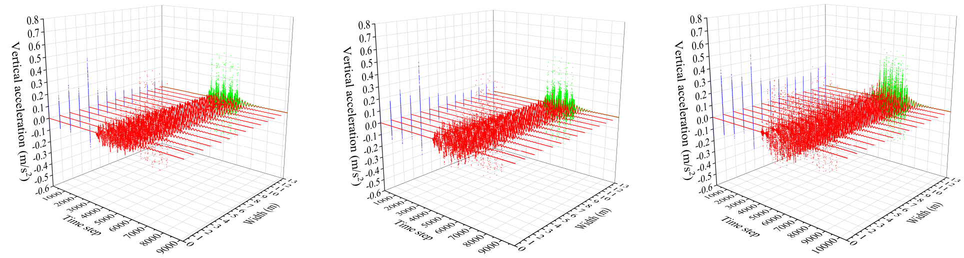

(a) 2 spans (b) 3 spans (c) 4 spans

Figure 18: Vertical acceleration of the last span bridge with different number of spans ($W_{\mathrm{t}} = 5$).

a converged value around -1.31×10^{-4} m. The scale influence factor χ, also affects the convergence speed. The fastest convergence is observed at $\chi = 3$. However, regardless of χ in the range of $2 \sim 3$, the structural response successfully converges and stabilizes with a 27×65 meshless node configuration. Consequently, the chosen value of $\chi = 2.4$ in our numerical examples is deemed appropriate in this study. This leads us to the conclusion that the proposed computational framework exhibits reliable stability and convergence.

Table 3: Sensitivity of stability and convergence for the structural vertical displacement ($\times 10^{-4}$ m) at coordinates (0,16) to the discretization density and scale influence factor χ when the first motor car runs into mid-span of the bridge ($W_{\mathrm{t}} = 5$).

χ	27×65	14×65	27×33	14×33	14×17	8×17
2.0	-1.130	-1.131	-1.130	-1.130	-1.128	-1.125
2.2	-1.130	-1.130	-1.127	-1.128	-1.117	-1.116
2.4	-1.131	-1.131	-1.128	-1.128	-1.115	-1.114
2.6	-1.131	-1.132	-1.129	-1.129	-1.118	-1.116
2.8	-1.130	-1.132	-1.129	-1.130	-1.126	-1.123
3.0	-1.130	-1.131	-1.130	-1.130	-1.129	-1.127

For the computational efficiency, an increase in model dimensionality (from one-dimensional to two-dimensional) almost inevitably leads to a reduction in computational efficiency. We list the CPU computation times for various models in Tab. 4. While computational efficiency experiences a significant decrease, it is not an insurmountable challenge. In our previous work, we successfully integrated various types of neural networks into the train-bridge system computational framework to predict dynamic responses, and the related results have been published [65–67]. These artificial intelligence agents effectively accelerate computations. Therefore, a similar approach could be considered to address the efficiency problem in our future work.

Table 4: CPU computation time for different models with different number of nodes.

Model	Node	Time (s)
Beam model	26	1.101
	51	3.046
	101	5.285
Plate model	8×17	116.750
	14×33	563.506
	27×65	3216.619

Until this juncture in the paper, we have verified the dynamic system of the vehicle coupled with the plate structure. We now propose a more refined system, as illustrated in Fig. 19, based on the findings of this study. Utilizing the FSDT-RPIM framework introduced in this paper, the top, web, and bottom plates with varying thickness [68] of the box girder bridge can be simulated and separately assembled, culminating in a higher level box girder model. The TBIS validated in this paper can be readily employed to couple the vehicle with the top plate. Simultaneously, the beam structure can be employed to simulate the pier and assembled with the bottom slab. This approach facilitates the construction of a higher level TBIS. The viability of this concept can be substantiated in future research. However, it is essential to note that the utilization of RPIM for discretizing the plate model in this study does not preclude the use of other methods. This research has demonstrated the applicability of meshless methods in the TBIS domain. Classical meshless methods such as the moving least square method, reproducing kernel particle method, and general finite difference method can be incorporated into the computational framework proposed in this paper. They only differ slightly in the imposition of boundary conditions and the wheel-plate coupling relationship. Thus, researchers can choose different methods based on specific needs when addressing this type of problem.

7. Conclusions

In this study, we propose a modified vertical train-bridge interaction system. To model the bridge, we utilize radial point interpolation method, a

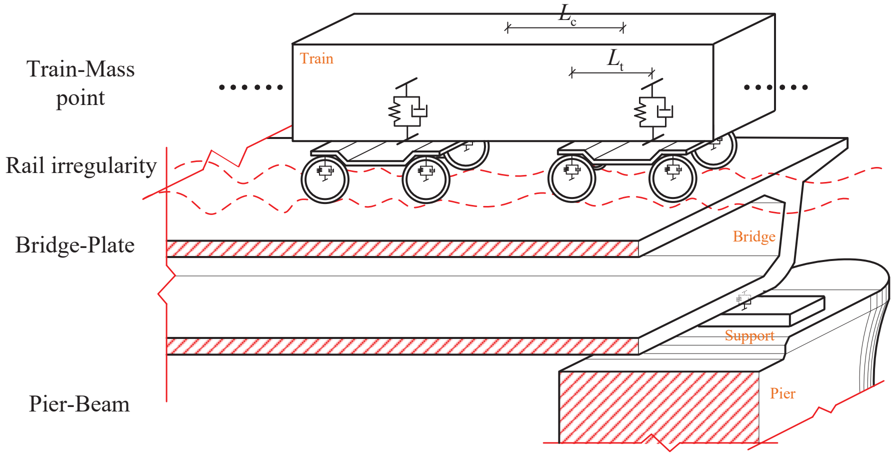

Figure 19: A higher level TBIS with multiple plates.

meshless method, while incorporating first-order shear deformation theory to represent the displacement field of the bridge. We provide the form of each block matrix in the coupled dynamics equations of the presented system. This is the first attempt to combine FSDT and RPIM to build a plate model for bridge simulate within TBIS. Furthermore, we conduct an analysis of the mid-span vertical displacement, vertical acceleration, and carbody acceleration for both the beam model and the proposed plate model. A comparison between the two models is performed, and the results yield the following findings:

(1) The analysis of the mid-span vertical displacements reveals that they exhibit an increasing trend as the width-thickness ratio increases. It is noteworthy that for lower span numbers, the mid-span vertical displacements obtained from the beam model are notably larger than those obtained from the plate model. In contrast, the plate model offers the advantage of providing more detailed information, such as the vertical displacement at any specific point within the bridge surface.

(2) The mid-span vertical acceleration exhibits an upward trend as the width-thickness ratio increases. Notably, the plate model surpasses the beam model in terms of its ability to provide vertical acceleration

information at every point along the entire bridge surface. Additionally, it is observed that the vertical acceleration is greater on the traffic side compared to the opposite side. Moreover, the vertical acceleration amplitude is significantly larger at the section of the bridge surface in contact with the wheels compared to other locations. In contrast, the beam model can only offer the overall vertical acceleration of the bridge, limiting its utility in targeted analysis and design of the bridge.

(3) The carbody acceleration exhibits minimal dependence on the bridge model and width-thickness ratio. Instead, it is primarily influenced by track irregularities.

As we mentioned in Section 1, this study establishes a theoretical foundation and validates the feasibility of implementing TBIS with precision bridge modeling within a unified platform. In engineering practice, a majority of simply supported girder bridges employ box girder structures, however, certain terrains necessitate the construction of large-span continuous girder bridges. The proposed model faces challenges in simulating such large-span bridges. As the span increases, the mechanical model becomes closer to a beam rather a plate. However, traditional beam models are also inadequate for simulating this bridge type effectively. We recommend employing a co-simulation approach, wherein programming software like MATLAB is utilized to simulate the structure above the bridge, while commercial software such as ABAQUS, ANSYS, and SIMPACK are employed for a refined modeling of the bridge.

Acknowledgments

This work was funded by the National Natural Science Foundation of China (Grant No. 11972379), the Key R&D Program of Hunan Province (2020SK2060), and Hunan Science Fund for Distinguished Young Scholars (2021JJ10061).

Declaration of Competing Interest

The authors declare that they have no known competing financial interests or personal relationships that could have appeared to influence the work reported in this paper.

Data Availability Statement

The data that support the findings of this study are available from the corresponding author, upon reasonable request.

References

[1] H. Zhao, B. Wei, L. Jiang, P. Xiang, X. Zhang, H. Ma, S. Xu, L. Wang, H. Wu, X. Xie, A velocity-related running safety assessment index in seismic design for railway bridge, Mech Syst Signal Pr 198 (2023) 110305. doi:10.1016/j.ymssp.2023.110305.

[2] Y. Wang, P. Wang, H. Tang, X. Liu, J. Xu, J. Xiao, J. Wu, Assessment and prediction of high speed railway bridge long-term deformation based on track geometry inspection big data, Mech Syst Signal Pr 158 (2021) 107749. doi:10.1016/j.ymssp.2021.107749.

[3] H. Zhao, B. Wei, P. Guo, J. Tan, P. Xiang, L. Jiang, W. Fu, X. Liu, Random analysis of train-bridge coupled system under non-uniform ground motion, Adv Struct Eng (2023). doi:10.1177/13694332231175230.

[4] C. Koh, J. Ong, D. Chua, J. Feng, Moving element method for train-track dynamics, Int J Numer Meth Eng 56 (11) (2003) 1549–1567. doi:10.1002/nme.624.

[5] L. Xu, Z. Yu, Z. Shan, Numerical simulation for train-track-bridge dynamic interaction considering damage constitutive relation of concrete tracks, Arch Civ Mech Eng 21 (2021) 1–23. doi:10.1007/s43452-021-00266-8.

[6] P. Xiang, H. Ma, H. Zhao, L. Jiang, S. Xu, X. Liu, Safety analysis of train-track-bridge coupled braking system under earthquake, Structures 53 (2023) 1519–1529. doi:10.1016/j.istruc.2023.04.086.

[7] P. Xiang, P. Guo, W. Zhou, X. Liu, L. Jiang, Z. Yu, J. Yu, Three-dimensional stochastic train-bridge coupling dynamics under aftershocks, Int J Civ Eng (2023) 1–17doi:10.1007/s40999-023-00846-0.

[8] L.-L. Ke, J. Yang, S. Kitipornchai, Nonlinear free vibration of functionally graded carbon nanotube-reinforced composite beams, Compos

Struct 92 (3) (2010) 676–683. doi:10.1016/j.compstruct.2009.09.024.

[9] S. Kitipornchai, D. Chen, J. Yang, Free vibration and elastic buckling of functionally graded porous beams reinforced by graphene platelets, Mater Design 116 (2017) 656–665. doi:10.1016/j.matdes.2016.12.061.

[10] D. Chen, J. Yang, S. Kitipornchai, Elastic buckling and static bending of shear deformable functionally graded porous beam, Compos Struct 133 (2015) 54–61. doi:10.1016/j.compstruct.2015.07.052.

[11] J. Yang, H. Wu, S. Kitipornchai, Buckling and postbuckling of functionally graded multilayer graphene platelet-reinforced composite beams, Compos Struct 161 (2017) 111–118. doi:10.1016/j.compstruct.2016.11.048.

[12] Z. Shao, X. Li, P. Xiang, A new computational scheme for structural static stochastic analysis based on karhunen–loève expansion and modified perturbation stochastic finite element method, Comput Mech 71 (5) (2023) 917–933. doi:10.1007/s00466-022-02259-7.

[13] Z.-P. Zeng, F.-S. Liu, P. Lou, Y.-G. Zhao, L.-M. Peng, Formulation of three-dimensional equations of motion for train–slab track–bridge interaction system and its application to random vibration analysis, Appl Math Model 40 (11-12) (2016) 5891–5929. doi:10.1016/j.apm.2016.01.020.

[14] W. Zhou, L. Zu, L. Jiang, J. Yu, Y. Zuo, K. Peng, Influence of damping on seismic-induced track geometric irregularity spectrum in high-speed railway track-bridge system, Soil Dyn Earthq Eng 167 (2023) 107792. doi:10.1016/j.soildyn.2023.107792.

[15] Y. Tang, Z. Zhu, Z. Ba, V. W. Lee, W. Gong, Running safety assessment of trains considering post-earthquake damage state of bridge–track system, Eng Struct 287 (2023) 116187. doi:10.1016/j.engstruct.2023.116187.

[16] X. Liu, P. Xiang, L. Jiang, Z. Lai, T. Zhou, Y. Chen, Stochastic analysis of train–bridge system using the karhunen–loéve expansion and the point

estimate method, Int J Struct Stab Dy 20 (02) (2020) 2050025. doi:10.1142/S021945542050025X.

[17] L. Jiang, X. Liu, P. Xiang, W. Zhou, Train-bridge system dynamics analysis with uncertain parameters based on new point estimate method, Eng Struct 199 (2019) 109454. doi:10.1016/j.engstruct.2019.109454.

[18] X. Lu, C.-W. Kim, K.-C. Chang, Finite element analysis framework for dynamic vehicle-bridge interaction system based on abaqus, Int J Struct Stab Dy 20 (03) (2020) 2050034. doi:10.1142/S0219455420500340.

[19] Z. Zhai, S. Zhu, Y. Yang, J. Luo, C. Cai, Dynamics analysis of train-track-bridge coupled system considering spatial flexibility of high piers and system longitudinal vibrations, Vehicle Syst Dyn 61 (10) (2022) 2613–2637. doi:10.1080/00423114.2022.2124178.

[20] P. Xiang, W. Huang, L. Jiang, D. Lu, X. Liu, Q. Zhang, Investigations on the influence of prestressed concrete creep on train-track-bridge system, Constr Build Mater 293 (2021) 123504. doi:10.1016/j.conbuildmat.2021.123504.

[21] H. Li, T. Wang, G. Wu, Probabilistic safety analysis of coupled train-bridge system using deep learning based surrogate model, Struct Infrastruct E 19 (8) (2023) 1138–1157. doi:10.1080/15732479.2021.2010104.

[22] M. Song, S. Kitipornchai, J. Yang, Free and forced vibrations of functionally graded polymer composite plates reinforced with graphene nanoplatelets, Compos Struct 159 (2017) 579–588. doi:10.1016/j.compstruct.2016.09.070.

[23] J. Yang, H.-S. Shen, Vibration characteristics and transient response of shear-deformable functionally graded plates in thermal environments, J Sound Vib 255 (3) (2002) 579–602. doi:10.1006/jsvi.2001.4161.

[24] T. Belytschko, Y. Y. Lu, L. Gu, Element-free galerkin methods, Int J Numer Meth Eng 37 (2) (1994) 229–256. doi:10.1002/nme.1620370205.

[25] Y. Deng, X. He, L. Sun, S. Yi, Y. Dai, An improved interpolating complex variable element free galerkin method for the pattern transformation of hydrogel, Eng Anal Bound Elem 113 (2020) 99–109. doi:10.1016/j.enganabound.2019.12.004.

[26] A. Ferreira, G. Fasshauer, R. Batra, Natural frequencies of thick plates made of orthotropic, monoclinic, and hexagonal materials by a meshless method, J Sound Vib 319 (3-5) (2009) 984–992. doi:10.1016/j.jsv.2008.06.034.

[27] J.-T. Chen, M. Chang, K. Chen, S. Lin, The boundary collocation method with meshless concept for acoustic eigenanalysis of two-dimensional cavities using radial basis function, J Sound Vib 257 (4) (2002) 667–711. doi:10.1006/jsvi.2002.5038.

[28] P. Xiang, L. Zhang, K. Liew, A mesh-free computational framework for predicting vibration behaviors of microtubules in an elastic medium, Compos Struct 149 (2016) 41–53. doi:10.1016/j.compstruct.2016.03.063.

[29] P. Xiang, L. Zhang, K. Liew, A third-order cauchy-born rule for modeling of microtubules based on the element-free framework, Compos Struct 161 (2017) 215–226. doi:10.1016/j.compstruct.2016.10.110.

[30] P. Xiang, K. M. Liew, Dynamic behaviors of long and curved microtubules based on an atomistic-continuum model, Comput Method Appl M 223 (2012) 123–132. doi:10.1016/j.cma.2012.02.023.

[31] R. A. Gingold, J. J. Monaghan, Smoothed particle hydrodynamics: theory and application to non-spherical stars, Mon Not R Astron Soc 181 (3) (1977) 375–389. doi:10.1093/mnras/181.3.375.

[32] J. J. Monaghan, Smoothed particle hydrodynamics, Annu Rev Astron Astr 30 (1) (1992) 543–574. doi:10.1146/annurev.aa.30.090192.002551.

[33] W. K. Liu, S. Jun, Y. F. Zhang, Reproducing kernel particle methods, Int J Numer Meth Fl 20 (8-9) (1995) 1081–1106. doi:10.1002/fld.1650200824.

[34] P. Xiang, Q. Xia, L. Jiang, L. Peng, J. Yan, X. Liu, Free vibration analysis of fg-cntrc conical shell panels using the kernel particle ritz element-free method, Compos Struct 255 (2021) 112987. doi:10.1016/j.compstruct.2020.112987.

[35] N. Perrone, R. Kao, A general finite difference method for arbitrary meshes, Comput Struct 5 (1) (1975) 45–57. doi:10.1016/0045-7949(75)90018-8.

[36] T. Liszka, J. Orkisz, The finite difference method at arbitrary irregular grids and its application in applied mechanics, Comput Struct 11 (1-2) (1980) 83–95. doi:10.1016/0045-7949(80)90149-2.

[37] G.-R. Liu, Y. Gu, A point interpolation method for two-dimensional solids, Int J Numer Meth Eng 50 (4) (2001) 937–951. doi:10.1002/1097-0207(20010210)50:4<937::AID-NME62>3.0.CO;2-X.

[38] J. Wang, G. Liu, A point interpolation meshless method based on radial basis functions, Int J Numer Meth Eng 54 (11) (2002) 1623–1648. doi:10.1002/nme.489.

[39] Q. Xia, P. Xiang, L. Jiang, J. Yan, L. Peng, Bending and free vibration and analysis of laminated plates on winkler foundations based on meshless layerwise theory, Mech Adv Mater Struc 29 (27) (2021) 6168–6187. doi:10.1080/15376494.2021.1972497.

[40] Z. Liu, G. Wei, Z. Wang, Numerical solution of functionally graded materials based on radial basis reproducing kernel particle method, Eng Anal Bound Elem 111 (2020) 32–43. doi:10.1016/j.enganabound.2019.09.023.

[41] Z. Liu, H. Gao, G. Wei, Z. Wang, The meshfree analysis of elasticity problem utilizing radial basis reproducing kernel particle method, Results Phys 17 (2020) 103037. doi:10.1016/j.rinp.2020.103037.

[42] S. Qin, G. Wei, B. Tang, The meshless analysis of elastic dynamic problem based on radial basis reproducing kernel particle method, Soil Dyn Earthq Eng 139 (2020) 106340. doi:10.1016/j.soildyn.2020.106340.

[43] T. Zhang, G. Wei, J. Ma, H. Gao, Radial basis reproducing kernel particle method for piezoelectric materials, Eng Anal Bound Elem 92 (2018) 171–179. doi:10.1016/j.enganabound.2017.10.020.

[44] J. Belinha, A. Araújo, A. Ferreira, L. Dinis, R. N. Jorge, The analysis of laminated plates using distinct advanced discretization meshless techniques, Comput Struct 143 (2016) 165–179. doi:10.1016/j.compstruct.2016.02.021.

[45] D. Rodrigues, J. Belinha, L. Dinis, R. N. Jorge, The bending behaviour of antisymmetric cross-ply laminates using high-order shear deformation theories and a radial point interpolation method, in: Structures, Vol. 32, 2021, pp. 1589–1603. doi:10.1016/j.istruc.2021.03.048.

[46] O. Askour, S. Mesmoudi, Y. Hilali, M. Rammane, O. Bourihane, An improved fsdt with an efficient mesh-free approach for nonlinear static analysis of fg-goprc beams, in: Structures, Vol. 58, 2023, p. 105575. doi:10.1016/j.istruc.2023.105575.

[47] X. Liu, L. Jiang, Z. Lai, P. Xiang, Y. Chen, Sensitivity and dynamic analysis of train-bridge coupled system with multiple random factors, Eng Struct 221 (2020) 111083. doi:10.1016/j.engstruct.2020.111083.

[48] P. Xiang, M. Wei, M. Sun, Q. Li, L. Jiang, X. Liu, J. Ren, Creep effect on the dynamic response of train-track-continuous bridge system, Int J Struct Stab Dy 21 (10) (2021) 2150139. doi:10.1142/S021945542150139X.

[49] P. Lou, Q. Zeng, Formulation of equations of motion of finite element form for vehicle–track–bridge interaction system with two types of vehicle model, Int J Numer Meth Eng 62 (3) (2005) 435–474. doi:10.1002/nme.1207.

[50] L. Xiang, J. Lizhong, X. Ping, et al., Analysis of train-bridge vertical random vibration based on a new point estimate method, Journal of Vibration and Shock 39 (6) (2020) 15–21. doi:10.13465/j.cnki.jvs.2020.06.003.

[51] J. Yang, H.-S. Shen, Dynamic response of initially stressed functionally graded rectangular thin plates, Compos Struct 54 (4) (2001) 497–508. doi:10.1016/S0263-8223(01)00122-2.

[52] C. Lü, C. W. Lim, W. Chen, Exact solutions for free vibrations of functionally graded thick plates on elastic foundations, Mech Adv Mater Struc 16 (8) (2009) 576–584. doi:10.1080/15376490903138888.

[53] C. W. Lim, C. Lü, Y. Xiang, W. Yao, On new symplectic elasticity approach for exact free vibration solutions of rectangular kirchhoff plates, Int J Eng Sci 47 (1) (2009) 131–140. doi:j.ijengsci.2008.08.003.

[54] C. Lim, Z. Li, Y. Xiang, G. Wei, C. M. Wang, On the missing modes when using the exact frequency relationship between kirchhoff and mindlin plates, Adv Vib Eng 4 (3) (2005) 221–248.

[55] M. Rafiee, X. He, K. Liew, Non-linear dynamic stability of piezoelectric functionally graded carbon nanotube-reinforced composite plates with initial geometric imperfection, Int J Nonlin Mech 59 (2014) 37–51. doi:10.1016/j.ijnonlinmec.2013.10.011.

[56] M. Rafiee, X. He, S. Mareishi, K. Liew, Modeling and stress analysis of smart cnts/fiber/polymer multiscale composite plates, Int J Appl Mech 6 (03) (2014) 1450025. doi:10.1142/S1758825114500252.

[57] K. Liew, X. He, T. Ng, S. Sivashanker, Active control of fgm plates subjected to a temperature gradient: modelling via finite element method based on fsdt, Int J Numer Meth Eng 52 (11) (2001) 1253–1271. doi:10.1002/nme.252.

[58] P. Zhu, Z. Lei, K. M. Liew, Static and free vibration analyses of carbon nanotube-reinforced composite plates using finite element method with first order shear deformation plate theory, Compos Struct 94 (4) (2012) 1450–1460. doi:10.1016/j.compstruct.2011.11.010.

[59] X. Li, Y. Zhu, Z. Jin, Nonstationary random vibration performance of train-bridge coupling system with vertical track irregularity, Shock Vib 2016 (2016) 1450895. doi:10.1155/2016/1450895.

[60] H. Xia, N. Zhang, W. Guo, H. Xia, N. Zhang, W. Guo, Dynamic analysis of train-bridge coupling system, Dynamic Interaction of Train-Bridge

Systems in High-Speed Railways: Theory and Applications (2018) 227–289doi:10.1007/978-3-662-54871-4_5.

[61] Z.-w. Yu, J.-f. Mao, F.-q. Guo, W. Guo, Non-stationary random vibration analysis of a 3d train–bridge system using the probability density evolution method, J Sound Vib 366 (2016) 173–189. doi:10.1016/j.jsv.2015.12.002.

[62] L. Xu, W. Zhai, A three-dimensional model for train-track-bridge dynamic interactions with hypothesis of wheel-rail rigid contact, Mech Syst Signal Pr 132 (2019) 471–489. doi:10.1016/j.ymssp.2019.04.025.

[63] H.-H. Phan-Dao, C. H. Thai, J. Lee, H. Nguyen-Xuan, Analysis of laminated composite and sandwich plate structures using generalized layerwise hsdt and improved meshfree radial point interpolation method, Aerosp Sci Technol 58 (2016) 641–660. doi:10.1016/j.ast.2016.09.017.

[64] H. Zhao, B. Wei, L. Jiang, P. Xiang, Seismic running safety assessment for stochastic vibration of train–bridge coupled system, Arch Civ Mech Eng 22 (4) (2022) 180. doi:10.1007/s43452-022-00451-3.

[65] P. Zhang, H. Zhao, Z. Shao, L. Jiang, H. Hu, Y. Zeng, P. Xiang, A rapid analysis framework for seismic response prediction and running safety assessment of train-bridge coupled systems, Soil Dyn Earthq Eng 177 (2024) 108386. doi:10.1016/j.soildyn.2023.108386.

[66] H. Zhao, B. Wei, P. Zhang, P. Guo, Z. Shao, S. Xu, L. Jiang, H. Hu, Y. Zeng, P. Xiang, Safety analysis of high-speed trains on bridges under earthquakes using a lstm-rnn-based surrogate model, Comput Struct 294 (2024) 107274. doi:10.1016/j.compstruc.2024.107274.

[67] P. Xiang, P. Zhang, H. Zhao, Z. Shao, L. Jiang, Seismic response prediction of a train-bridge coupled system based on a lstm neural network, Mech Based Des Struc (2023) 1–23doi:10.1080/15397734.2023.2260469.

[68] H. Xiang, J. Yang, Free and forced vibration of a laminated fgm timoshenko beam of variable thickness under heat conduction, Compos Part B-Eng 39 (2) (2008) 292–303. doi:10.1016/j.compositesb.2007.01.005.